



Mohamad Ali Nasri, Ili Farhana (2019) *Optical sensors based on asymmetric plasmonic nanostructures for environmental monitoring*. PhD thesis.

<https://theses.gla.ac.uk/75134/>

Copyright and moral rights for this work are retained by the author

A copy can be downloaded for personal non-commercial research or study, without prior permission or charge

This work cannot be reproduced or quoted extensively from without first obtaining permission from the author

The content must not be changed in any way or sold commercially in any format or medium without the formal permission of the author

When referring to this work, full bibliographic details including the author, title, awarding institution and date of the thesis must be given

Enlighten: Theses

<https://theses.gla.ac.uk/>
research-enlighten@glasgow.ac.uk

Optical Sensors Based on Asymmetric Plasmonic Nanostructures for Environmental Monitoring

Ili Farhana Mohamad Ali Nasri

Submitted in fulfillment of the requirements for the
Degree of Doctor of Philosophy

School of Engineering
College of Science and Engineering
University of Glasgow



October 2019

“ This is by the Grace of my Lord! ”

— (An-Naml 27:40)

Abstract

Optical sensors based on plasmonic nanostructures can be used for high-throughput bio-sensing applications in environmental monitoring, healthcare, food safety etc. Due to their high-sensitivity and flexibility, array metasurfaces have been widely employed as label-free optical sensors for organic compounds and could eventually be used for rapid environmental analysis. Estrogenic hormones have been noted as harmful organic compounds that are often found in water and threaten the quality and security of water supplies.

In this thesis, the fabrication and characterization of plasmonic metamaterial nanostructures array based on asymmetric split-H (ASH) resonators. The ASHs have been optimized to produce plasmonic resonances that match molecular vibrations of the biological material in order to increase the sensitivity and specificity of the biosensor. The geometry of ASH nanostructures was formed by a crossbar (with gap) placed between asymmetric (unequal arm-length) vertical dipoles. ASH and double ASH (D-ASH) were designed on silica substrates and the geometry of the ASHs were tuned to produce double plasmonic resonances. The resonances were measured at normal incidence using a microscope coupled Fourier Transform Infrared (FTIR) spectrometer and observed at mid-infrared wavelengths in the range between 2 and 8 μm , both experimentally and in simulation. To illustrate the sensitivity of the D-ASH, a thin layer of PMMA used as analyte was simulated on top of the devices. The sensitivity for the D-ASH was 1297 nm/RIU. Then, the ASHs were fabricated on the zinc selenide (ZnSe) substrates to ensure low-loss transmission operation up to 21 μm .

Estrogenic hormones; Estrone (E1), 17β -Estradiol (E2), Estriol (E3) and synthetic estrogen; 17α -Ethinyl Estradiol (EE2) were chosen as analytes for coupling with plasmonic resonances. Two geometry sizes of ASH labelled as ASH₁ and ASH₂ produced two distinct plasmonic resonances each that were matched with the five molecular bond resonances (for O-H, C-H, C=O, C=C and C \equiv C-H bonds) observed for the estrogenic hormones. Consequently, it was also possible to differentiate E2 from E1, E3 and EE2 in a mixture of two estrogens. Sensitivities of 363 nm/RIU

and 636 nm/RIU were achieved from the deposition of E2 on two ASHs. The amplitudes of the molecular vibrational resonances were also around 500 times greater when matched with the plasmonic resonances of the ASHs, as compared with deposition on bulk ZnSe substrates.

Finally, the surface functionalization of ASH with specific thiol-terminated aptamers as a bio-recognition element that binds to E2 was described. The 6-Mercapto-1-hexanol (MCH) was used as a blocking agent to prevent non-specific binding on the gold surface. Aptamers functionalized on ASH₁ nanostructures were demonstrated to be effective refractometric sensors for E2 over 5 orders of magnitudes. The experimental results are well supported by simulation results obtained using finite difference time domain (FDTD) software.

Table of Contents

Abstract	ii
Table of Contents	iv
List of Tables	viii
List of Figures	xv
Acknowledgements	xvi
Declaration	xvii
Publication and Conferences	xviii
List of Nomenclature	xx
1 Introduction	1
1.1 Project Motivation	1
1.2 Aim and Objectives	3
1.3 Chapter summary and thesis outline	3
2 Research background and theory	5
2.1 Introduction	5
2.2 Environmental Biosensors	5
2.2.1 The need for environmental biosensors	5
2.2.2 Definition of biosensor	6
2.2.3 State-of-the-art for estrogen biosensors	7
2.3 Plasmonic-based sensing	11
2.3.1 Electromagnetic theory and dielectric properties	11
2.3.2 Refractive index and Negative Refractive Index	12
2.3.3 Plasmonic and surface plasmon resonance	13
2.3.4 Localized surface plasmon resonance	16
2.3.5 Localized surface plasmon resonance sensing	16
2.3.6 Characterization of the LSPR sensing	18

2.3.7	Metal plasmonic nanostructures	20
2.3.8	Examples of LSPR sensing	22
2.4	Bio-recognition	23
2.4.1	Aptamer production	24
2.4.2	Label-free and labelled biosensor	25
2.4.3	Surface modification	26
2.4.4	Estrogen-binding aptamers	27
2.5	Conclusion	27
	References	28
3	Methods	36
3.1	Introduction	36
3.2	Simulation Methods	36
3.2.1	Finite difference time domain	36
3.2.2	Simulation using Lumerical FDTD solutions	37
3.3	Fabrication Methods	39
3.3.1	Electron beam lithography	39
3.3.2	Metallisation	41
3.3.3	Lift-off	41
3.4	Measurement Methods	42
3.4.1	Fourier transform infrared spectroscopy	42
3.5	Characterization of the plasmonic nanostructures	44
3.5.1	Scanning electron microscopy	44
3.5.2	Atomic force microscopy	44
3.5.3	Optical microscopy	45
3.6	Conclusion	45
	References	46
4	Selection of asymmetric nanostructures and substrates for environmental sensors	47
4.1	Abstract	47
4.2	Introduction	47
4.3	Asymmetric plasmonic nanostructures	50
4.3.1	Quality factor in Mid Infrared	52
4.4	Modelling and simulation on the silica substrate	53
4.4.1	Modelling the asymmetrical structure	53
4.4.2	Simulations using FDTD Lumerical software	54
4.5	Fabrication and measurement	58
4.5.1	Fabrication on fused silica	58
4.5.2	Fabrication on ZnSe substrate	59

4.6	Results and discussions	60
4.6.1	Effect the period arrangement of ASH	60
4.6.2	Effect of the period arrangement of dual polarization ASH	64
4.6.3	Varying the gap of dual polarization ASH	65
4.6.4	Effect of different substrates	67
4.6.5	Variation of the ASH arm-length on ZnSe substrate	69
4.7	Conclusions	72
	References	73
5	Detection of estrogenic hormones using plasmonic nanostructures	77
5.1	Abstract	77
5.2	Estrogenic hormones	77
5.3	Materials and Methods	80
5.3.1	Gold nanostructures fabrication	80
5.3.2	FTIR measurement	80
5.3.3	FDTD simulations	81
5.3.4	Estrogenic hormone preparation	81
5.4	Results and discussions	81
5.4.1	Molecular bonds of the estrogenic hormones	81
5.4.2	Matching the molecular bonds of estrogens with ASH resonance	85
5.4.3	Detection of the mixture of two estrogenic hormones	92
5.5	Conclusions	98
	References	99
6	Aptamers as bio-recognition element for plasmonic estrogenic hormone biosensor	102
6.1	Abstract	102
6.2	Aptamer-based biosensor	102
6.3	Materials and Methods	105
6.3.1	Chemicals	105
6.3.2	Fabrication, measurements and characterization	106
6.3.3	Surface functionalization of the gold nanostructures surface	106
6.4	Results and discussions	108
6.4.1	Detection of 6-mercapto-1-hexanol	108
6.4.2	Immobilization of aptamers	110
6.4.3	Detection of 17 β -Estradiol (E2)	114
6.4.4	Surface modification characterized by AFM	119
6.5	Conclusion	120
	References	121

7	Conclusions and future work	124
7.1	Aim and Objectives	124
7.2	Summary findings and conclusion	124
7.3	Recommendation for future work	126
7.3.1	Improving the nanofabrication	126
7.3.2	Improving surface functionalization	127
7.3.3	Towards an environmental sensor	127
	References	128
	Appendix A Graphs	129

List of Tables

2.1	Maximum and minimum concentration of natural estrogens in water samples (E1, E2 and E3 (estriol)) - NM: not measured; ND: Not Detected; ¹ Concentrated Animal Feeding Operation, ² Sewage Treatment Works [Adapted from Sarah Jane Haig Thesis, (2014) [7]].	8
2.2	Types of biosensor available on the environmental sensing. All the range unit in the table have been converted to pg/ml.	10
4.1	Comparison of the Q-factors in the infrared wavelengths.	53
5.1	Illustration of (a) Estrone (b) 17 β -Estradiol (c) Estriol and (d) 17 α -Ethinyl Estradiol chemical structures showing the common regions and in functional groups.	79
5.2	The summary of molecular vibrational peaks and absorption features extracted from the estrogenic hormones deposited on plain ZnSe substrate in the mid-IR wavelength between 2.00 μm to 8.00 μm	83
5.3	Summary of the initial position of ASH ₁ and ASH ₂ and resonance shifted after deposition of E2 on the nanostructures. The sensitivity was calculated by spectral shift to the refractive index change. The value of refractive index change is $\Delta n \approx 1.55$	90
5.4	Compositions of E2 - E1 mixtures with different ratios, diluted in absolute ethanol and having the same total concentration of 2mg/ml.	92
5.5	Table of the mixtures between E2 and E1 with different ratios diluted in the absolute ethanol giving the same total concentration of 2mg/ml.	95

List of Figures

1.1	Illustration of main sources of estrogen in the water release into the environment [1]–[3].	2
2.1	Biosensor block diagram. Biosensor consists of biorecognition elements, transducer and the signal processing.	7
2.2	(a) Light refracted by a conventional material (b) light refracted by a material with a negative refractive index.	13
2.3	(a) Illustration of the surface plasmon propagating along the x-axis at the metal-dielectric interface. The electric field line is the z-direction. (b) Dispersion curve for surface plasmon polaritons; the grey straight line is the photon line in air, the brown dashed line is the SPP and the orange dotted line is the bulk plasmon. Where ω_p is the plasma frequency of free electrons in the metal, ω_{SP} is the surface plasmon frequency.	14
2.4	Schematic diagram of localized surface plasmon resonance on the nanoparticle surface showing the electron displacement [36].	16
2.5	(a) LSPR (b) SPR configuration of the detection principle of plasmonic sensing.	17
2.6	Illustration of plasmonic biosensor based on (a) refractive index sensing and (b) surface molecular sensing integrated with SEIRA.	18
2.7	The plan view of a split ring structure in a square array, lattice spacing, a by Pendry <i>et al.</i> [42].	20
2.8	Schematic representation of (a) electric and (b) magnetic field distribution inside a metallic split-ring resonator. (Figure where reprint from the published paper [46]).	21
2.9	(a) The size comparison between the IgG antibody and the thrombin aptamer. (b) The secondary structure of DNA aptamer by Kim <i>et al.</i> used in this study. (Figure adapted from the published paper [31], [69]).	24
2.10	Schematic figure of the SELEX process (Figure adapted from the published paper [65]).	25

2.11	Immobilization of gold surface via the thiol group.	26
3.1	Displacement of the electric (E) and magnetic (H) field vector components about a cubic unit cell of the Yee space lattice.	37
3.2	The FDTD simulation schematic for setup for modelling the ASH nanostructures (10 nm Titanium (Ti) and 100 nm Gold (Au)). The images showed the model in XY and XZ plane view. (1)Tx: Transmission, (2)E-Fields: Electric fields, (3) Rx: Reflection.	38
3.3	(a) The top images show the resist was spun to form a uniform layer. (b) Positive and negative resist behaviour after the development process.	40
3.4	Lift-off process	41
3.5	Schematic diagram of an optical beam path for the FTIR experimental setup for the reflection and transmission measurement.	43
4.1	The various nanostructures shaped (a) XI structures, (b) seven split nanoring (SNR) (c) asymmetric double bar (ADB), (d) Split ring resonator (SRR), (e) asymmetric nanostructure (f) χ -shaped nanostructures.	50
4.2	Illustration of Asymmetric Split Ring Resonators (ASRR) with different size of arc-length and (b) Asymmetric split H-shape (ASH). . .	51
4.3	The simulation results of the reflectance resonance peak between ASRR and ASH with $2.40 \mu\text{m}$ periodic boundary size. The geometry sizes of ASH are $L_1 = 1.3 \mu\text{m}$ and $L_2 = 1.1 \mu\text{m}$ and the diameter of ASRR is $1.2 \mu\text{m}$. Both of the structures produce the resonances between wavelengths of $3.5 \mu\text{m}$ to $5.5 \mu\text{m}$	52
4.4	Schematic diagrams of Asymmetric H-Shaped (ASH) resonators for FDTD simulation in one-unit cells including the geometrical parameters, arm lengths (L_1 and L_2), horizontal dipole (H) width (w), gap (g) and thickness (t). The incident light polarization, E_Y and E_X are shown in the figure.	53
4.5	Varying the ASH and SSH geometries structure. Transmittance and reflectance spectra at $2.8 \mu\text{m}$ periodicity in both polarizations; (a) polarization parallel with vertical dipoles (b) polarization perpendicular with horizontal dipoles.	55
4.6	Schematic and simulation results of the geometries for ASH and side to side. Illustration of nanostructures with (a) the arm-length, L_1 of ASH produced a resonant with green dashed line, (b) the arm-length, L_2 of ASH with resultants in orange dotted line and (c) ASH with a black line.	56

4.7	An energy level diagram describing the plasmon hybridization of ASH. The coupling effect between both arm-length, L_1 and L_2 produce two new modes, symmetric and antisymmetric.	57
4.8	Illustration of the fabrication process steps on fused silica or ZnSe substrates as explained in the Section 4.5.	59
4.9	Scanning electron micrograph image of ASH nanostructures array with different periodicity (a) 2.4 μm , (b) 2.8 μm (c) 3.0 μm and (d) 3.2 μm	61
4.10	Measurement and simulation reflection spectra in different periodicity and polarization. The experimental resonance was plotted in blue line and the simulations resonance peak were plotted in black dashed line. In the E_X polarization, the simulation was performed with 0 nm gap and 50 nm gap.	62
4.11	Comparison between the measurement and simulation for arm-lengths,(a) $L_2 = 1.2 \mu\text{m}$ and (b) $L_1 = 1.6 \mu\text{m}$ for Q-factors versus periodic arrangement. (c) Wavelength versus periodic arrangement for arm-lengths, L_1	63
4.12	The schematic images (d) of the ASH structures on the plots for the reflectance spectral peaks obtained from numerical simulation with the electric field polarized: (a) across the gap along the x-axis and (b) along the y-axis. (c) Comparison graph of the Q-factor for the E_X and E_Y polarizations of the incident light electromagnetic waves.	65
4.13	Effect on varying the gap sizes from 0 nm to 200 nm on the reflection spectra for both polarization; (a) E_Y polarization and (b) E_X polarization. (c)gap versus wavelength.	66
4.14	E-fields plot at the plasmonic resonance of 7.5 μm when the D-ASH with 0 nm gap and at resonance 4.28 μm with 200 nm gap.	67
4.15	Simulation results of ASH on different substrate (a) fused silica and (b) ZnSe substrate. The incident light has been polarized parallel with the asymmetric arm length; $L_1 = 1.6 \mu\text{m}$ and $L_2 = 1.2 \mu\text{m}$	68
4.16	Simulation and experimental results of varying the arm length, L_2 with 500 nm, 550 nm, 600 nm, and 650 nm. The arm length, L_1 remains constant. Other parameters remain unchanged. All figures were labelled with ASH (L_1, L_2) μm	70
4.17	The arm-length of L_1 (nm) function of the wavelength (μm). Lines are linear fits with the arm-length (L_1, L_2 and the gap G) is increase the resonance peak position also increased.	70

- 4.18 (a) Simulated transmittance spectra of a 50 nm thickness with different refractive indexed on ASH, modelled on the ZnSe substrates. (b) Zoom-in on the simulated transmittance spectra of (a). (c) Resonance shifts function ($\Delta\lambda$ nm) of the refractive index (n) of the surrounding for the ASH. Lines are linear fits 71
- 5.1 The magnified transmittance measurement results of the 10 μg estrogenic hormones deposited on the plain ZnSe substrates between 2.00 μm to 8.00 μm . The signals were recorded with $380 \times 380 \mu\text{m}^2$ sized area. For the purpose of better visibility, shows in the stacked plot. The circular dashed line indicates the molecular vibrational bonds of O-H, C-H, C=O, C=C and C \equiv C-H appeared in estrogenic hormone spectra. 83
- 5.2 The microscope images of the 10 μg estrogenic hormones on the plain ZnSe substrates with 5x and 100x magnification. 84
- 5.3 Experimental results of tuning the arm-length of ASH₁ to produce resonance at 2 to 4 μm and ASH₂ at 5 to 8 μm . The black dashed lines are the highlighted area of the position of the molecular vibrations bond resonance. 86
- 5.4 Simulated and measurement spectra of (a) ASH₁ and (b) ASH₂. The black dashed line is the simulated results obtained by Lumerical FDTD and the blue line is the measurement results using for corresponding ASH (L_1, L_2) - ASH₁ (800 nm, 600 nm) and ASH₂ (1.5 μm , 1.2 μm) 87
- 5.5 Scanning electron micrograph image of an array and one-unit cell of asymmetric split H (ASH) resonators with different sizes; (a) ASH₁ and (b) ASH₂. 87
- 5.6 AFM images show 1 mg/ml concentration of E2 in EtOH (a) before and (b) after deposition on the ASH arrays (c) on the ZnSe substrate alone over an area of $10 \times 10 \mu\text{m}^2$. The E2 was crystallized on top of the sample. 88
- 5.7 Top panel: The red line in both plots shows the deposition of E2 on the bare ZnSe substrate. Bottom panel: The figures showed the shift in the position of the transmittance resonance from (a) ASH₁ (b) ASH₂ sample before (black line) and after (blue line) the deposition of 1 mg/ml concentration of E2. The dashed blue line indicates the molecular bond vibration matched with the resonance shifted. 89

- 5.8 The transmittance spectra of three selected sizes of ASH as indicated covered with a thin layer of E2. The plot on the right is the magnified to the molecular vibration of the C-H bond. The black dashed line is referring to the C-H bond resonance at $3.41\ \mu\text{m}$ and $3.48\ \mu\text{m}$ 90
- 5.9 Shows the vibrational resonance after the baseline correction spectra of 1mg/ml solution of E1 (blue line), E2 (red line), E3 (orange line) and EE2 (green line) on ASH_1 and ASH_2 . The spectra are plots in stacked for better visibility. The black arrow indicated the peak-to-peak amplitude. 91
- 5.10 The upper panel: The vibrational transmittance spectrum of E2: E1 on the 1mm thickness ZnSe substrate alone measured with $380 \times 380\ \mu\text{m}^2$. Middle panel: Plots transmittance resonances of shift in position (a) ASH_1 and (b) ASH_2 before (black colour) and after coated (red line) with the mixtures of E2 and E1 (50:50). Bottom panel: show the vibrational resonances after the baseline correction in the fingerprints of O-H, C-H, C=O and C=C bonds. The position of the respective vibrational resonances are shown with the blue dashed lines. 93
- 5.11 Baseline correction spectra of the mixtures E2 with E1 (green line), E3 (olive line) and EE2 (purple line). The peak amplitude of the enhanced signal was calculated based on a peak to peak value. The peak position agrees well with the deposition on the ZnSe substrate alone. Stacked plots were used for the purpose of better visibility. . . 94
- 5.12 Determination of percentage peak intensity of each of the molecular bond resonances C-H, C=O and C=C in three different mixtures of E2 with E1, E3, and EE2. 94
- 5.13 Determination of percentage peak intensity of each molecular bond resonances C-H, C=O and C=C in three different ratios of E2 to E1. 96
- 5.14 The peak intensity after baseline correction of the C=O group as a function of E1 concentration. The peaks are linearly correlated to the concentration of E1. 96
- 5.15 Fingerprint signal intensities for mixtures of two estrogens E2: E1 on ASH arrays showing transmittance resonances extracted after baseline correction. The C=O molecular peak intensity increases directly with the amount of E1 in the mixtures. The double-bond resonance peak occurs at the same peak intensity, in order to indicate the total concentration of the mixtures of estrogens. 97

- 6.1 Schematic images of the surface functionalization of APT on the gold nanostructures samples following the protocol [12]. (a) the sample was clean with UV ozone, (b) surface functionalization to attach the aptamer on gold surface (c) surface blocking to cover the empty space on gold surface (d) E2 to be captured by the aptamer. 107
- 6.2 The FTIR transmittance spectra of (a) ASH₁ and (b) ASH₂ after deposition of MCH with a concentration of 14.6 μM . The bottom panel is the zoom in view of the transmittance spectra in (a) to indicate the C-H stretching and C-H bending bond of the MCH. 109
- 6.3 The FTIR transmittance spectra of ASH₁ after deposition of 100 μM of E2 on MCH (b) The zoom-in view of the transmittance spectra in (a) to indicate no interaction or no resonance shift. 109
- 6.4 Measured wavelength shifts of the ASH₁ (black line) and ASH₂ (grey line) transmittance resonance as a function of aptamer (APT) concentration. The error bars are representing the standard deviation of three measurements were taken in the same sample with different arrays. The negative values represent the blue shifting of the resonance. 111
- 6.5 (a) Simulated transmittance spectra of ASH with a different value of the refractive index (n). The blue dotted line indicated the initial resonance of the bare ASH. (b) the zoom-in view of (a) showing the resonance was blue-shifted. 113
- 6.6 (a) Simulated transmittance spectra of the different thickness of aptamer varied from 2 nm to 10 nm (b) zoom-in view of (a) showing the transmittance spectra are blue-shifted and red-shifted depending on the thickness of aptamer. 113
- 6.7 (a) Simulation transmittance peaks as a function of the refractive index value (b) Simulations wavelength shifts of the ASH transmittance spectra as a function of the thickness of aptamer. The refractive index of the aptamer was set, $n = 1.52$ 114
- 6.8 The resonance shifts as a function of the concentration of the E2 on ASH₁. The resonance shifts were calculated based on the peak position of the bare ASH as the initial value. Two different concentration of aptamer was used in this experiment. 115
- 6.9 Resonance shifts as a function of the same concentration of 3 μM APT and various concentrations of E2 on ASH₁ (red line) and ASH₂ (grey line). 116
- 6.10 RI sensitivity of the ASH with (red line) and without (blue line) the deposition of 6-mercapto-1-hexanol (MCH). 116

6.11	(a) Measured transmittance spectra (zoomed in) of ASH arrays after functionalizing the sensor surface with aptamer, the blocking agent (MCH) and subsequent binding with 17 β - Estradiol (E2) with different concentrations. The molecular vibration of C-H bonds is highlighted in blue, respectively. (b) Shows the vibration resonance of each concentration after the baseline correction of the transmittance spectra in (a). The spectra are plots in stacked for better visibility. The respective C-H molecular bond resonance of E2 is shown by the blue dashed line; the C-H bonds of MCH is shown by black dashed line.	117
6.12	Peak intensity observed at 3.41 μm and 3.49 μm as a function of the concentration of E2. The blue line indicated the peak intensity of E2, and the red line indicated the reducing of peak of MCH at 3.42 μm and 3.50 μm .	118
6.13	AFM image of (a) the bare ASH (b) after the surface functionalization by attaching the APT (c) the uncovered surface was covered by MCH and (d) after the E2 binding.	119
6.14	Height profile of the AFM images in Figure 6.13 (a) ASH alone with (b) APT on the ASH. The blue the red line indicates the height profile at a different area and measured from the baseline to the top peak.	120
A.1	AFM images of (a) Estrone (E1) (b) 17 β -Estradiol (E2) (c) Estriol (E3) (d) 17 α -Ethinyl Estradiol with 1mg/ml solution concentration deposited on the ZnSe substrate. The images were obtained using ScanAsyst mode with the scale bar 10 μm	129
A.2	Matching the molecular bonds of (a) Estrone (b) 17 β -Estradiol (c) Estriol and (d) 17 α -Ethinyl with the plasmonic resonance.	130
A.3	Plots transmittance resonances from the ASH with the mixture of E2 with E1, E3, and EE2 vibrational resonances for the C-H, C=O and C=C bonds with the inset showing the zoomed plots	131
A.4	Plots transmittance resonances from the ASH with the mixture of E2 with E1 with different ratio.	132
A.5	Microscope images of the mixture of E2 with E1 with a different ratio on the ASH arrays	133
A.6	FTIR transmittance spectra of three arrays in a different area from samples mixtures of E2: E1 (4:4)	134

Acknowledgements

First and foremost, I would like to express my sincere gratitude to my supervisors, Dr Caroline Gauchotte-Lindsay and Prof Marc Sorel for providing me invaluable guidances and continuous support throughout my study. Their patience, motivation, useful feedback and helped me in all time of research and writing of the thesis. This study would not have been possible without them.

I would like to acknowledge my former supervisor, Dr Nigel Johnson who initially gave me the opportunity to continue my study and stay with me until the end of the journey. Additionally, Prof Richard De La Rue is a great source of inspiration who always share his knowledge and experience.

Additionally, I would like to express my sincere gratitude to the following people who contributed towards this success of this study:

1. Prof Sorel's research group especially Graham, JWNC and optoelectronics technical staffs who always assist me in the fabrications and measurements. Also to Dr Johnson's research group, Ifeoma, Jharna, Sean for helping me in my early stage of this study.
2. Technical staffs; Julie Russell, Anne McGarrity, HiRACE groups members and people in the Environmental laboratory who helped me a lot in the biology and chemistry samples preparation.
3. Assoc Prof Nathalie Lidgi-Guigui who teaches me on the surface functionalization with Thierry and Andrea at Université Paris 13. Thanks to SRPe and Mobility funding for helping to make the research visit to France possible.

Many thanks to my housemate, Faezah for the encouragement and Ana, Nita, Nadhirah who helped me before the thesis submission. To all my officemates, thanks for the amazing memories in the past four years. Also, my life could not be completed without having my Glasgow and Malaysian friends for making me feel like home.

Gratitude to my parents, and siblings for their endless support and prayers throughout my study and life in general. Finally, last but by no means least, to Majlis Amanah Rakyat (MARA) for sponsoring my study and UniKL MIAT to approve my study leave. Thanks for all your encouragement!

Declaration

I declare that, except where explicit reference is made to the contribution of others, that this thesis is the result of my own work and has not been submitted for any other degree at the University of Glasgow or any other institution.

Ili Farhana Mohamad Ali Nasri

Publication and Conferences

Articles

1. I. G. Mbomson, **I. F. Mohamad Ali Nasri**, R. M. De La Rue, and N. P. Johnson, “Dual polarization operation of nanostructure arrays in the mid-infrared,” *Appl. Phys. Lett.*, vol. 112, no. 7, p. 73105, Feb. 2018.

Conferences

1. **I. F. Mohamad Ali Nasri**, G. J. Sharp, R. M. De La Rue, N. P. Johnson, M. Sorel, and C. Gauchotte-Lindsay, “Detection of organic molecules using asymmetric plasmonic nanostructures,” in META 2019, the 10th International Conference on Metamaterials, Photonic Crystals and Plasmonics, Instituto Superior Técnico, Lisbon, Portugal, 23 – 26 July 2019.
2. **I. F. Mohamad Ali Nasri**, I.G. Mbomson, G. J. Sharp, R. M. De La Rue, N. P. Johnson, M. Sorel, and C. Gauchotte-Lindsay, “Biomedical optical sensing using nano-/micro-structured metamaterials,” in 21th International Conference of Transparent Optical Network, Angers, France, 9 – 13 July 2019.
3. **I. F. Mohamad Ali Nasri**, G. J. Sharp, R. M. De La Rue, N. P. Johnson, M. Sorel, and C. Gauchotte-Lindsay, “Array metasurfaces based on asymmetric split-H resonator for environment monitoring system” in Sensors 2019: Sensors and Networks for Environmental Monitoring at the Royal Society of Chemistry, Burlington House, London, 26th June 2019.
4. **I. F. Mohamad Ali Nasri**, G. J. Sharp, R. M. De La Rue, N. P. Johnson, M. Sorel, and C. Gauchotte-Lindsay, “Optical sensing of estrogenic hormones using nanostructured metamaterials,” in Symposium on Fibre Optic and Photonic Sensors for Industrial and Healthcare Applications – New Challenges and Opportunities, Grasmere, UK, 15 -18 October 2018.
5. **I. F. Mohamad Ali Nasri**, G. J. Sharp, R. M. De La Rue, N. P. Johnson, M. Sorel, and C. Gauchotte-Lindsay, “Asymmetric split H resonators for

estrogenic hormone detection,” in SPIE Phototonics Europe: Metamaterials, Strasbourg, France, 22- 26 April 2018.

6. **Ili F. Mohamad Ali Nasri**, Ifeoma G. Mbomson, Richard M. De La Rue, Nigel P. Johnson, ”Varying the periodicity to achieve high quality factor on asymmetrical H-Shaped resonators,” Proc. SPIE 9883, Metamaterials X, 98831N, 18 April 2016.

Award

1. **Best Contributed Paper** in Symposium on Fibre Optic and Photonic Sensors for Industrial and Healthcare Applications – New Challenges and Opportunities, Grasmere, UK, 15 -18 October 2018.
2. Received a travel grant from Scottish Research Partnership in Engineering (SRPe) under PERCE Award 2017/18 for a two months visit to Université Paris 13.

List of Nomenclature

Abbreviations

AFM	Atomic Force Microscopy
Ag	silver
Al	aluminium
APT	Aptamers
ASH	Asymmetric split-H resonators
AsLSS	asymmetric least squares smoothing
ASRR	Asymmetric split ring resonators
Au	gold
CAD	computer-aided design
CEC	contaminants of emerging concerns
D-ASH	Double Asymmetric split-H resonators
DNA	Deoxyribonucleic Acid
E1	Estrone
E2	17 β -Estradiol
E3	Estriol
EDC	endocrine-disrupting chemicals
EE2	17 α -Ethinyl Estradiol
EF	Enhancement factor
FDTD	finite-difference time-domain

FHWM	Full half width maximum
FOM	figure of merit
FTIR	Fourier Transform Infrared Spectroscopy
LSPR	Localized surface plasmon resonance
MCH	6-mercapto-1-hexanol
PMMA	polymethylmethacrylate
Q-factor	Quality factors
RIU	Refractive index unit
RO	reverse osmosis
SAM	self-assembled monolayer
SEIRA	Surface enhanced infrared absorption
SELEX	Systematic Evolution of Ligands by Exponential enrichment
SEM	Scanning Electron Microscopy
SERS	Surface enhancement Raman Spectroscopy
SiO ₂	fused silica
SP	surface plasmon
SPR	surface plasmon resonance
SRR	Split ring resonantors
SSH	Symmetric split-H resonators
WWTP	Wastewater treatment plants
ZnSe	Zinc Selenide

Other Symbols

ΔI	changes in intensity
ΔR	relative change in the reflectance
Δn	changes in refractive index

$\Delta\lambda$	changes in wavelengths
ρ	charge density
B	magnetic induction
D	electric displacement
E	electric field
H	magnetic fields
J	urrent density
N	the total number of molecules
s	Sensitivity

Chapter 1

Introduction

1.1 Project Motivation

The amount of contamination in the different environmental compartments such as air, water and soil is increasingly alarming. Contamination in the aquatic environment significantly affects animals, human beings, farming and food production. Human activities contribute greatly to the release of contaminants into the environment e.g. waste dumping, domestic, industrial and agricultural waste. It is important to note that contamination is a serious concern at a time when ever increasing demand threatens water security.

Estrogens are biologically active hormones derived from humans, animals and also found in plants that can enter to the environment through wastewater treatment plants (WWTPs) or from agriculture operations (Figure 1.1). After the WWTPs, low concentrations of estrogen have been discovered in various water environments. Estrogens in the environment have been recognized as an important threat since they have been listed as endocrine disruptor compounds (EDC) and have the potential to lead to adverse major health effects, also causing some concern for drinking water contamination. In particular, they affect reproductive and developmental systems of both humans and animals. There is an increasing need for the development of sensitive biosensors for detection of estrogenic molecules.

Although the number of tools for analysing organic and inorganic contamination in water samples is extensive and sensitive, these instruments are laboratory-based. They are typically time consuming and labour-intensive. Further enforcement by environmental regulators will mean that rapid and accurate monitoring systems will soon be required. Therefore, there is a need for a low-cost, portable, rapid response indicator to detect the presence of the pollutant, which this research aims to provide.

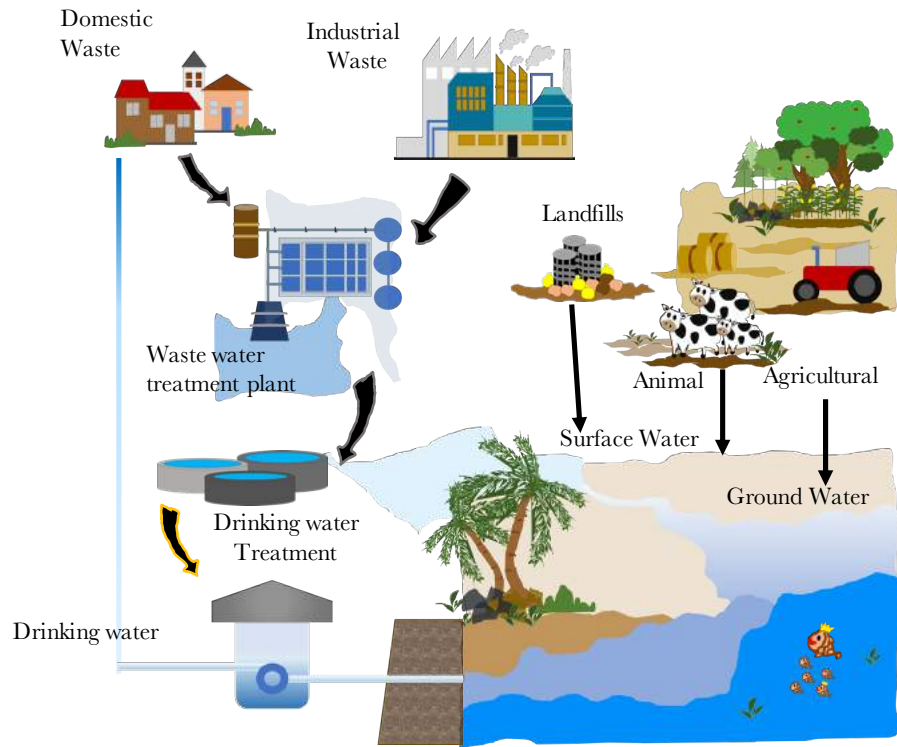


Figure 1.1: Illustration of main sources of estrogen in the water release into the environment [1]–[3].

Work on optical sensing techniques continues to advance – and optical sensing techniques and related technologies are becoming a well-established approach for *inter alia* applications in biomedical and environmental sensing. These have overcome the limitations of classical advanced analytical methods in terms of sensitivity and stability. Plasmonic devices, in particular, consist of metallic nanostructures that can sensitively measure changes in their surrounding material. Plasmonic sensors performance can be controlled through the geometry of the nanostructures and their optical properties. These properties include the physical dimensions and shape of the nanostructures, their periodicity and their constituent material. Additionally, the surface of the materials can be modified to have selective and specific affinity for biological or chemical substances. Advanced lithography technique also improves fabrication flexibility and facilitates the design of novel biosensors. Furthermore, plasmonic sensors can potentially be used in miniaturized and portable biosensing systems, such as lab-on-a-chip devices for medical and environmental applications that have a restricted sample volumes.

To start addressing these issues, this research presents the development of a plasmonic biosensor based on nanostructures for chemical sensing applications based on localized surface plasmon resonance. Designed tuning of reflection, transmission and

absorption resonances can be used to help identify specific molecules through selection of the known bond resonances of the molecules of interest while refractrometry sensing can be employed for quantification of concentrations.

1.2 Aim and Objectives

The aim of this study was to develop a novel plasmonic biosensor that will specifically detect estrogenic hormones (analytes) in water that are detrimental to humans and animals. The specific objectives were to:

1. Perform simulation, fabrication and characterisation asymmetric split-H (ASH) gold nanostructures on a dielectric substrate to produce double resonance peaks to be matched with the infrared vibrational energies of the bonds in the targeted molecules.
2. Tune the plasmonic resonances of ASH nanostructures to match with the molecular vibration resonances of estrogenic hormones, namely Estrone (E1), 17β -Estradiol (E2), Estriol (E3) and 17α -Ethinyl Estradiol (EE2), simultaneously detect the hormones in mixtures and quantify their molar fraction.
3. Functionalize ASH nanostructure surface with a specific bio-recognition element which will be used to bind with the 17β -Estradiol (E2) and test the sensing performance after functionalization.

1.3 Chapter summary and thesis outline

Chapter 1 is an introduction to this thesis providing short descriptions on the content, project motivations and contributions regarding developing plasmonic biosensors using metallic nanostructures for environmental sensing.

Chapter 2 is the literature review, explaining the state-of-the-art of sensors for environmental monitoring and the relevant theories and developments in the field of optical sensing. This chapter presents the overall research background of optical bio sensing using localized surface plasmon resonance with the operation of plasmonic nanostructures.

Chapter 3 provides the details on the methods used to model and fabricate the plasmonic nanostructures. The fabrication process was carried out using electron beam lithography and lift-off process. The explanations continue by showing the

measurement methods using Fourier transform infrared (FTIR) spectroscopy. This chapter also includes a description on characterization of the plasmonic nanostructures scanning electron microscopy and atomic force microscopy.

Chapter 4 describes the background in designing the asymmetric plasmonic nanostructures. This chapters also discusses on the various factors relevant for the design of the nanostructures such as the choice of the substrates. Modelling was carried out using the fused silica and ZnSe substrates. The nanostructures were physically optimised to produce plasmonic resonances at the targeted wavelengths of the molecular bonds of the targered analytes. Tuning the geometry and periodic arrangement lead to achieve a narrow resonance and high amplitude. This chapter include an overview of the characteristics of optical sensing using plasmonic nanostructures.

Chapter 5 describes the four most common estrogenic hormones in the environment, Estrone (E1), 17β -Estradiol (E2), Estriol (E3) and 17α -Ethinyl Estradiol (EE2) were deposited on the bare substrates and on gold nanostructures. The enhancement results and the resonance shifts were compared and calculated. The plasmonic resonances produced have been tuned to match with the molecular vibration resonance of the four estrogens. The sensing experimentation was presented in this chapter. Additionally, mixtures of two hormones were also deposited on the nanostructures and the responses were characterised.

Chapter 6 investigates the use of the aptamers, a deoxyribonucleic acid (DNA) as the biorecognition element with high affinity and specific binding to E2. This chapter also presents the approaches for the immobilization of the aptamers on the gold surface. After functionalizing the surface sensor with aptamers, sensitivity curves were produced by addition increasing concentrations of E2.

Chapter 7 is a summary of the work. The strengths and the weaknesses of the work are summarised and there is a discussion on potential future works that can be implemented as the continuation of this project.

Chapter 2

Research background and theory

2.1 Introduction

This chapter relates the most important research and theories relevant to better understand and apply the different advanced techniques behind plasmonic-based sensing using aptamer functionalised gold nanostructures for environmental monitoring. The need for environmental biosensors is explained and the latest advancement on optical environmental biosensors are presented. Notably, the use of aptamers as a bio-recognition elements has become increasingly important to develop specific biosensors also known as aptasensors. Following on this, brief explanations on the working principles of the surface plasmon and localized surface plasmon are also discussed and localized surface plasmon resonance (LSPR) sensing, both refractive index and the surface enhanced infrared absorption (SEIRA) sensing, are presented in more details. This chapter also provides a review of the state-of-the art of biosensors for environmental monitoring especially in the aquatic environment.

2.2 Environmental Biosensors

2.2.1 The need for environmental biosensors

As population levels increase towards 9 billion in 2050, water security has become increasingly important. One important aspect of water security is ensuring the continuing supply of drinking water that is sustainable, safe and free from contamination. Increasing water demand means that the use of reclaimed water, i.e. treated wastewater, is more and more common. It is therefore crucial to ensure that all contamination: organic and biologic be remediated prior to distribution. In the last few decades, concerns have been raised over the ubiquity of new biologically active compounds in waterways and the marine environment. The concentrations of these xenobiotics compounds in various environmental compartments (water, sed-

iment, plants and animals) are ever-increasing and their ecological effects are not yet fully characterised. They have been labelled “contaminants of emerging concerns” (CECs). CECs arrive in the aquatic environment via the effluent of municipal wastewater treatment plants (WWTPs) after incomplete removal. Reclaimed water has, therefore, the potential to be contaminated, although at trace levels, with CECs and the effect on human health of low concentration, chronic exposure to a mixture of chemicals is yet unknown. There is a pressing need, therefore, to develop and implement fast and sensitive detection methods for these compounds in wastewater and surface waters. Classical advanced analytical methods such as gas chromatography or high-performance liquid chromatography coupled with mass spectrometry have very low detection limit for CECs and have been successful for their detection in various water samples (surface, ground and drinking water). These methods, however, including sample preparation, are labour intensive, time-consuming and expensive. They are thus not adapted for real-time, high frequency, on-site monitoring of environmental contaminants. In fields such as biomedical engineering, food safety and drug development, biosensors have already been widely employed because of their many favourable characteristics: small foot-print, low cost, ease-of-use, specificity and sensitivity; however, their deployment in environmental monitoring and early warning systems are still limited [1].

2.2.2 Definition of biosensor

A biosensor is an analytical device that is capable of detecting organic biological or chemical species and producing a signal depending on its concentration. According to IUPAC nomenclature, a biosensor is a “device that uses specific biochemical reactions mediated by isolated enzymes, immunosystems, tissues, organelles or whole cells to detect chemical compounds usually by electrical, thermal or optical signals” [2]. Biosensors are composed of three components: a biological sensing element, a transducer and the processing of the signal (Figure 2.1). The transducers can be based on different principles such as optical, mechanical, electrochemical, or yet piezoelectric. The specificity and selectivity of the biosensor are determined by the properties of the biological recognition element. The bio-recognition elements or bioreceptors are key components that are immobilized at the biosensor surface and specifically bind to the target analyte. Biomolecules are used to bind the target molecules, for example, nucleic acids, enzymes, antibodies, aptamers, molecularly imprinted polymers (MIPs) [3]. The transducer as a quantifiable signalling component will transfer the signal from the interaction of the bio-recognition element into an optical, electrical or mechanical signal that can be measured or quantified. The output signal from the transducer will be passed to the amplifier for amplification

and the signal will be processed to produce a user-friendly reading.

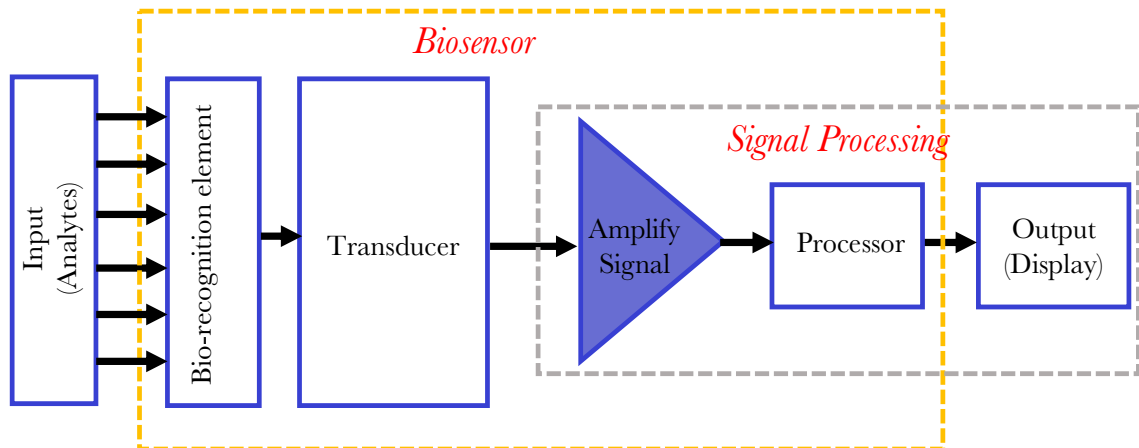


Figure 2.1: Biosensor block diagram. Biosensor consists of biorecognition elements, transducer and the signal processing.

2.2.3 State-of-the-art for estrogen biosensors

2.2.3.1 Estrogenic contaminations

Estrogen; either the natural or synthetic estrogens are important amongst CECs as they are endocrine-disrupting chemicals (EDC). They have been detected in numerous studies of wastewater influents and effluents. They are known to be the main causative agents for reported abnormalities in reproductive and developmental systems of both humans and animals. This is lead to “testicular feminisation” in fish and male infertility in humans and also cancers and bone disorders [4], [5]. Intensive agricultural industry and incomplete removal by WWTPs leads to their introduction in surface water and potentially to drinking water sources. They have been detected down to the low ng/L level in surface, ground and drinking water (Table 2.1). In 2015, the European Union published a watch list of substances that may pose a significant risk to the aquatic environment [6]. These include several EDCs, notably the natural estrogen, 17β -estradiol (E2), estrone (E1), and the synthetic 17α -ethinylestradiol (EE2) from medications like contraceptive pills. Once added to the regulated contaminant lists, water companies will have to comply and remediate them in WWTPs to acceptable levels within a very short amount of time (by 2021).

Table 2.1: Maximum and minimum concentration of natural estrogens in water samples (E1, E2 and E3 (estriol)) - NM: not measured; ND: Not Detected; ¹Concentrated Animal Feeding Operation, ²Sewage Treatment Works [Adapted from Sarah Jane Haig Thesis, (2014) [7]].

Location	Sample type	E1 (ng/L)	E2 (ng/L)	E3 (ng/L)	Ref
China	Pearl and Liao River	0 – 78.7	0.9 – 7.7	NM	[8], [9]
Germany	River water (31 samples)	0.1 – 18	0.15 – 5.2	NM	[10]
Japan	Tama River	0.01 – 85.6	0.01 – 12.3	NM	[9]
Netherlands	Coastal/Estuarine water(11 samples)	0.1 – 3.4	0.3 – 5.5	0.1 – 4.3	[11]
UK	River water (28 Sites)	0.07 – 3.33	0 – 0.9	0 – 1.2	[12]
USA	River water (139 Sites)	< 5 – 112	< 5 – 93	< 5 – 51	[13]
USA	Mississippi River	0.02 – 4.7	0.02 – 4.5	NM	[14]
USA	Drinking water (10 samples)	0.03 – 0.1	0.01 – 0.02	0.01 – 0.02	[15]
Taiwan	Wulo Creek-downstream of CAFO ¹ (54 samples)	7.4 – 1267	9.3 – 313.6	0 – 210	[16]
UK	River downstream of farm runoff (25 samples)	1.46 – 9.31	0.69 – 3.62	NM	[17]
UK	Poultry litter (runoff)	32.5 – 3500	NM	NM	[18]
USA	8 CAFO (swine lagoon)	1100 – 17400	194 – 3900	47 – 6290	[19]
USA	8 CAFO (cattle lagoon)	20 – 102	8 – 200	ND	[19]
Canada	Effluent from STW ²	2.5 – 82.1	0.44 – 3.3	0.43 – 18	[20]
Germany	Effluent from STW ²	1 – 70	< 1 – 3	NM	[21]
Germany	15 Rivers subjected to STW ² discharge	< 0.1 – 1.6	NM	NM	[21]
Spain	Effluent from STW ²	< 0.2 – 1.8	ND	NM	[22]
Spain	Llobregat Rivers subjected to STW ² discharge	0.7 – 1	ND	NM	[22]
UK	Effluent from 3 STW ²	< 0.4 – 12.2	< 0.4 – 4.3	NM	[23]
UK	River subjected to STW ² discharge	< 0.4 – 2.5	< 0.4 – 2.3	NM	[23]

2.2.3.2 Estrogen environmental sensors

To ensure the safety of human and environment, a number of techniques for detection of EDCs have been reported. Biosensors are a potential technology that can be useful for continuous monitoring of potentially contaminated areas.

A study by Kushwaha *et al.* (2014) have reported exploiting graphene oxides (GO) based on FRET (fluorescent resonance energy transfer) sensor to sense estriol (E3) with the lowest limit detection of 1.3 nM [24]. The fluorescence intensity of the mixture (GO, E3, GO-estriol complex solution) is measured using a luminescence spectrometer. The different concentration of E3 from 0 nM to 10 nM were evaluated and the emission intensity peak was rapidly increased after the addition of GO in the solution of E3. The specificity of the devices also has been tested with the influence of glucose, vitamin C and simulated body fluid, where the 90% peak intensity of E3 was observed compared to other molecules. Fourier transform infrared spectroscopy (FTIR) was also used to determine the functional group of GO-estriol complex solution.

Previously, Dai *et al.* (2017) demonstrated the detection of 17 β -Estradiol in environmental samples using a single used biosensor based on electrochemical transduction mechanism of differential pulse voltammetry (DPV) [25]. The three-gold electrode configuration was fabricated and functionalized with 3-mercaptopropionic acid (MPA) to attach the anti-estrogen receptor. The influence of K₃Fe(CN)₆/K₄Fe(CN)₆ redox coupling reaction with 17 β -estradiol (E2) antigen were used as the biorecognition element with the estrogen receptor α (ER- α). The antibody and antigen are in a “lock and key” mechanism as the specificity of the biosensor. The K₃Fe(CN)₆/K₄Fe(CN)₆ was prepared and added on top of the gold electrode before the measurement is taken. They have tested and showed the performance of the devices with regular tap water from the Cleveland regional water district (US) and simulated urine test sample, with concentrations between 2.25 pg/mL and 2250 pg/ml. Singh *et al.* (2017) developed capacitive immunosensors to detect E2 in water samples and reached a limit of detection is 1 pg/mL. The two electrodes were fabricated and functionalized with monoclonal antibody (mAb) specific to E2 using a monolayer of 11-mercaptopundecanoic acid (11-MUA) [26]. Zhang *et al.* (2014) reported on an electrochemical sensor based on the electropolymerized molecular imprinted polymers (MIP) with electrodeposited AuNPs amplification for detection of E2 in milk samples that exhibited a detection limit of 1.28×10^{-12} mg/ml [27]. Florea *et al.* (2015) also demonstrated a sensitive electrochemical MIP sensor to analyse river water samples collected from the Rhone River [28]. The gold nanoparticles on

Table 2.2: Types of biosensor available on the environmental sensing. All the range unit in the table have been converted to pg/ml.

Transducer	Bioreceptor	Analyte	Range (pg/ml)	LOD (pg/ml)	Ref
Electrochemical (Capacitive)	Antibodies	E2	1 – 200	1	[26]
Electrochemical (DPV)	Antibodies	E2	2.25 – 2250	1	[25]
Electrochemical	MIP	E2	0.001 – 100	1.28×10^{-3}	[27]
Electrochemical	Aptamers	E2	27.3 – 27238	35.4	[31]
Optical (FRET)	GO	E3	374.9 – 2883.8	374.9	[24]
Optical (SPR)	Antibodies	E2	$1950 – 2000 \times 10^3$	810	[30]
Optical (SERS)	Antibodies	E2	0.1 – 1000	0.65	[29]

the gold electrodes were functionalized with potentiodynamic electropolymerization containing p-amino thiophenol. The sensor exhibits a broad linear range from 3.6 fM to 3.6 nM and a limit quantification of 1.09 fM.

Wang *et al.* (2016) used surface-enhance Raman scattering (SERS)-based immunoassay using functional nanomaterials. E2 was successfully measured and the limit detection of E2 was 0.65 pg/ml in a range of 0.1 to 1000 pg/mL [29]. Jia *et al.* (2018) demonstrated the development of magnetic nanoparticles enhanced with SPR immunosensor for the quantification of E2 with the anti-17 β -estradiol monoclonal antibody (E2-mAb) [30]. E2 spiked in milk samples was detected in the range of 1.95 to 2000 ng/mL and the limit detection was 0.81 ng/mL. Currently, the detection of 17 β -estradiol performed using an aptamer (anti- 17 β -estradiol as bio-recognition element increased rapidly. Details are provided in section 6.2 and chapter 6.

The choice of transducers depends on the signal generated by the interaction of the bio-recognition elements and the analytes. Transducers can mainly be divided into electrochemical, mechanical and optical transduction. The work in this thesis is mainly focused on optical transduction, using the plasmonic properties of metamaterials, measuring the changes in the optical properties in the presence of analytes either in absorption, transmittance, reflectance or emission that can be recorded by a photodetector. In general, plasmonic biosensors consist of a light source, a plasmonic transducer, and a detector.

2.3 Plasmonic-based sensing

Plasmonic-based sensors are optical sensors that rely on plasmons, the excited electrons, in a metal thin film, in metal nanoparticles or in nanostructure surfaces. These properties make the plasmonic sensors a platform for low-cost point of care diagnostic devices when integrated of in a microfluidic system. Currently, plasmonic is an important field due to the advances in nanofabrication technologies that allow the researchers to precisely tune over the geometry and the optical properties of the materials. Also, it provides techniques with high sensitivity and can be utilized outside of the laboratory. Plasmonic-based sensing can be divided into two categories of excitation; surface plasmon resonance (SPRs) and localized surface plasmon resonance (LSPRs). The more common LSPR sensing, based on metal nanostructures (typically gold and silver) deposited on dielectric substrates (metal-dielectric interfaces), lies in the visible or near-infrared region but also can be excited in different wavelengths depending on the geometry sizes. LSPR sensing offers many advantages due to its spectral enhancement and dependence on the surrounding medium along with several additional benefits, particularly in higher throughput screening sensing applications. It was utilized for the first time by Englebienne *et al.* (1998) in biosensing [32].

2.3.1 Electromagnetic theory and dielectric properties

Maxwell's equations are composed of four equations based on Gauss law, Faraday law, Ampere's law and Poisson and Laplace equations and describe the propagation and interactions between the electric and magnetic fields. The Maxwell equations below are expressed in the differential equations form:

$$\text{Gauss' Law} \qquad \qquad \qquad \nabla \cdot D = \rho \qquad \qquad (2.1)$$

$$\text{Gauss' Law for magnetism} \qquad \qquad \qquad \nabla \cdot B = 0 \qquad \qquad (2.2)$$

$$\text{Faraday's Law} \qquad \qquad \qquad \nabla \times E = -\frac{\partial B}{\partial t} \qquad \qquad (2.3)$$

$$\text{Ampere's Law} \qquad \qquad \qquad \nabla \times E = J + \frac{\partial D}{\partial t} \qquad \qquad (2.4)$$

Where E is denotes the electric field, D is electric displacement, H is magnetic fields, B is magnetic induction, J is current density, and ρ is charge density [33]. In the isotropic, linear and homogeneous media, there is a following relations apply:

$$D = \varepsilon E + P = \varepsilon E \quad (2.5)$$

$$B = \mu H \quad (2.6)$$

$$J = \sigma E \quad (2.7)$$

Where P is polarisation, the constants ε , μ and σ are respectively, the electric permittivity (or dielectric value), magnetic permeability and conductivity of the material. ε can be decomposed into two components, ε_r the relative permittivity and ε_0 , the permittivity in free space and μ , into μ_r , the relative permeability, and μ_0 , the permeability in free space [33].

$$\varepsilon = \varepsilon_r \varepsilon_0 \quad (2.8)$$

$$\mu = \mu_r \mu_0 \quad (2.9)$$

2.3.2 Refractive index and Negative Refractive Index

Properties of a material are described by its ε , μ , and its refractive index, n . The refractive index (RI) of material is measured by a ratio between the phase velocity of the electromagnetic wave in a vacuum (c) and the phase velocity travelling through the particular materials (v).

$$n = \frac{c}{v} \quad (2.10)$$

Where c is the speed of light in medium and $c = \lambda \times f$ The refractive index of a particular material does not remain constant, but it will change depending on the wavelength of the incident wave. In isotropic medium, the refractive index given as;

$$n = \sqrt{\varepsilon_r \mu_r} \quad (2.11)$$

In real materials, the permittivity is complex and is frequency-dependent. n is the real part of the refractive index and κ is the extinction coefficient to indicate the amount of absorption loss when the electromagnetic wave propagates through the material.

$$n = n + i\kappa \quad (2.12)$$

In normal materials, both ε and μ are positive and these materials are known as right-handed material (RHM) (Figure 2.2(a)). However, combining magnetic and electric properties of an element in an appropriate structure will enable to exhibit negative values for ε and μ . V. G. Veselago (1967) was the first theoretical physicist to describe that negative values of dielectric constant and permeability could transmit light and coined the word ‘metamaterial’ for materials with such properties [34]. As such, ε and μ can thus be categorised in four quadrants being either both positive; both negative; ε positive and μ negative; or ε negative and μ positive. Left-handed materials (LHM) are defined as having either (but not both) ε or μ negative and have opposite properties to RHM (Figure 2.2(b)) i.e. the light flow is inverted when passing through the material. Some artificial metamaterials can have $\varepsilon < 0$ and $\mu < 0$ and because the product is positive, the refractive index, n is real [35].

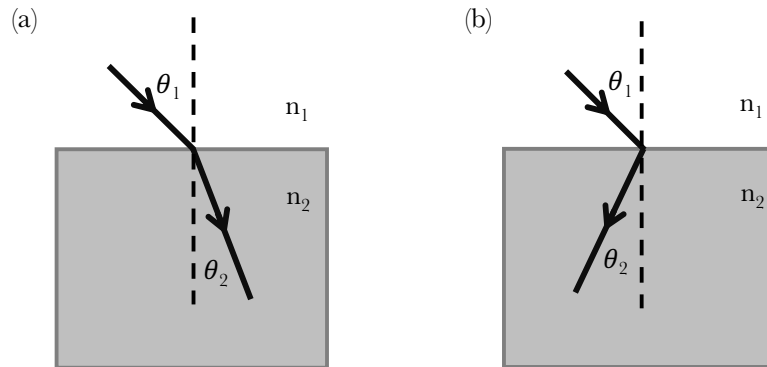


Figure 2.2: (a) Light refracted by a conventional material (b) light refracted by a material with a negative refractive index.

2.3.3 Plasmonic and surface plasmon resonance

Plasmonics is the study of electromagnetic responses at the interface between metals and dielectric materials. It describes the light localization and propagation at the subwavelength scales. Electromagnetic waves propagation in a direction parallel (along the x-axis) to the metal (conductor) and dielectric (insulator) interface will induce coherent delocalised oscillations of electrons of as shown in Figure 2.3 called

surface plasmons (SPs). This occurs because the real part of the dielectric function constant changes sign across the interface. The surface plasmon resonance (SPR) is sensitive to its immediate environment i.e. surrounding refractive index and can be used to measure the presence of analyte at the surface. When the dielectric is coated with a thin layer of metal, surface plasmon polaritons (SPPs) are produced as the combination of a surface plasmon and a photon propagating at the material interface (Figure 2.3(a)). SPPs are shorter in wavelength compared to the incident light. The excitation of the SPR film can be done through several methods, and the most common is using the Kretschmann configurations or prism coupling.

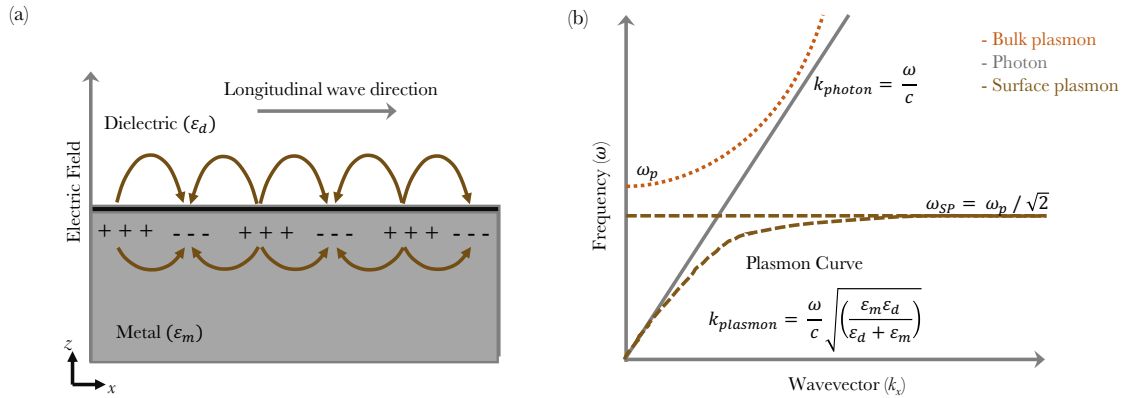


Figure 2.3: (a) Illustration of the surface plasmon propagating along the x -axis at the metal-dielectric interface. The electric field line is the z -direction. (b) Dispersion curve for surface plasmon polaritons; the grey straight line is the photon line in air, the brown dashed line is the SPP and the orange dotted line is the bulk plasmon. Where ω_p is the plasma frequency of free electrons in the metal, ω_{SP} is the surface plasmon frequency.

The expression for surface plasmon dispersion relation can be obtained by solving Maxwell's equations under the appropriate boundary conditions between the frequency and spatial wave number, which can be found as :

$$k_{plasmon} = \frac{\omega}{c} \sqrt{\frac{\epsilon_m \epsilon_d}{\epsilon_m + \epsilon_d}} \quad (2.13)$$

Where k_{photon} is the free space wave number, ϵ_d is the permittivity of the dielectric, and ϵ_m is the frequency dependent permittivity of the metal. For the SP to be possible the signs of ϵ_d and ϵ_m must have an opposite signs. The SPP wave vector $k_{plasmon}$ is plotted in Figure 2.3(b).

2.3.3.1 Metals and plasmons at optical frequencies

There are four metals with plasmonic behaviour at optical frequencies: gold (Au), silver (Ag), aluminium (Al) and copper (Cu). Plasmons can be described as a collective oscillation of the free electron density with respect to the fixed ions in a metal. They oscillate back and forth at the plasma frequency until it loses resistance (damping). The plasma oscillation frequency, (ω_p) , is defined as:

$$\omega_p = \sqrt{\frac{ne^2}{m_0\varepsilon_0}} \quad (2.14)$$

Where n is the electron density, e is the electron charge, m is the electron mass and ε_0 is the free space permittivity. These metals exhibit a negative real part of dielectric permittivity in the visible and near-IR regions. The complex dielectric functions can be defined as:

$$\varepsilon = \varepsilon_1 + i\varepsilon_2 \quad (2.15)$$

ε_0 is the dielectric constant and the real part ε_1 is the refraction of light, the imaginary part ε_2 is absorption. The plasmonic response of the material can be described by the Drude dielectric function with two parameters, the plasma frequency and the relaxation rate of free charge carriers. The Drude model was proposed by Paul Drude in 1900 to describe the optical properties of metal. The Drude model can be written as:

$$\varepsilon_m(\omega) = 1 - \frac{\omega_p^2}{\omega^2 + i\gamma\omega} \quad (2.16)$$

Where ω is the frequency of the incident light, ω_p is the plasma frequency, γ is the collision frequency (or also known as damping constant). Splitting $\varepsilon_m(\omega)$ into real and imaginary part gives:

$$\varepsilon_1(\omega) = 1 - \frac{\omega_p^2}{\omega^2 + \gamma^2} \quad (2.17)$$

$$\varepsilon_2(\omega) = \frac{\omega_p^2\gamma}{\omega(\omega^2 + \gamma^2)} \quad (2.18)$$

The movement of the electrons produced a vibration that creates the electromagnetic waves. For optical sensing applications, local heating of the plasmonic structures will change the refractive index and the sensitivity will depend on the polarization, geometry of the structures and intensity.

2.3.4 Localized surface plasmon resonance

The second fundamental type of plasmonic excitation is localized surface plasmon (LSP). When the metal dimensions are significantly smaller than the wavelength of the incident light, the SP wave cannot propagate further than the structural sizes; hence it becomes localized and leads the plasmon to oscillate around the metal. The excitation of the free electrons in the metal creates a collective oscillation limited to the boundaries of the geometry. These oscillations are the LSP as shown in Figure 2.4. Similar to SPR, the LSPR also is sensitive to the changes on the surrounding dielectric environment and can be manipulated by varying the metal shapes and sizes or using different metals.

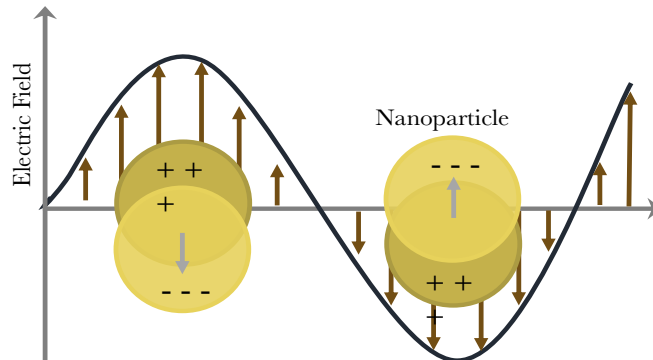


Figure 2.4: Schematic diagram of localized surface plasmon resonance on the nanoparticle surface showing the electron displacement [36].

2.3.5 Localized surface plasmon resonance sensing

Optical sensors convert light intensity into electronic signals. The plasmonic interaction between metal nanoparticles is very sensitive to their separation and the refractive index of the surrounding medium. The resonance can be shifted when there is an interaction between the metal and organic materials [37]. The plasmonic resonance can also be tuned by coupling effects, geometric sizes, periodic arrangement, and also surrounding dielectric environments [38]. Examples of applications of optical technologies that use enhanced light-matter interaction are surface enhancement Raman spectroscopy (SERS), surface-enhanced infrared absorption (SEIRA)

and photothermal induced resonance spectroscopy. The sensor performance can be evaluated by calculating the sensitivity (nm/RIU) and the figure of merit (FOM) as explained in the next section 2.3.6. In order to increase the performance of the devices, the total shift resonance should be maximized with as narrow a resonance linewidth as possible.

Both SPR and LSPR use the incident light to collectively excite the electrons in a metal and measure the changes in the local refractive index (Figure 2.5). In LSPR, the electromagnetic field is highly confined close to the metal surface and the sensitive area only expands a few nanometres from the surface (20 to 40 nm), whereas SPR evanescent decay expands several nanometres (250 to 1000 nm) resulting in high sensitivity to bulk refractive index changes.

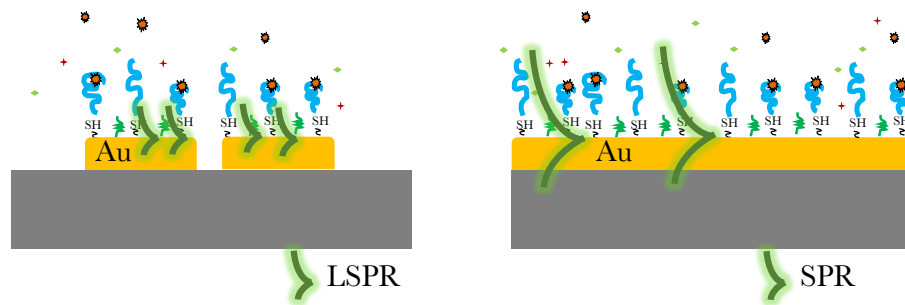


Figure 2.5: (a) LSPR (b) SPR configuration of the detection principle of plasmonic sensing.

LSPR is much less complex and the instrument can be made much smaller. Compared to a gold thin film, LSPR has smaller sensing volume that enables to be more sensitive to the molecular binding. LSPR allows to measure the small changes in the wavelength (spectral shifts) rather than looking at the angle change and no prism is needed to couple with the light Figure 2.6(a). Refractive index sensing is the simplest application of LSPR because changes in the refractive index of the surrounding environment induce shifts in the LSPR. SEIRA is another application of LSPR; molecular sensing happens by coupling between the molecular vibrational wavelengths with the LSPR as presented in Figure 2.6(b).

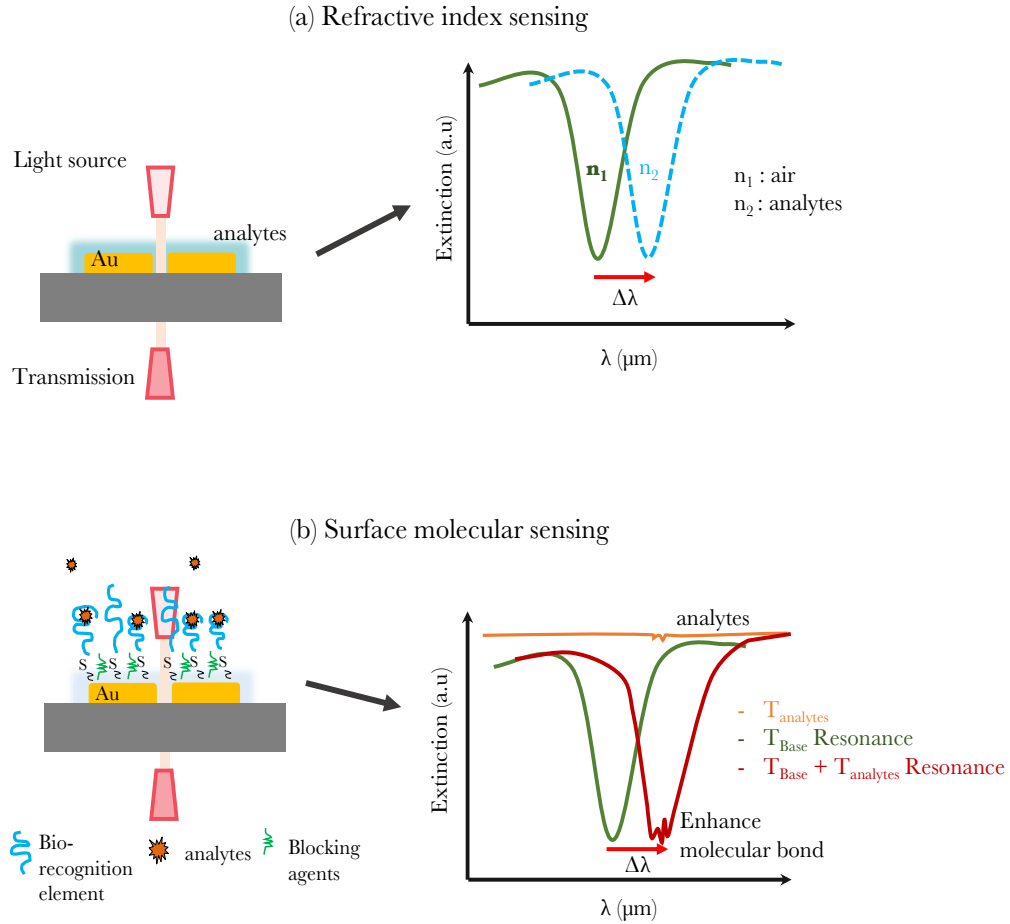


Figure 2.6: Illustration of plasmonic biosensor based on (a) refractive index sensing and (b) surface molecular sensing integrated with SEIRA.

The three main optical arrangements to generate the LSPR signal are transmission, reflection and dark-field microscopy since there is no bulky coupling method needed. Transmission measurement is the most straight-forward. The sample is placed between the source and the detector and the light is passed through the sample. The transmitted light is measured and produced the recorded wavelengths. Compared to transmission, reflection measurements are good for non-transparent samples and the wavelengths are recorded by taking the measurement of the light reflected from the samples.

2.3.6 Characterization of the LSPR sensing

The detection principle in LSPR sensors is based on the peak intensity or wavelength shift. The performance of the sensor can be assessed by determine the sensitivity (s) and the Figure of Merit (FOM). Sensitivity (s) is defined as the ratio of wavelength shifts in position or intensity to the changes of the refractive index of a dielectric medium. Increasing the dielectric constants of the environments will leads to a

redshift (lower frequency) and decreasing the sizes of the particles will leads to a blueshift (higher frequency). The sensitivity of the structures can be calculated using the formula below [38]:

$$s = \frac{\Delta\lambda}{\Delta n}(nm/RIU) \quad (2.19)$$

$$s = \frac{\Delta I}{\Delta n}(RIU^{-1}) \quad (2.20)$$

Δn is the changes in refractive index, $\Delta\lambda$ is the changes in wavelengths and ΔI is the changes in peak intensity. RIU is for Refractive Index Unit. The figure of merit (FOM) also can be calculated using the terms of sensitivity [38]. Therefore, in order to increase the FOM, the total wavelength shifts $\Delta\lambda$ must be larger and narrower the line width of the resonance.

$$FOM = \frac{s}{FWHM} \quad (2.21)$$

Vibrational wavelengths of many molecular bonds of organic compounds can be found in the infrared range. A higher sensing performance can be achieved by enhancing the signal of a particular vibrational mode of analyte in the infrared spectra. In this case, infrared spectra are used as a reference to tune the resonance peaks to match with the molecular bond resonances of the analyte. Infrared spectra can be split into three regions; near IR (13 000 – 4000 cm^{-1}), mid IR (4000 – 400 cm^{-1}) and far IR (<400 cm^{-1}) [39]. In the mid-IR spectrum, it divides into another four regions; X-H stretching region, triple bond, double bond and fingerprint region. Matching the LSPR to the molecular bond resonances is achieved by controlling and changing the geometric sizes of nanostructures (SEIRA).

It is also important to locate where the electric field intensity in the structure is greatest to detect small amounts of organic materials. The electric field intensity for the resonator can be high, at the corners of the structures compare to other parts and are known as “hot spots” [40]. The molecular detection at a specific hotspot can improve the detection. The enhancement factor (EF) can be calculated from electric field plot simulation results by comparing the ratio of resonance enhanced signals to signals from the organic materials alone [41]:

$$EF = \frac{\Delta R_2/N_2}{\Delta R_1/N_1} \quad (2.22)$$

N is the total number of molecules and ΔR is the relative change in the reflectance. N_1 and ΔR_1 correspond to measurements on unstructured surfaces produced by molecular resonance. N_2 and ΔR_2 correspond to the surface covered with an array of plasmonic structure. The enhancement factor needs to be calculated with caution as it relies on an estimate influence of the size of the hot spot compared to the amount of material deposited on a bare substrate.

2.3.7 Metal plasmonic nanostructures

Many unique optical properties can be achieved when adjusting the structures size and composition of the metal. Split ring resonators (SRR) are most commonly used as metamaterial structures since Pendry *et al.* proposed structures with smaller than wavelength dimensions (Figure 2.7) in late 1999. They suggested that an array of ring resonators features with a small gap ('C' shape) could respond to the magnetic component of light and could provide negative permeability [42]. When combined with thin wires to provide negative permittivity a double negative material can be produced that can demonstrate negative refraction. The periodic structures are defined by a unit cell of the characteristic dimensions a , with $a \ll \lambda$, where λ is the operating wavelength in the electromagnetic field. In 2000, Smith *et al.* designed such a structure of SRR operating in the GHz range and demonstrated negative refraction in numerical simulation and in experiments [43]. These double negative properties are not required for the sensing applications described here.

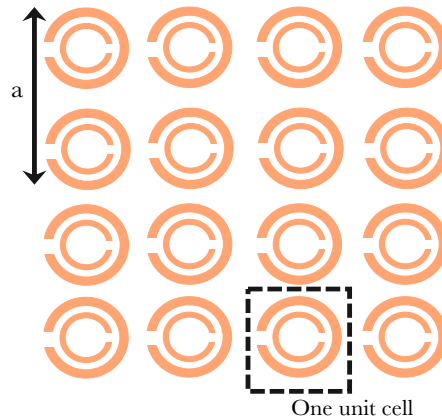


Figure 2.7: The plan view of a split ring structure in a square array, lattice spacing, a by Pendry *et al.* [42].

The SRR can be constructed in two different types described as ‘C’ or ‘U’ shaped, also single or double (Figure 2.7). It can act as an LC oscillating circuit containing a magnetic coil of conductance (L) and capacitor of capacitance (C) of the circuit where the resonant frequency of the LC resonance is given $\omega_{LC}=1/\sqrt{LC}$ [44]. The resonance can be changed by manipulating its geometrical parameters either in symmetric or asymmetric structures. The purpose of small gaps in between the rings is to produce large capacitance values, which lower the resonance frequency. When the dimension of the ring is also smaller than the wavelength; the losses become smaller and make the Q-factors larger [42]. The SRRs provide strong magnetic responses with negative permeability where is required to achieve negative index of refraction [43]. The above magnetic resonances or so-called LC resonances are different to the generally shorter wavelength (higher frequency) plasmonic resonances.

In electromagnetism (EM), both the electric and magnetic fields are transverse waves which can be divided into three modes; transverse electric and magnetic (TEM), transverse electric (TE) and transverse magnetic (TM). Transverse modes occur because of boundary conditions imposed on the wave by waveguide. In the TE mode no electric fields exist in the direction of propagation and in the TM mode a magnetic field does not exist in the direction of propagation [33].

The SRR can be polarized in two different directions depending on the electromagnetic responses either TE or TM. During the normal incidence, in Figure 2.8(a), the TE polarization modes (parallel with x axis) will across the gap in between of SRR and interacts with external fields to generate magnetic resonance called as LC resonance at the longer wavelength. Figure 2.8(b) shows, the TM occur when the magnetic fields parallel with SRR (parallel with Y axis) and electric field cannot be coupled with capacitance of SRR generates as plasmon resonance at shorter wavelength [44]. This theory has been experimentally demonstrated by Linden *et al.* with U-shaped gold structures in THz range [45].

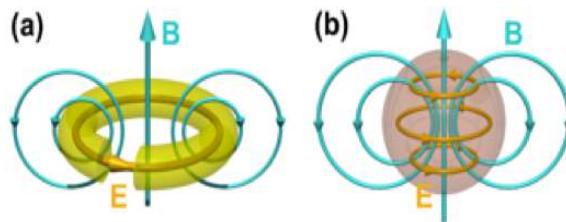


Figure 2.8: Schematic representation of (a) electric and (b) magnetic field distribution inside a metallic split-ring resonator. (Figure where reprint from the published paper [46]).

In the paper by Rockstuhl *et al.* (2006) [47], the SRR structures in near-IR have been characterized by adjusting the size of the gap and width with a periodicity of 500 nm. The SRR structure used gold on top of the quartz substrate with the parameters; height 20 nm and width of 60 nm. By opening the gap of SRR from 0 to 280 nm the results showed two major changes in the resonance. The larger the gap width in the structure, the LC resonance moves to higher frequency and for small gap it will appear at the lower frequency due to lower capacitance as the gap widens.

2.3.8 Examples of LSPR sensing

Although the literature often highlights the potential of LSPR sensors for environmental samples, there are a very limited report of such sensors compared to the LSPR sensors in medical and diagnosis tool applications.

Endo *et al.* (2005) developed label-free optical biosensors for monitoring the interaction with biomolecules that has a potential impact on the medical and environmental applications [48]. The LSPR biosensors with gold-capped nanoparticles layer substrate were utilized to detect the peptide nucleic acids (PNA)-DNA hybridization. The optical properties were characterized by transmission measurement and the limit of detection of 0.677 pM was achieved. Kim *et al.* (2019) demonstrated a nanopatterned fibre optic LSPR (FO LSPR) biosensor fabricated by focused ion beam (FIB) nanopatterning lithography [49]. Prostate-specific antigen (PSA) immunoassay is performed using FO LSPR to verify the fabricated sensor system as a biosensor. After the immobilization of the PSA antibodies, the FO LSPR sensors were reacted with various concentration of antigen and the LOD was 0.1 pg/ml.

Optical sensors based on plasmonic nanostructures have been introduced to provide high sensitivity with compact size [50]. The plasmonic resonances in these structures can be tuned to the spectral regions of interest with high spatial reproducibility. By applying an organic analyte on the metal-air interface of the metamaterial structures, the characteristic molecular vibrations of the analyte material can be detected and enhanced if they coincide with the plasmonic resonant wavelengths. The resultant red shift in the plasmonic resonance can be measured and used to calculate the sensitivity for use as an optical biosensor [51]–[53]. This plasmonic resonant coupling approach is known as surface-enhanced infrared absorption (SEIRA). Early work has been demonstrated by Neubrech *et al.* in 2008 that introduced the resonant coupling between nanorods and a nanometre thick layer of self-assembled monolayer octadecanethiol (ODT). The molecular signals of the ODT

are strongly enhanced when coupling with the plasmonic resonant and Fano resonance behaviour occurs [54]. Later work using the same detection molecules of ODT with split ring resonator was proposed by Cubukcu *et al.* and Wu *et al.* [55], [56]. Pryce *et al.* [41] have demonstrated the use of both SEIRA and refractive index sensing on a coupled split-ring resonators. Mbomson *et al.* [57] introduced asymmetric split-H (ASH) resonators on a silica substrate that produced a narrow band plasmonic resonances at a mid-infrared wavelength and provided the high enhancement factor required in SEIRA. The ASH plasmonic resonances coupled with the vibrational resonance of C-H bonds of the molecule 17 β -Estradiol. A high sensitivity value on the refractive index sensing 2335 nm/RIU was achieved. This technique also has been shown for several types of molecules organic; proteins, non-biological, organic thin-film and doping the metal oxide [57]–[60].

Recently, plasmonic biosensors utilizing various metallic structures have been demonstrated to realize SEIRA of biomolecules in aqueous solutions. Cetin *et al.* [61] introduced a biosensing platform using plasmonic gold nanohole arrays on a hybrid substrate. A limit of detection of 2×10^{-15} RIU was achieved for the refractive index change of a protein bilayer (protein A/G and protein IgG) which selectively bound on the gold nanohole. They also demonstrated the real-time detection of protein binding kinetics at the lowest concentration of 0.7 ng/mL using the plasmonic biosensors integrated with a microfluidic channel. Limaj *et al.* [62] developed an IR plasmonic biosensor based on gold nanoantennas fabricated on a CaF₂ substrate and sealed in a poly(dimethylsiloxane) (PDMS) fluidic chamber for chemical-specific detection and monitoring of a bilayer lipid membranes. The systems show the biosensor can be engineered to the targeted molecules by observing the two absorption bands of the molecular bonds of CH₂ of the lipids located at 2855 and 2927 cm⁻¹.

2.4 Bio-recognition

The choices of biorecognition elements are important and key factors include high affinity, stability, specificity and availability of the functional groups. Enzymes and antibodies are the most used bioreceptors due to their exceptional specificity and sensitivity. Currently, the usage of aptamer as a bio-recognition element is increasing rapidly. The word aptamer is derived from the Latin word “aptus” (to fit) as artificial specific oligonucleotides are selected for a particular target [63], [64]. Aptamers are single-stranded deoxyribonucleic acid (DNA) or ribonucleic acid (RNA) that can bind to their targets such as organic and inorganic compounds with high specificity and high binding affinity (Figure 2.9). The values of the dissociation constant (K_D)

of an aptamer with its target molecule are in the nanomolar and picomolar range. Aptamers can be a useful alternative to antibodies as a sensing molecule due to their stability. Specific aptamers are selected from large oligonucleotide libraries, using the Systematic Evolution of Ligands by Exponential enrichment (SELEX) process to the specific target [1]. Aptamers have the ability to fold into three-dimensional structures and interact with their targets by complementary shape [65]. Specifically, aptamers are flexible structures that are considerably smaller than antibodies. Aptamers are 6 to 30 kDa big with diameters smaller than 5 nm while antibodies are 150 to 180 kDa big with 15 nm diameters (Figure 2.9) [66], [67]. Furthermore, they are synthesised *in vitro* not *in vivo*, with very low batch-to-batch variation in production. Aptamers are easily modified and very chemically stable so that they can be used multiple times, hence their lifetime is much longer than antibodies [65]. Aptamers have been selected for a wide range of targets such as small organic molecules, metal ions, organic dyes, proteins and also peptides. Aptamers can adopt several 3D conformations: pseudoknot, G-quadruple, stem-loop and also hairpin [68]. Immobilization of biorecognition element can be done by physisorption or chemisorption that will be explained in section 2.4.3.

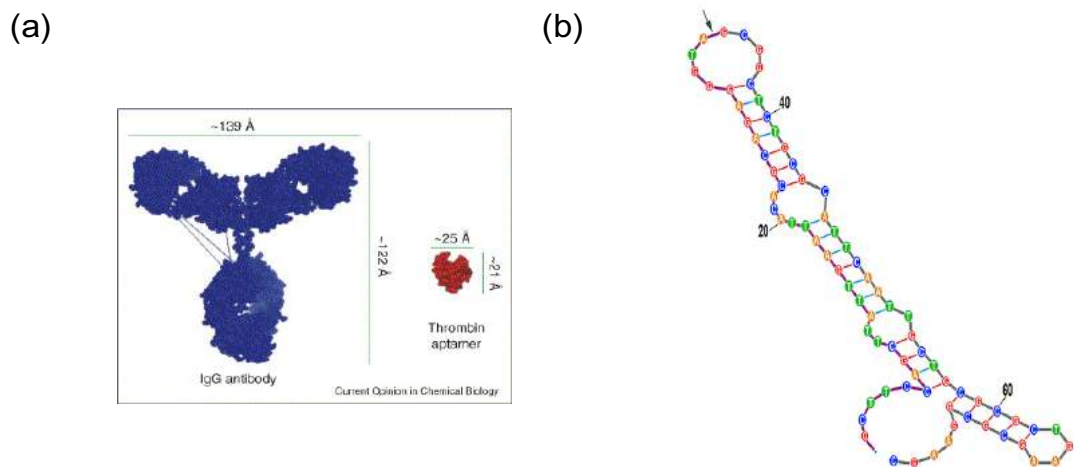


Figure 2.9: (a) The size comparison between the IgG antibody and the thrombin aptamer. (b) The secondary structure of DNA aptamer by Kim *et al.* used in this study. (Figure adapted from the published paper [31], [69]).

2.4.1 Aptamer production

The SELEX process involves an *in vitro* selection procedure including target binding, partitioning, amplification and conditioning (Figure 2.10). Aptamers are selected from the starting pool (library) consists of 10^{12} to 10^{16} different oligonucleotides with a random sequence [65]. The process starts with a nucleic acid library to find the best fitter or bind to the specific regions of the target through the selection

process by incubating together with a target molecule. The initial library is constituted of randomly generated sequences using the four possible nucleotides: cytosine [C], guanine [G], adenine [A] or thymine [T]. The binding involves with hydrogen bonds, salt bridges and van der Waals, hydrophobic and electrostatic interactions. The partitioning phase of the unbound molecules are separated and washed away and the specific bound sequences are retained with the bound molecules. The bound molecules were eluted from the target molecules and amplified by polymerase chain reaction (PCR) amplification or reverse transcription. This resulting in the double-stranded DNA transformed into the enriched oligonucleotides pool by separating the single-stranded DNA. The process is repeated usually 6 to 12 times through the steps 1 to 3 using the enriched oligonucleotide pool. The aptamer from the SELEX process are generally have 70 to 80 mer [64].

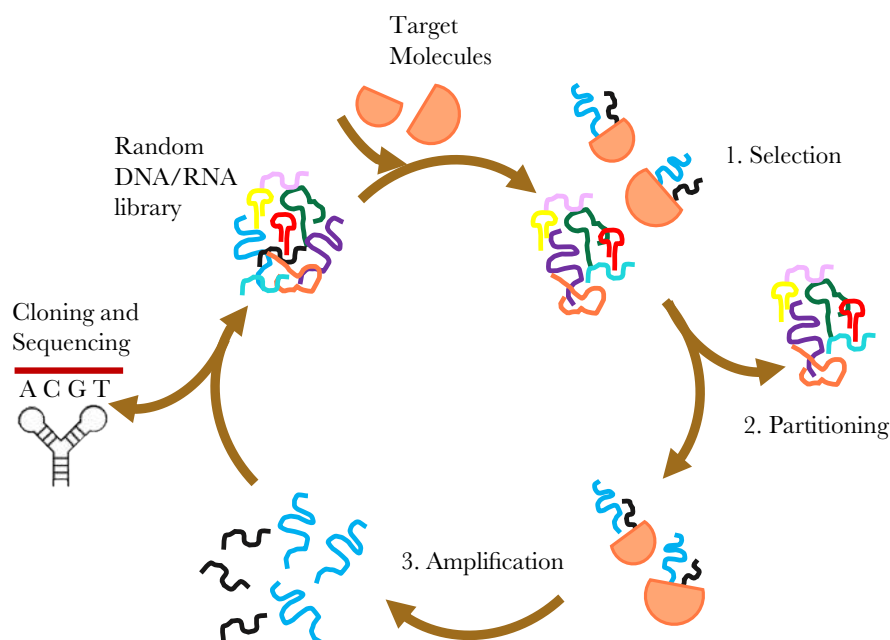


Figure 2.10: Schematic figure of the SELEX process (Figure adapted from the published paper [65]).

2.4.2 Label-free and labelled biosensor

Label-free methods provide simple, cost-effective and rapid measurements usually based on physical parameter detections such as molecular weight and refractive index. These methods enable the real-time monitoring of the binding reaction to the targets. Label-based biosensors usually used fluorescence tags to produce light at a given wavelength when the molecule of interest binds to the biomolecule. However, label based detection is high cost and possible to have modification or interaction with the bioreceptor. Other label types are chemiluminescent labelling, radiolabelling, enzymes or isotopic labelling.

2.4.3 Surface modification

Spin coating and vapour deposition that are used for surface film produced films substantially thicker than a monolayer. To attach the bio-recognition element, there is a method known as surface modification that enables to form a monolayer. Surface modification helps in enhancing bioactivities, improving the adhesion properties, providing optimum orientations of binding sites and also improving the electrical conductivities and optical properties of a surface. Surface modification processes can be classified into two categories. The first category is physisorption and involves a weak attraction between the surface substrate and the surface modifier. Physisorption is represented as the most simple and straightforward functionalization methods (noncovalent bonding) utilizing a combination of Van der Waals and hydrophobic forces. However, this method produces a loss and reductions in biological activities. The second category, chemisorption is a method involving strong surface bonds and usually using covalent bonding attraction mostly known as surface functionalization. It helps to overcome the issues associated with physisorption. The surface functionalization introduces a chemical functional group to be bound with the surface. Gold surfaces have a high affinity for thiol (SH) group while silica and silicon show high affinity for silane groups (Si-O). The most common method to functionalize the gold surface is by the usage of the thiol-chemistry. Both of this group can form a self-assembled monolayer (SAM). The thickness of the layer mainly ranges from 2 nm to 10 nm thick and the functionalized molecules depend on the type of solutions, solution concentration, immersion times and the chain length of molecules.

The aptamer can be immobilized on a gold surface by having the thiol group attached to the 5' end (Figure 2.11) to maintain the binding affinity and selectivity of the aptamer in a solution. Further explanation of the aptamer immobilization can be found in Chapter 6 section 6.3.3.

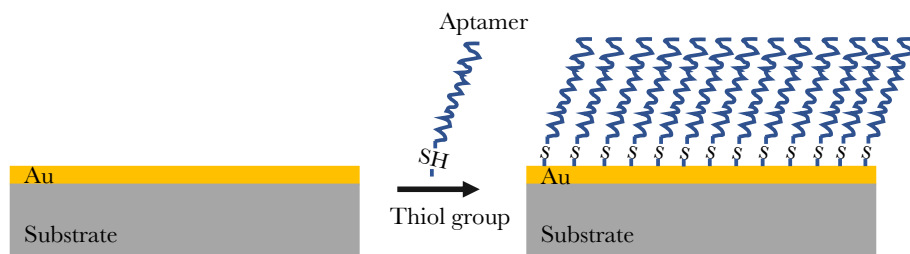


Figure 2.11: Immobilization of gold surface via the thiol group.

2.4.4 Estrogen-binding aptamers

Up to date, few aptamers for hormones have been reported; aptamer selected against 17β -Estradiol and progesterone by Contreras-Jimenez *et al.* [70]. The first 17β -Estradiol aptamers (76 mer) was reported by Kim *et al.* using the SELEX process after 7 rounds. Alsager *et al.* found an aptamer that could bind equally to the three steroids; estradiol, testosterone, and progesterone after 18 rounds of SELEX. They demonstrated aptamers with 75 mer for 17β -Estradiol and the aptamer also bound to progesterone [71]. Then, the same aptamer was shortened with 35 mer and 22 mer to demonstrate the binding of 17β -Estradiol. Akki *et al.* reported the third aptamer to bind to 17β -Estradiol. Vanschoenbeek *et al.* reported a series of aptamers to bind to 17β -Estradiol after 10 rounds of SELEX. The various bind with different functional groups on the steroid ring structures [72].

2.5 Conclusion

In this chapter, it described on the studies related on the background theory and the previous work that is relevant to these studies; localized surface plasmon resonance in both refractive index and the surface enhanced infrared absorption (SEIRA) sensing. This also demonstrated the importance of optimise the geometry nanostructures shape, sizes and the surrounding materials as it is sensitive to the changes in refractive index. The overview of the current environmental sensors used to detect the estrogens either the natural or synthetic estrogens and the types of bio-recognition element were also explained in this chapter. The bio-recognition elements are the key components that are immobilized on the biosensor surface and specifically bind to the target analytes. The aptamers are used as a bio-recognition element as it is useful alternatives to antibodies. The studies will provide a new direction for future sensing experiments to produced rapid and accurate monitoring system in the environment.

References

- [1] F. Long, A. Zhu, and H. Shi, “Recent advances in optical biosensors for environmental monitoring and early warning.,” *Sensors*, vol. 13, no. 10, pp. 13 928–13 948, Oct. 2013 (cit. on pp. 6, 24).
- [2] J. Duffus, “Glossary for chemists of terms used in toxicology (IUPAC Recommendations 1993),” *Pure and Applied Chemistry*, vol. 65, no. 9, pp. 2003–2122, Jan. 2007 (cit. on p. 6).
- [3] G. A. Lopez, M. C. Estevez, M. Soler, and L. M. Lechuga, *Recent advances in nanoplasmonic biosensors: Applications and lab-on-a-chip integration*, Jan. 2017. [Online]. Available: <http://www.degruyter.com/view/j/nanoph.2017.6.issue-1/nanoph-2016-0101/nanoph-2016-0101.xml> (cit. on p. 6).
- [4] M. Y. Gross-Sorokin, S. D. Roast, and G. C. Brighty, “Assessment of feminization of male fish in english rivers by the environment agency of England and Wales,” *Environmental Health Perspectives*, vol. 114, no. SUPPL.1, pp. 147–151, Apr. 2006 (cit. on p. 7).
- [5] “UK 2 page Briefing — Flame retardants What is the endocrine system?” Tech. Rep. (cit. on p. 7).
- [6] “Decision 2018/840,” Tech. Rep., 2018 (cit. on p. 7).
- [7] S.-J. Haig, “Charactering the functional through environmental genomics,” PhD thesis, 2014, pp. 1–297 (cit. on p. 8).
- [8] J. L. Zhao, G. G. Ying, L. Wang, J. F. Yang, X. B. Yang, L. H. Yang, and X. Li, “Determination of phenolic endocrine disrupting chemicals and acidic pharmaceuticals in surface water of the Pearl Rivers in South China by gas chromatography-negative chemical ionization-mass spectrometry,” *Science of the Total Environment*, vol. 407, no. 2, pp. 962–974, Jan. 2009 (cit. on p. 8).
- [9] L. Wang, G. G. Ying, J. L. Zhao, S. Liu, B. Yang, L. J. Zhou, R. Tao, and H. C. Su, “Assessing estrogenic activity in surface water and sediment of the Liao River system in northeast China using combined chemical and biological tools,” *Environmental Pollution*, vol. 159, no. 1, pp. 148–156, Jan. 2011 (cit. on p. 8).
- [10] H. M. Kuch and K. Ballschmiter, “Determination of endocrine-disrupting phenolic compounds and estrogens in surface and drinking water by HRGC-(NCI)-MS in the picogram per liter range,” *Environmental Science and Technology*, vol. 35, no. 15, pp. 3201–3206, Jun. 2001 (cit. on p. 8).

- [11] G. G. Ying, R. S. Kookana, and Y. J. Ru, *Occurrence and fate of hormone steroids in the environment*, Dec. 2002. [Online]. Available: <https://www.sciencedirect.com/science/article/pii/S0160412002000752> (cit. on p. 8).
- [12] X. Y. Xiao, D. V. McCalley, and J. McEvoy, “Analysis of estrogens in river water and effluents using solid-phase extraction and gas chromatography-negative chemical ionisation mass spectrometry of the pentafluorobenzoyl derivatives,” *Journal of Chromatography A*, vol. 923, no. 1-2, pp. 195–204, Jul. 2001 (cit. on p. 8).
- [13] D. W. Kolpin, E. T. Furlong, M. T. Meyer, E. M. Thurman, S. D. Zaugg, L. B. Barber, and H. T. Buxton, “Pharmaceuticals, hormones, and other organic wastewater contaminants in U.S. streams, 1999–2000: A national reconnaissance,” *Environmental Science and Technology*, vol. 36, no. 6, pp. 1202–1211, Mar. 2002 (cit. on p. 8).
- [14] S. Zhang, Q. Zhang, S. Darisaw, O. Ehie, and G. Wang, “Simultaneous quantification of polycyclic aromatic hydrocarbons (PAHs), polychlorinated biphenyls (PCBs), and pharmaceuticals and personal care products (PPCPs) in Mississippi river water, in New Orleans, Louisiana, USA,” *Chemosphere*, vol. 66, no. 6, pp. 1057–1069, Jan. 2007 (cit. on p. 8).
- [15] A. Wise, K. O’Brien, and T. Woodruff, “Are Oral Contraceptives a Significant Contributor to the Estrogenicity of Drinking Water? †,” *Environmental Science & Technology*, vol. 45, no. 1, pp. 51–60, Jan. 2011 (cit. on p. 8).
- [16] T. S. Chen, T. C. Chen, K. J. C. Yeh, H. R. Chao, E. T. Liaw, C. Y. Hsieh, K. C. Chen, L. T. Hsieh, and Y. L. Yeh, “High estrogen concentrations in receiving river discharge from a concentrated livestock feedlot,” *Science of the Total Environment*, vol. 408, no. 16, pp. 3223–3230, Jul. 2010 (cit. on p. 8).
- [17] P. Matthiessen, D. Arnold, A. C. Johnson, T. J. Pepper, T. G. Pottinger, and K. G. Pulman, “Contamination of headwater streams in the United Kingdom by oestrogenic hormones from livestock farms,” *Science of the Total Environment*, vol. 367, no. 2-3, pp. 616–630, Aug. 2006 (cit. on p. 8).
- [18] W. J. Langston, G. R. Burt, B. S. Chesman, and C. H. Vane, *Partitioning, bioavailability and effects of oestrogens and xeno-oestrogens in the aquatic environment*, Feb. 2005. [Online]. Available: https://www.cambridge.org/core/product/identifier/S0025315405010787/type/journal%7B%5C_%7Darticle (cit. on p. 8).

- [19] S. R. Hutchins, M. V. White, F. M. Hudson, and D. D. Fine, *Erratum: Analysis of lagoon samples from different concentrated animal feeding operations (CAFOs) for estrogens and estrogen conjugates (Environmental Science and Technology (2007) 41, (738-744))*, Jan. 2007 (cit. on p. 8).
- [20] C. Baronti, R. Curini, G. D'Ascenzo, A. Di Corcia, A. Gentili, and R. Samperi, "Monitoring natural and synthetic estrogens at activated sludge sewage treatment plants and in a receiving river water," *Environmental Science and Technology*, vol. 34, no. 24, pp. 5059–5066, Nov. 2000 (cit. on p. 8).
- [21] T. A. Ternes, M. Stumpf, J. Mueller, K. Haberer, R. D. Wilken, and M. Servos, "Behavior and occurrence of estrogens in municipal sewage treatment plants - I. Investigations in Germany, Canada and Brazil," *Science of the Total Environment*, vol. 225, no. 1-2, pp. 81–90, Jan. 1999 (cit. on p. 8).
- [22] M. Kuster, M. J. López de Alda, M. D. Hernando, M. Petrovic, J. Martín-Alonso, and D. Barceló, "Analysis and occurrence of pharmaceuticals, estrogens, progestogens and polar pesticides in sewage treatment plant effluents, river water and drinking water in the Llobregat river basin (Barcelona, Spain)," *Journal of Hydrology*, vol. 358, no. 1-2, pp. 112–123, Aug. 2008 (cit. on p. 8).
- [23] R. J. Williams, A. C. Johnson, J. J. Smith, and R. Kanda, "Steroid estrogens profiles along river stretches arising from sewage treatment works discharges," *Environmental Science and Technology*, vol. 37, no. 9, pp. 1744–1750, Mar. 2003 (cit. on p. 8).
- [24] H. S. Kushwaha, R. Sao, and R. Vaish, "Label free selective detection of estriol using graphene oxide-based fluorescence sensor," *Journal of Applied Physics*, vol. 116, no. 3, p. 034701, Jul. 2014 (cit. on pp. 9, 10).
- [25] Y. Dai and C. Liu, "Detection of 17 β -Estradiol in Environmental Samples and for Health Care Using a Single-Use, Cost-Effective Biosensor Based on Differential Pulse Voltammetry (DPV)," *Biosensors*, vol. 7, no. 2, p. 15, Mar. 2017 (cit. on pp. 9, 10).
- [26] A. C. Singh, G. Bacher, and S. Bhand, "A label free immunosensor for ultra-sensitive detection of 17 β -Estradiol in water," *Electrochimica Acta*, vol. 232, pp. 30–37, Apr. 2017 (cit. on pp. 9, 10).
- [27] X. Zhang, Y. Peng, J. Bai, B. Ning, S. Sun, X. Hong, Y. Liu, Y. Liu, and Z. Gao, "A novel electrochemical sensor based on electropolymerized molecularly imprinted polymer and gold nanomaterials amplification for estradiol detection," *Sensors and Actuators, B: Chemical*, vol. 200, pp. 69–75, Sep. 2014 (cit. on pp. 9, 10).

- [28] A. Florea, C. Cristea, F. Vocanson, R. Sandulescu, and N. Jaffrezic-Renault, “Electrochemical sensor for the detection of estradiol based on electropolymerized molecularly imprinted polythioaniline film with signal amplification using gold nanoparticles,” *Electrochemistry Communications*, vol. 59, pp. 36–39, Oct. 2015 (cit. on p. 9).
- [29] R. Wang, H. Chon, S. Lee, Z. Cheng, S. H. Hong, Y. H. Yoon, and J. Choo, “Highly Sensitive Detection of Hormone Estradiol E2 Using Surface-Enhanced Raman Scattering Based Immunoassays for the Clinical Diagnosis of Precocious Puberty,” *ACS Applied Materials and Interfaces*, vol. 8, no. 17, pp. 10 665–10 672, 2016 (cit. on p. 10).
- [30] Y. Jia, Y. Peng, J. Bai, X. Zhang, Y. Cui, B. Ning, J. Cui, and Z. Gao, “Magnetic nanoparticle enhanced surface plasmon resonance sensor for estradiol analysis,” *Sensors and Actuators, B: Chemical*, vol. 254, pp. 629–635, Jan. 2018 (cit. on p. 10).
- [31] Y. S. Kim, H. S. Jung, T. Matsuura, H. Y. Lee, T. Kawai, and M. B. Gu, “Electrochemical detection of 17β -estradiol using DNA aptamer immobilized gold electrode chip,” *Biosensors and Bioelectronics*, vol. 22, no. 11, pp. 2525–2531, May 2007. arXiv: [NIHMS150003](#) (cit. on pp. 10, 24).
- [32] P. Englebienne, A. V. Hoonacker, and M. Verhas, “Surface plasmon resonance: principles, methods and applications in biomedical sciences,” *Spectroscopy*, vol. 17, no. 2-3, pp. 255–273, 2012 (cit. on p. 11).
- [33] J. D. Kraus, D. A. Fleisch, and S. H. Russ, *Electromagnetics with applications*, 5th ed. McGraw-Hill, 1999 (cit. on pp. 12, 21).
- [34] S. Tretyakov and C. Simovski, “Historical Notes on Metamaterials,” in *Theory and Phenomena of Metamaterials*, CRC Press, Oct. 2009. DOI: [10.1201/9781420054262.pt1](#) (cit. on p. 13).
- [35] S. E. Mendhe and Y. P. Kosta, “Metamaterial properties and applications,” *International Journal of Information Technology and Knowledge Management*, vol. 4, no. 1, pp. 85–89, 2011 (cit. on p. 13).
- [36] K. M. Mayer and J. H. Hafner, “Localized Surface Plasmon Resonance Sensors,” *Chemical Reviews*, vol. 111, no. 6, pp. 3828–3857, Jun. 2011 (cit. on p. 16).
- [37] L. Novotny and B. Hecht, “Surface plasmons,” in *Principles of Nano-Optics*, Cambridge: Cambridge University Press, 2014, pp. 369–413 (cit. on p. 16).

- [38] E. Wijaya, C. Lenaerts, S. Maricot, J. Hastanin, S. Habraken, J. P. Vilcot, R. Boukherroub, and S. Szunerits, “Surface plasmon resonance-based biosensors: From the development of different SPR structures to novel surface functionalization strategies,” *Current Opinion in Solid State and Materials Science*, vol. 15, no. 5, pp. 208–224, 2011. arXiv: [NIHMS150003](#) (cit. on pp. 16, 19).
- [39] B. H. Stuart, *Infrared Spectroscopy: Fundamentals and Applications*, D. J. Ando, Ed., ser. Analytical Techniques in the Sciences. Chichester, UK: John Wiley & Sons, Ltd, Jun. 2004. DOI: [10.1002/0470011149](#) (cit. on p. 19).
- [40] E. Martinsson, *Nanoplasmonic Sensing using Metal Nanoparticles*, 1624. Linköping University Electronic Press, Nov. 2014, p. 91 (cit. on p. 19).
- [41] I. M. Pryce, Y. A. Kelaita, K. Aydin, and H. a. Atwater, “Compliant metamaterials for resonantly enhanced infrared absorption spectroscopy and refractive index sensing.,” *ACS nano*, vol. 5, no. 10, pp. 8167–74, Oct. 2011 (cit. on pp. 19, 23).
- [42] J. Pendry, A. Holden, D. Robbins, and W. Stewart, “Magnetism from conductors and enhanced nonlinear phenomena,” *IEEE Transactions on Microwave Theory and Techniques*, vol. 47, no. 11, pp. 2075–2084, 1999 (cit. on pp. 20, 21).
- [43] D. Smith, W. Padilla, D. Vier, S. Nemat-Nasser, and S. Schultz, “Composite medium with simultaneously negative permeability and permittivity,” *Physical review letters*, vol. 84, no. 18, pp. 4184–7, May 2000 (cit. on pp. 20, 21).
- [44] B. Lahiri, S. G. Mcmeekin, A. Z. Khokhar, R. M. De La Rue, and N. P. Johnson, “Magnetic response of split ring resonators (SRRs) at visible frequencies.,” EN, *Optics express*, vol. 18, no. 3, pp. 3210–8, Feb. 2010 (cit. on p. 21).
- [45] S. Linden, “Magnetic Response of Metamaterials at 100 Terahertz,” *Science*, vol. 306, no. 5700, pp. 1351–1353, Nov. 2004. arXiv: [science.1105371 \[10.1126\]](#) (cit. on p. 21).
- [46] A. I. Kuznetsov, A. E. Miroschnichenko, Y. H. Fu, J. Zhang, and B. Luk’yanchuk, “Magnetic light,” en, *Scientific reports*, vol. 2, p. 492, Jan. 2012 (cit. on p. 21).
- [47] C. Rockstuhl, T. Zentgraf, H. Guo, N. Liu, C. Etrich, I. Loa, K. Syassen, J. Kuhl, F. Lederer, and H. Giessen, “Resonances of split-ring resonator metamaterials in the near infrared,” *Applied Physics B: Lasers and Optics*, vol. 84, no. 1-2, pp. 219–227, Apr. 2006 (cit. on p. 22).

- [48] T. Endo, K. Kerman, N. Nagatani, Y. Takamura, and E. Tamiya, “Label-free detection of peptide nucleic acid-DNA hybridization using localized surface plasmon resonance based optical biosensor,” *Analytical Chemistry*, vol. 77, no. 21, pp. 6976–6984, Nov. 2005 (cit. on p. 22).
- [49] H. M. Kim, M. Uh, D. H. Jeong, H. Y. Lee, J. H. Park, and S. K. Lee, “Localized surface plasmon resonance biosensor using nanopatterned gold particles on the surface of an optical fiber,” *Sensors and Actuators, B: Chemical*, vol. 280, pp. 183–191, Feb. 2019 (cit. on p. 22).
- [50] T. Chung, S. Y. Lee, E. Y. Song, H. Chun, and B. Lee, “Plasmonic nanostructures for nano-scale bio-sensing,” *Sensors*, vol. 11, no. 11, pp. 10 907–10 929, Nov. 2011 (cit. on p. 22).
- [51] F. Neubrech, C. Huck, K. Weber, A. Pucci, and H. Giessen, “Surface-Enhanced Infrared Spectroscopy Using Resonant Nanoantennas,” *Chemical Reviews*, vol. 117, no. 7, pp. 5110–5145, Apr. 2017 (cit. on p. 22).
- [52] A. John-Herpin, A. Tittl, and H. Altug, “Quantifying the Limits of Detection of Surface-Enhanced Infrared Spectroscopy with Grating Order-Coupled Nanogap Antennas,” *ACS Photonics*, vol. 5, no. 10, pp. 4117–4124, Oct. 2018 (cit. on p. 22).
- [53] T. H. H. Le and T. Tanaka, “Plasmonics–Nanofluidics Hybrid Metamaterial: An Ultrasensitive Platform for Infrared Absorption Spectroscopy and Quantitative Measurement of Molecules,” *ACS Nano*, acsnano.7b02743, Sep. 2017 (cit. on p. 22).
- [54] F. Neubrech, A. Pucci, T. W. Cornelius, S. Karim, A. García-Etxarri, and J. Aizpurua, “Resonant plasmonic and vibrational coupling in a tailored nanoantenna for infrared detection,” *Physical Review Letters*, vol. 101, no. 15, 2008. DOI: [10.1103/PhysRevLett.101.157403](https://doi.org/10.1103/PhysRevLett.101.157403) (cit. on p. 23).
- [55] E. Cubukcu, S. Zhang, Y.-S. Park, G. Bartal, and X. Zhang, “Split ring resonator sensors for infrared detection of single molecular monolayers,” *Applied Physics Letters*, vol. 95, no. 4, p. 43 113, Jul. 2009 (cit. on p. 23).
- [56] C. Wu, A. B. Khanikaev, R. Adato, N. Arju, A. A. Yanik, H. Altug, and G. Shvets, “Fano-resonant asymmetric metamaterials for ultrasensitive spectroscopy and identification of molecular monolayers,” *Nature Materials*, vol. 11, no. 1, pp. 69–75, Nov. 2011 (cit. on p. 23).
- [57] I. G. Mbomson, S. Tabor, B. Lahiri, G. J. Sharp, S. G. McMeekin, R. M. De La Rue, and N. P. Johnson, “Asymmetric split H-shape nanoantennas for molecular sensing,” *Biomedical Optics Express*, vol. 8, no. 1, p. 395, Jan. 2017 (cit. on p. 23).

- [58] G. J. Sharp, H. Vilhena, B. Lahiri, S. G. McMeekin, R. M. De La Rue, and N. P. Johnson, "Mapping the sensitivity of split ring resonators using a localized analyte," *Applied Physics Letters*, vol. 108, no. 25, p. 251105, Jun. 2016 (cit. on p. 23).
- [59] J. Paul, S. G. McMeekin, R. M. De La Rue, and N. P. Johnson, "AFM imaging and plasmonic detection of organic thin-films deposited on nanoantenna arrays," *Sensors and Actuators, A: Physical*, vol. 279, pp. 36–45, Aug. 2018 (cit. on p. 23).
- [60] M. Xi and B. M. Reinhard, "Localized Surface Plasmon Coupling between Mid-IR-Resonant ITO Nanocrystals," *The Journal of Physical Chemistry C*, vol. 122, no. 10, pp. 5698–5704, Mar. 2018 (cit. on p. 23).
- [61] A. E. Cetin, D. Etezadi, B. C. Galarreta, M. P. Busson, Y. Eksioglu, and H. Altug, "Plasmonic Nanohole Arrays on a Robust Hybrid Substrate for Highly Sensitive Label-Free Biosensing," *ACS Photonics*, vol. 2, no. 8, pp. 1167–1174, Aug. 2015 (cit. on p. 23).
- [62] O. Limaj, D. Etezadi, N. J. Wittenberg, D. Rodrigo, D. Yoo, S.-H. Oh, and H. Altug, "Infrared Plasmonic Biosensor for Real-Time and Label-Free Monitoring of Lipid Membranes," *Nano Letters*, vol. 16, no. 2, pp. 1502–1508, Feb. 2016 (cit. on p. 23).
- [63] A. D. Ellington and J. W. Szostak, "In vitro selection of RNA molecules that bind specific ligands," *Nature*, vol. 346, no. 6287, pp. 818–822, Aug. 1990 (cit. on p. 23).
- [64] Sumedha D. Jayasena, "Aptamers: An Emerging Class of Molecules That Rival Antibodies in Diagnostics," *Clinical chemistry*, vol. 45, no. 9, 1999 (cit. on pp. 23, 25).
- [65] A. Ruscito and M. C. DeRosa, "Small-Molecule Binding Aptamers: Selection Strategies, Characterization, and Applications," *Frontiers in Chemistry*, vol. 4, p. 14, May 2016 (cit. on pp. 24, 25).
- [66] J. Zhou and J. Rossi, "Aptamers as targeted therapeutics: current potential and challenges," *Nature Reviews Drug Discovery*, vol. 16, no. 3, pp. 181–202, Mar. 2017 (cit. on p. 24).
- [67] A. V. Lakhin, V. Z. Tarantul, and L. V. Gening, *Aptamers: Problems, solutions and prospects*, 2013. [Online]. Available: <http://aptamer.icmb.utexas.edu> (cit. on p. 24).
- [68] S. Song, L. Wang, J. Li, C. Fan, and J. Zhao, "Aptamer-based biosensors," *TrAC - Trends in Analytical Chemistry*, vol. 27, no. 2, pp. 108–117, Feb. 2008 (cit. on p. 24).

- [69] A. Nezami, R. Nosrati, B. Golichenari, R. Rezaee, G. I. Chatzidakis, A. M. Tsatsakis, and G. Karimi, “Nanomaterial-based aptasensors and bioaffinity sensors for quantitative detection of 17β -estradiol,” *TrAC Trends in Analytical Chemistry*, vol. 94, pp. 95–105, Sep. 2017 (cit. on p. 24).
- [70] G. Contreras Jiménez, S. Eissa, A. Ng, H. Alhadrami, M. Zourob, and M. Siaj, “Aptamer-based label-free impedimetric biosensor for detection of progesterone,” *Analytical Chemistry*, vol. 87, no. 2, pp. 1075–1082, Jan. 2015 (cit. on p. 27).
- [71] O. A. Alsager, S. Kumar, G. R. Willmott, K. P. McNatty, and J. M. Hodgkiss, “Small molecule detection in solution via the size contraction response of aptamer functionalized nanoparticles,” *Biosensors and Bioelectronics*, vol. 57, pp. 262–268, Jul. 2014 (cit. on p. 27).
- [72] K. Vanschoenbeek, J. Vanbrabant, B. Hosseinkhani, V. Vermeeren, and L. Michiels, “Aptamers targeting different functional groups of 17β -estradiol,” *Journal of Steroid Biochemistry and Molecular Biology*, vol. 147, pp. 10–16, Mar. 2015 (cit. on p. 27).

Chapter 3

Methods

3.1 Introduction

This chapter briefly described the numerical, experimental and characterisation techniques that have been used in this research to design the plasmonic nanostructures. An overview of the finite difference time domain and the numerical method that has been used in designing the plasmonic nanostructures prior to the fabrication process is provided. This chapter also described the specific fabrication techniques used in producing the nanostructures and that have been carried out in the James Watt Nanofabrication Centre (JWNC). The measurement techniques and the sample characterisation also will be discussed.

3.2 Simulation Methods

3.2.1 Finite difference time domain

The finite-difference time-domain (FDTD) method is used to solve complicated problems in the electromagnetics both in time and space derivatives in Maxwell's equation. The finite differences were first applied to Maxwell's curl equation by Yee in 1966 [1]. In the FDTD algorithm, the lattice space increment in x, y, and z directions are given by the mesh step sizes of Δx , Δy and Δz and time increment is given by Δt . The three-dimensional FDTD defines an orthogonal cubic with unit cell known as Yee lattice (Figure 3.1). Each cubic grid contains both the electric field (E-field) in time derivative and magnetic fields (H-field) vector (the curl) components. The electric fields component was assigned in the centre of the grid edge and the vector is parallel with each edge, where the magnetic fields were assigned in the centre of the grid face and the vector is perpendicular to each face.

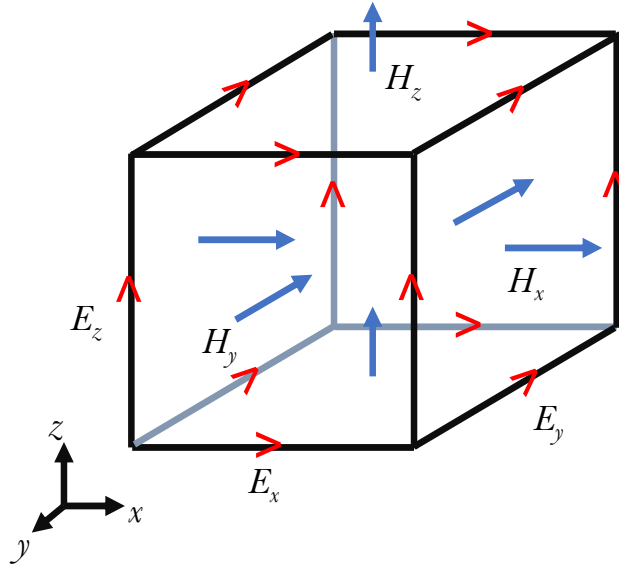


Figure 3.1: Displacement of the electric (E) and magnetic (H) field vector components about a cubic unit cell of the Yee space lattice.

3.2.2 Simulation using Lumerical FDTD solutions

The Finite Difference Time Domain (FDTD) Lumerical simulation software is a 3D FDTD method Maxwell's equations solver for design, analysis and optimization of nanophotonic devices, processes and materials [2]. This software package can be used to investigate the complex geometries in a unit cell and the effect of varying the parameters. Various types of structures (rectangular, circle, ring, and polygon) were included in the software package for the simulation model. It is also used to reduce the cost of experimental fabrication leading to quicker design concepts and specific structures. The FDTD methods are widely used in plasmonic modelling. The setup modules in the simulations include the structures, simulations region using periodic, metal, perfect matched layer (PML), Bloch, symmetric or antisymmetric boundary conditions. The following types of sources are included in the software are the plane wave, dipole, Gaussian and Lorentzian beam source. By running the simulation software, the reflectance and transmittance spectra can be produced by placing monitors into the model. The magnetic and electric field plots can also be viewed [3].

In this work, all simulations were performed using the dielectric values for gold, titanium and silica provided by Palik [4]. The values for zinc selenide and the analytes (organic materials) were not included in the software. The values for zinc selenide and the analytes (organic materials) were not included in the software. Therefore, the refractive index of the materials was defined manually in the material database referring to the datasheets of the materials. The mesh set in the FDTD

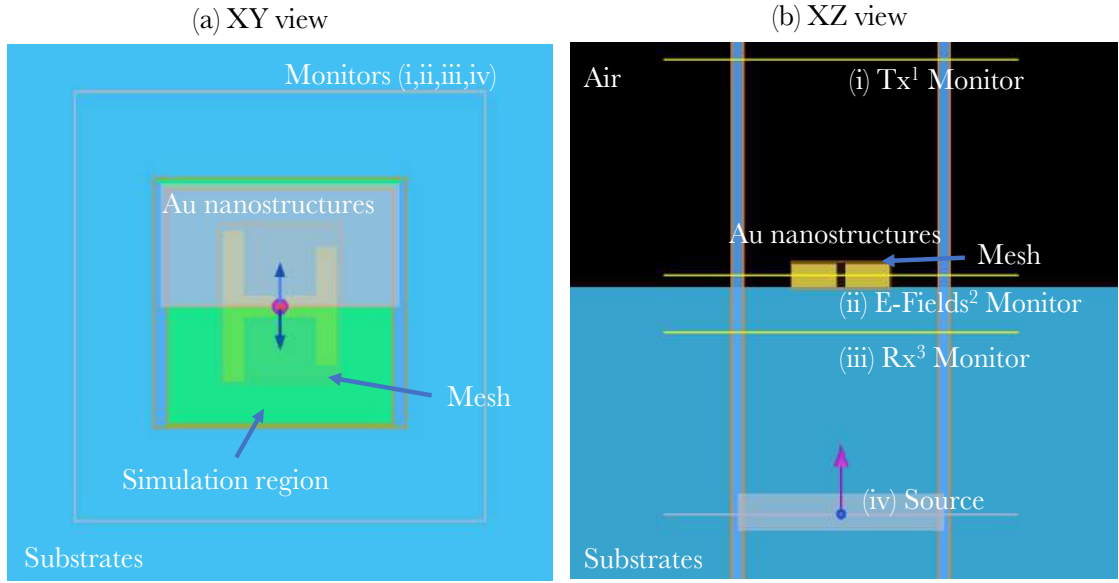


Figure 3.2: The FDTD simulation schematic for setup for modelling the ASH nanostructures (10 nm Titanium (Ti) and 100 nm Gold (Au)) . The images showed the model in XY and XZ plane view. (1)Tx: Transmission, (2)E-Fields: Electric fields, (3) Rx: Reflection.

is divided into finite volume cells that are corresponding to the Yee lattice (Figure 3.1). The finer mesh setting gives an advantage of better accuracy, but it takes a long calculation time and requires more memory. The fabricated device consisted of the period arrays of the nanostructures on the surface of the substrate. In the simulation model, the nanostructure was modelled into a one-unit cell and the structural material was defined as shown in Figure 3.2. The mesh setting was set at 5 nm. Then, in the simulation region menu, mesh accuracy, and the boundary conditions were added into the model. Periodic boundary condition in x and y-axes is the most common setup and was used in the simulation model. Elsewhere, symmetric and antisymmetric boundary conditions were chosen in x and y-axes to reduce the simulation timing since the nanostructures are equal in the y-axis. The perfect matched layer was set in the z-direction to absorb the scattered light. The plane wave source was placed inside the substrate and was used to generate an incident electromagnetic wave and investigate the characteristics over the range of wavelengths of interest. The polarization of the source also can be modified in the setup. The two power monitors; the frequency-domain power monitor and frequency domain filed monitor was used for the simulation model. The 2D frequency-domain power monitor will produce the reflection and transmission results and the monitors were placed on top of the nanostructures and between substrates. The frequency-domain field monitor was able to plot the electric field, magnetic field and the power fields distribution.

3.3 Fabrication Methods

3.3.1 Electron beam lithography

Electron beam (E-Beam) lithography, or EBL, is a lithography process used for advanced research in patterning in the nanometre-scale. Its versatility and high-resolution capabilities are advantageous in nanotechnology research although it is significantly slower than optical lithography. EBL is a serial patterning process on a surface covered with an electron-sensitive film called a resist. Electron beam writing tools consist of an electron gun, beam focusing components, sample stage, vacuum and pumping systems. The electrons are produced from a filament and focused using electromagnetic lenses onto the substrate that sits on a mechanical sample stage. An aperture is used to control the current and the beam shape and size. The electron column is always kept under vacuum to minimize scattering. The e-beam is vector scanned and the beam is deflected to write the pattern that is to be exposed before the sample is repositioned to start the writing the next field [5]. The writing time is time dependent on the pattern data and after writing the field completely, the sample will move to the next write location. The pattern data is derived from computer-aided design (CAD) based software and transmitted electronically, compared to the photolithography in which a static mask is used.

In this work, EBL was carried out by a Vistec VB6 Ultra High-Resolution Extra Wide Field (UHR EWF) tool at 100 kV [6]. The pattern file is designed by using the software Tanner L-Edit IC Layout to produce the GDSII file and the fracturing process is performed using Beamer software. The fracturing process will split the design or fractured into rectangular and trapezoid blocks. Proximity error correction can be performed using Beamer. Beamer produces .vep files and the processes continue with the sample layout file using the software, which is known as Belle before submitting the patterning file to the E-Beam writer. In the Belle file, the substrate size and the exposure parameters such as the exposure dose, beam step size, VRU (variable resolution unit) and the pattern position were well defined. To ensure the resist is fully exposed by the electron beam and maintain an acceptable writing time, the VRU needs to be set so that the beam step size (BSS) meets the following condition: $BSS = \text{Resolution} \times \text{VRU}$. Also, it is important to control the exposure dose (measured in $\mu\text{C}/\text{cm}^2$) as this determines the number of incident electrons on the resist and effects the pattern quality. The e-beam exposure is not only dependent on the exposure dose but also reliant on the electron scattering (both forward and backward). Finally, the Belle file will produce the .bel file to transferred to the VB6 machine for patterning. A conductive substrate is required to allow

the electron to dissipate. On non-conductive substrates (highly insulated), a thin layer of aluminium (Al) is deposited on the substrate as the charge conduction layer.

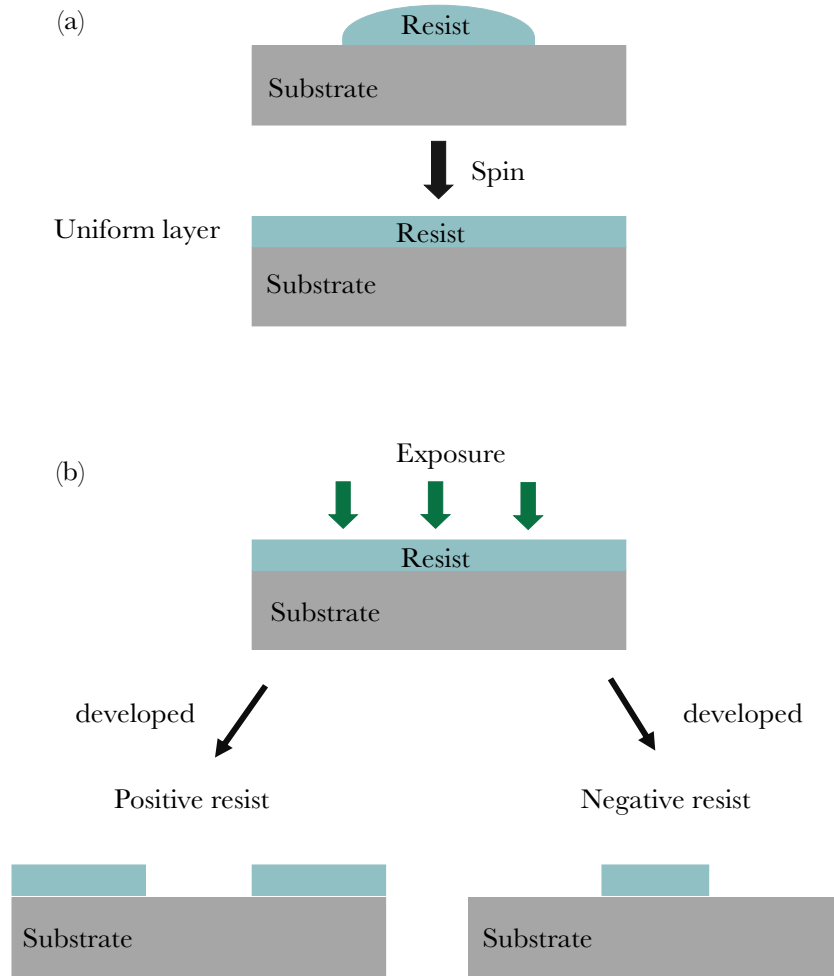


Figure 3.3: (a) The top images show the resist was spun to form a uniform layer. (b) Positive and negative resist behaviour after the development process.

Spinning is the process of applying a uniform thin layer of resist on the substrate in advance of exposure (Figure 3.3). There are two types of electron beam resists; positive and negative tone. Positive resists are where the underlying resist is removed during the development process and negative resists are where the exposed material remains after the development process, as shown in Figure 3.3. Commonly used E-beam resists include the positive polymethylmethacrylate (PMMA) and the negative hydrogen silsesquioxane (HSQ). A bi-layer consists of two films of PMMA each with different molecular weights (PMMA 2010 on top of PMMA 2041 series). This was used in this fabrication process to minimise pinholes and provide improved undercut profiles for the lift-off process. The low molecular weight (PMMA 2010) resist was spun on the bottom layer as it is more sensitive to the electron beam and requires a lower electron dose. This results in a larger feature size being developed and leaves

the top layer of resist overhanging the bottom layer (undercut). By placing the sample on a spinner, few drops of the resist were deposited on the sample with at least 70% coverage. The thickness of the resist depends on the rotation speed and duration as well as the solution type. After the spinning, the samples were baked in the oven or on the hot plate to evaporate the resists. The electron beam exposure breaks the resists into fragments and can be dissolved in the methyl isobutyl ketone or the mixture of isopropanol and the reverse osmosis (RO) water.

3.3.2 Metallisation

Metallisation is the deposition of thin metal layers on the developed resist and can be done using several methods: filament evaporation, electron beam evaporation, laser ablation and sputter coating. The Plassys MEB400S and MEB550S with fully automated control equipment and utilising electron beam evaporation was used for this work for deposition of gold, titanium and aluminium [6]. The source chamber is cryo pumped and separated from the sample chamber by the gate valve. In the vacuum chamber, the electron beam will heat the metal to the point where the metal melts and evaporation occurs. Then, the evaporated metals were transferred to the chamber, to allow the metal to be released on the substrates and the thickness was gradually increased depending on the amount were sets in the system.

3.3.3 Lift-off

After the metal deposition, the remaining resist is dissolved using the pattern transfer process. The pattern transfer technique can be applied using the lift-off process or the etching process. Lift-off process is a pattern transfer process to produces the metal contact on the substrates Figure 3.4. The process was done under the appropriate solvent (acetone) and the sample was immersed in the hot bath for several hours depending on the design leaving only the desired metal patterns.

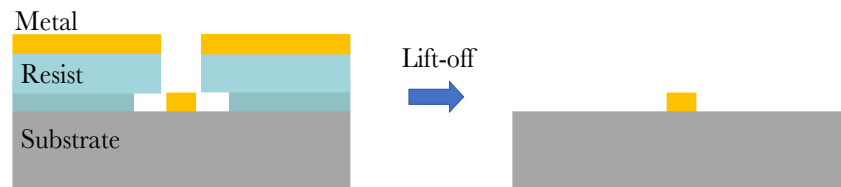


Figure 3.4: Lift-off process

3.4 Measurement Methods

3.4.1 Fourier transform infrared spectroscopy

Fourier Transform Infrared Spectroscopy (FTIR) is an analytical technique used to identify the organic and inorganic material by measuring the intensity of the infrared radiation as a function of frequency or wavelength [7]. In infrared spectroscopy, the infrared radiation will pass through the sample. Some of the radiation will be absorbed by the sample and some of the radiation will be transmitted and reflected. The resulting infrared spectrum can show the molecular bond vibrations. This makes the FTIR useful for several analyses to identify unknown materials, determine the components of the mixture and also determine the quality of the sample. The advantages of using FTIR include the accuracy of the wavenumber, the high resolution and wide scan ranges between 10000 and 10 cm^{-1} . The FTIR can scan up to 50 times in a minute to give a better resolution. The FTIR has improved the signal to noise ratio compared to the other infrared spectroscopy [8].

The basic components in the FTIR spectrometer consist of light sources, an interferometer, the sample holder, detector, amplifier, and a computer. The FTIR Bruker Vertex 70 spectrometer coupled to Nicolet Continuum Hyperion microscope were used in all measurements reported in the following chapter. The FTIR spectrometer uses an interferometer to modulate the wavelength from the broadband infrared sources and is typically based on the Michelson Interferometer experimental setup (Figure 3.5). The broadband mid-IR source was used to excite the sample in the range of 1.25 to 16 μm (8000 – 600 cm^{-1}). The light source illuminated by the visible lights generates the radiation and passes the light into the potassium bromide (KBr) beamsplitter which splits the light into two paths to different mirrors. The calcium fluoride (CaF_2) beamsplitter was used for the near-infrared wavelength in the range of 900 nm to 5000 nm. One beam is transmitted to the stationary mirror which is fixed in place and the other beam is reflected to the movable mirror. The stationary and the movable mirror reflect back the beam to the beam splitter and recombine. The half is passing to the detector and the other half is back to the source. When two beams are interfering to each other, this is resulting in the interferogram that has unique properties of every data point. A liquid nitrogen-cooled mercury-cadmium-telluride (HgCdTe, MCT) detector was used in the measurement detector to measure the interferogram signal which is converted into the spectrum. The liquid nitrogen is used to cool down the detector and keep the device in the operational temperature. All the reflectance and transmittance spectra were measured at normal incidence using the 15 x IR objective lens with 0.4 numerical

aperture (NA). The beam was polarized using a zinc selenide (ZnSe) IR polarizer were placed under the condenser for the transmission measurement. The polarizer was placed in front of the sample at the beam path for the reflection measurement. The samples were placed at the sample holder and positioned in the optical paths to allow the light to pass through the sample. The condenser is used to correct the vertical displacement of the focusing area for the transmittance measurement. The reflection measurement allows the light through on top of the sample and measured the reflected light. The background spectrum is obtained from the planar gold spectrum for the reflection measurement and the substrate materials used for the transmission measurement. The interferometer is maintained under the vacuum and the microscope was constantly purged with nitrogen gas to eliminate water and CO₂ influence. The signal obtained from the detector is an interferogram signal will be analysed with a computer using the Fourier transforms to obtain the infrared spectrum (reflection, transmission, or absorption). The final spectrum is the ratio between the sample spectrum and the background spectrum. The installed OPUS software is used for processing the spectra data. The peak intensity of the FTIR spectra is plotted as the percentage of light transmittance or reflectance at each wavelength (μm) or wavenumber (cm^{-1}).

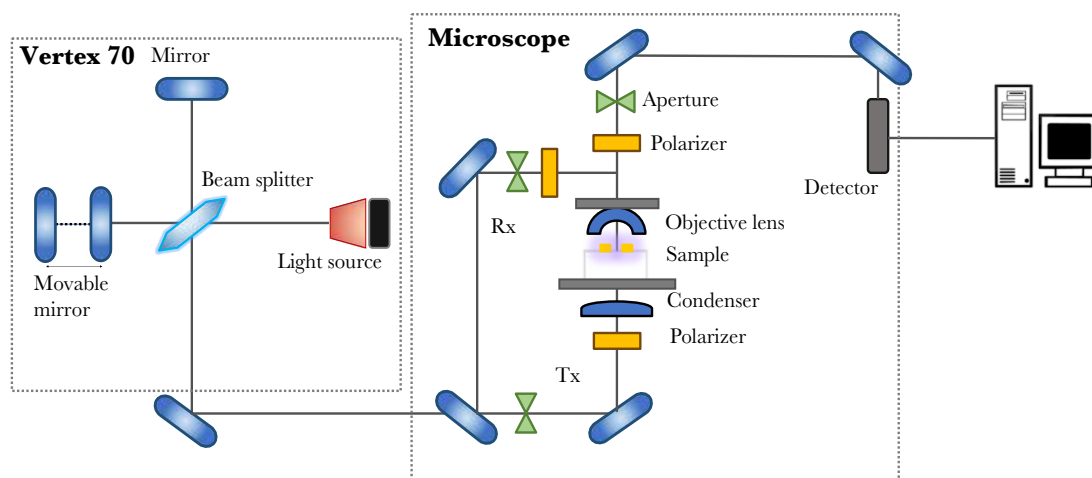


Figure 3.5: Schematic diagram of an optical beam path for the FTIR experimental setup for the reflection and transmission measurement.

3.5 Characterization of the plasmonic nanostructures

3.5.1 Scanning electron microscopy

Scanning electron microscopy (SEM), is one type of microscope that uses high-energy beams of electrons in a raster pattern rather than light. SEM works under vacuum conditions and the electron will interact with the sample to produce secondary electrons. By scanning the beam over the sample its structure can be mapped. SEM has many advantages over other microscopes. The SEM has a large depth of field, which allows more of a specimen to be in focus at one time. The SEM also has a much higher resolution, so closely spaced specimens can be magnified at much higher levels. The SEM shows very detailed 2-dimensional images at much higher magnifications which are more difficult or impossible a light microscope.

In this work, the images of the nanostructures were taken using the Hitachi S4700 SEM tool and the Hitachi SU8240 SEM tool [9]. When using the SEM, the dielectric substrate can cause an issue with charge build up. A thin layer of aluminium or Electra 92 were used as the charge conduction layer on the dielectric substrate to avoid the charge build-up and to have a better and clear image. The substrate was coated up to 20 nm thick of charge conduction layer. The images created without light waves were rendered in black and white.

3.5.2 Atomic force microscopy

Atomic Force Microscopy's (AFM) working principle is to produce topographical images that use force interactions between the probe or tip on the end of the cantilever and the sample surface. A typical AFM consists of a cantilever, a laser, photodiodes and a scanner. The AFM probe with pyramid-shaped probing tips typically micro-fabricated from the silicon or silicon nitride. The probe is attached with a cantilever is interacting with the substrate through the raster scanning motion. As the cantilever approaches the sample surface, the cantilever will make contact and the cantilever is scanned across the surface to generate images in two and three-dimensional images. The resolution and the accuracy of the images are determined by the speed of the scan and the force at the tips. The AFM works in several modes of operations; contact mode, tapping mode, and non-contact mode. These modes are depending to the distance between the sample surface and the tip [10]

In this work, the Bruker Dimension Icon AFM using the ScanAsyst mode based on the peak force tapping mode which collects force curves at every pixel in the image. The probe is periodically tapping on the samples and the interaction force is measured by the deflection of the cantilever. PeakForce tapping provides much more accuracy than the tapping mode. The AFM images analysis using the software provided by the Bruker (NanoScope analysis software) has been used for characterising the surface roughness or surface modification on the nanostructures, the morphology and the height profile.

3.5.3 Optical microscopy

Optical microscope is commonly using visible light and a system that allows magnifying the images of the small objects. It generates a micrograph image using the standard light-sensitive cameras. The power of magnification of the optical microscope depends on the objective lenses from 5 times magnification to 150 magnification. The condenser is used to focus the lights on the sample through the opening in the stage. The optical microscopy has been used in this work in order to inspect the sample during the fabrication process and also the deposition of the analytes on the sample.

3.6 Conclusion

In this chapter, the relevant modelling and specific fabrication process of making the plasmonic nanostructures have been described in details. In addition, the simulation techniques and the sample characterisation were explained, and the specific details of these can be found in the experimental details (Chapter 4, 5, and 6).

References

- [1] Kane Yee, “Numerical solution of initial boundary value problems involving maxwell’s equations in isotropic media,” *IEEE Transactions on Antennas and Propagation*, vol. 14, no. 3, pp. 302–307, May 1966 (cit. on p. 36).
- [2] *Lumerical Soutions*, 2015. [Online]. Available: <https://www.lumerical.com/tcad-products/fdtd/> (cit. on p. 37).
- [3] F. Capolino, *Theory and Phenomena of Metamaterials*. CRC Press, Oct. 2009, vol. 8, p. 974 (cit. on p. 37).
- [4] E. D. Palik, *Palik, Handbook of Optical Constants of Solids, Vol.2*. 1991, vol. 2 (cit. on p. 37).
- [5] R. F. Pease, “Electron beam lithography,” *Contemporary Physics*, vol. 22, no. 3, pp. 265–290, May 1981 (cit. on p. 39).
- [6] JWNC, *James Watt Nanofabrication Centre*, 2011. [Online]. Available: <http://jwnc.eng.gla.ac.uk/> (visited on 07/15/2019) (cit. on pp. 39, 41).
- [7] A. Dutta, “Fourier Transform Infrared Spectroscopy,” in *Spectroscopic Methods for Nanomaterials Characterization*, vol. 2, Elsevier, 2017, pp. 73–93. arXiv: [arXiv:1011.1669v3](https://arxiv.org/abs/1011.1669v3) (cit. on p. 42).
- [8] B. H. Stuart, *Infrared Spectroscopy: Fundamentals and Applications*, D. J. Ando, Ed., ser. Analytical Techniques in the Sciences. Chichester, UK: John Wiley & Sons, Ltd, Jun. 2004. DOI: [10.1002/0470011149](https://doi.org/10.1002/0470011149) (cit. on p. 42).
- [9] Hitachi, *Hitachi High-Technologies Introduces the Ultimate Field Emission Scanning Electron Microscope: The SU8200 Series : Hitachi High-Technologies GLOBAL*. [Online]. Available: <https://www.hitachi-hightech.com/global/about/news/2013/nr20130516.html> (visited on 07/15/2019) (cit. on p. 44).
- [10] S. B. Kaemmar and Bruker Corporation, *Introduction to Brukers ScanAsyst and PeakForce Tapping AFM Technology*, 2011. (visited on 07/03/2019) (cit. on p. 44).

Chapter 4

Selection of asymmetric nanostructures and substrates for environmental sensors

4.1 Abstract

An asymmetric split-H resonator (ASH) has been designed using gold on a fused silica and zinc selenide substrate. The aim is to obtain a maximum - quality factor at the reflectance resonance peaks in the mid - infrared wavelength of 2 μm to 8 μm . The structures were modelled using the Finite Difference Time Domain (FDTD) Lumerical Solution simulation software by adjusting the parameter of periodic boundary condition on the x and y-axis and perfectly matched layer (PML) on the z-axis. The asymmetric structures give double resonance peaks that depend on the arm-length of the structure. The electric-field of the incident wave has been both polarized parallel to the vertical asymmetric dipole arms and polarized across the gap in the horizontal bar. The periodic arrangement along the x and y-axes was varied to tune the width of the resonant peaks in order to obtain the better sensitivity. Experimental results broadly confirm the simulations.

4.2 Introduction

Metamaterials are man-made or artificial structures that have geometries smaller than the wavelength of light. These structures have unique properties that can allow effective negative permeability and permittivity, among other properties, that are not found in nature due to their design and arrangement [1]–[3]. The properties of materials are engineered by the structures in periodic arrays rather than changing the chemical deposition. The geometry can be altered to produce a desired electro-

magnetic response for the targeted application depending on the shape, structure size and periodic arrangement. The structures shapes' have been engineered from nanoparticles, nanorods, circular, crescents, prism and bowties to achieve higher electric field enhancement or to the refractive index change [4]–[7]. Furthermore, light interaction with an array of metamaterial structures resulting in localized surface plasmons can give a complex resonant phenomenon, such as Fano resonances or plasmon resonance hybridization. This is useful because Fano resonances can be engineered with the specific coupling parameters to produced narrow line width and sensitive to refractive index change [8], [9].

Metamaterials have been actively researched in many regions of the electromagnetic spectrum from the microwave through to the terahertz, infrared and visible ranges and some have demonstrated novel properties such as invisible cloaking devices, superlensing and negative refraction [10]. The applications of metamaterials includes imaging, communication and biochemical sensors. The metal nanostructures are typically arranged in 2D-arrays using either gold, silver or copper deposited on a dielectric or semiconductor substrate to generate strong plasmonic resonances depending on the specific application.

Verellen *et al.* (2011) demonstrated that high sensitivity localized surface plasmon resonances (LSPR) refractive index sensing in the near infrared [11]. The “XI” structures (Figure 4.1(a)) introduced consisted of combinations of nanocross and dipole structures, of which the modes of structures coupled into three hybridized modes. Two resonances were obtained from the quadrupole nanocross and a single resonance peak was viewed from the dipole. The structure’s geometry has been tuned to understand the coupling effect between the dipole and nanocross. Additional substrate etching in the design resulted in a large enhancement of the sensing volume and also increased the sensitivity. The smaller gaps in between the structures help to narrow the linewidths of the nanocross and dipole resonance with the quality factors (Q-factors) of 8 and 7 respectively. A microfluidic chip was used to transport glycerol solutions as analytes with varying values of refractive index. The results showed the spectra was red-shifted with a high sensitivity of 1000 nm/RIU and FOM of 5.

In 2012, Liu *et al.* studied plasmonic heptamer clusters (Figure 4.1(b)) to produce multiple Fano resonances with strong modulation depths [12]. The heptamer clusters are a combination of seven split nanorings (SNR) with two gaps. The structures were simulated using FDTD simulation software with gold on top of surrounding medium with a refractive index of 1.33. Multiple resonances have been

achieved from 800 nm to 1600 nm wavelength. However, the studies were performed in simulation by producing the multiple resonances by varying the outer radius (R), separation (S) and gaps (G), with different incident light polarization. By increasing the separation of the structures, the resonances became broader due to the weaker interaction between the nanorings.

Recently, the studies on producing multiple peak resonances in single structures were investigated to increase the functionality and performance of biosensors. A combination of two different sizes of an asymmetric double bar (ADB) (Figure 4.1(c)) structure was proposed by Moritake *et al.* (2016) [13]. The design consists of large and small ADBs on silica substrates with two asymmetric gold bars of different lengths. A triple Fano resonance was achieved when combining the two ADBs in near infrared region with larger Q-factors compared to the single Fano resonance. The calculations of Q-factors were performed by fitting Lorentzian functions. Chen *et al.* (2016) [14] also demonstrated that by pairing two sizes of split ring resonator (SRR) (Figure 4.1(d)); inner SRRs (SRR_i) and outer SRRs (SRR_o), two extremely sharp transmission peak existed at 7.4 μm and 2.8 μm . The refractive index sensitivity was calculated by increasing the thickness of the dielectric layer with a fixed refractive index of 2.4 at the surfaces of coupled SRR. The Drude model was used to describe the plasma frequency was $1.37 \times 10^{16} \text{ s}^{-1}$ of the dielectric layer. By gradually increasing the thickness of dielectric layer, the resonance is shifted, and the sensitivity is evaluated to be 1230 nm/RIU and 220 nm/RIU respectively and the FOM of 2.5 and 2.4.

Comparing to other nanorods or dipole structures, Yang *et al.* (2018) [15] have designed an asymmetric nanostructure (Figure 4.1(e)) in the longitudinal direction to produce a resonance at the visible to near infrared range and to be optimized to have highest field enhancement. The studies show the comparison between single nanorod and asymmetric nanorods, where the rods diameter and the gaps between two adjacent rods is equal to 10 nm. The combination of the three asymmetric nanostructures with different lengths produced a sharp Fano resonance with high quality factors of 16 with the enhancement factor equal to 24. The χ -shaped nanostructures (Figure 4.1(f)) by Kim *et al.* were presented in this paper also show that Fano resonance can be obtained by two structures; dipole and hexapole nanorods are coupling due to the narrow gaps between the dipoles [16].

In this chapter, metal metamaterials nanostructures will be used to generate plasmonic resonances at the targeted wavelength in the infrared region where structure sizes are in the nano or micro scale. The target is to achieve narrow resonance,

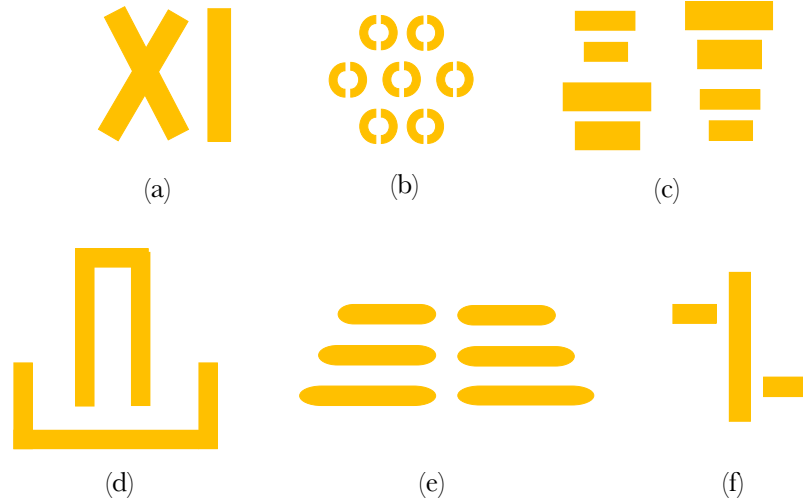


Figure 4.1: The various nanostructures shaped (a) XI structures, (b) seven split nanoring (SNR) (c) asymmetric double bar (ADB), (d) Split ring resonator (SRR), (e) asymmetric nanostructure (f) χ -shaped nanostructures.

optimum sensitivity and figure of merit (FOM) for sensors derived from nanostructure. Moreover, the simulated numerical results showed the necessary step is optimizing the sharpness of the resonances (Q-factors), by investigating their metal compositions, geometry, periodicity arrangement and also the effect of two different substrates. An asymmetric nanostructure has been designed using gold on dielectric substrate to give double resonance peaks with a trapped mode that depends on the arm-lengths and can be tuned to the targeted wavelength. The trapped mode is present between two resonance peaks and is also known as the Fano resonance, or dark mode.

4.3 Asymmetric plasmonic nanostructures

Asymmetric split ring resonators (ASRR) have been introduced because they can produce high Q-factors resonances due to the presence of a so-called trapped mode. The additional capacitive and inductance element in the structures produces two resonance peaks compared to single gap SRR. The trapped mode is the dip that appears between two resonance peaks from the asymmetric structures. Fedotov *et al.* reported in 2011 a narrow transmission and reflection resonance with high Q-factors of 20 using ASRRs at microwave frequencies [17]. This was achieved by the trapped mode coupling weakly to the free space and the symmetry breaking in the structure to produce a narrow transmission resonance in between two reflection resonance peaks. The longer-armed SRR (L_1) structure produced a resonance peak at the longer wavelength and the shorter SRR (L_2) produced a resonance peak at the shorter wavelength, in agreement with the LC resonance description. The ASRR

in Figure 4.2(a) was designed by Lahiri *et al.* (2009) has a circular basic geometry with gaps in between two different sizes of the arc length, (left hand and right hand). The two arcs act as two separate resonators that produce their individual resonance responses depending on their dimensions [18]. The results are similar to those of Fedotov *et al.* [17], including the presence of trapped mode between the two resonance peaks. The Q-factors for ASRR are reduced to 7 in the mid-IR wavelength compared to 20 in the microwave range. Chae *et al.* (2015) [19] make a comparison between four different shapes of the structures; ASRR, crescent-shaped (Cr-SRR), “C”-shaped (CSR) and “U”-shaped (USRR) in different pitches and period arrangement, either isolated or organized to show the SEIRA enhancement and spectra in the near field. The dimension of the structures is around $1.10\ \mu\text{m}$ to $1.85\ \mu\text{m}$ and produces the reflectance resonance between $8\ \mu\text{m}$ and $9.0\ \mu\text{m}$. The measurement was taken using photothermal induced resonance (PTIR) and showed that the enhancement is strongly dependent on the shapes of the structures.



Figure 4.2: Illustration of Asymmetric Split Ring Resonators (ASRR) with different size of arc-length and (b) Asymmetric split H-shape (ASH).

In a proceedings paper, Mbomson *et al.* (2015) [20] introduced nanostructures named asymmetric split H-shape (ASHs) resonators, as shown in Figure 4.2(b) which produced double plasmonic resonance and narrow resonance peaks in mid-IR compared with asymmetrical dipole structures alone. The ASH shows a narrower resonance peak because of the split crossbar between two asymmetric arms giving stronger coupling between the dipoles. Due to the narrow resonance, it helps to increase the value of Q-factors [20]. A further reason for using this structure is to produce multiple resonances instead of a single resonance by designing the ASH structure double asymmetric with different characteristics dependent on either vertical or horizontal polarization. Figure 4.3 shows the comparison between two-resonance peaks position using ASH and ASRR with the same periodic size arrangement. The resonances of the ASH with Q-factors of 14 compared to ASRRs with Q-factors of 6 [20].

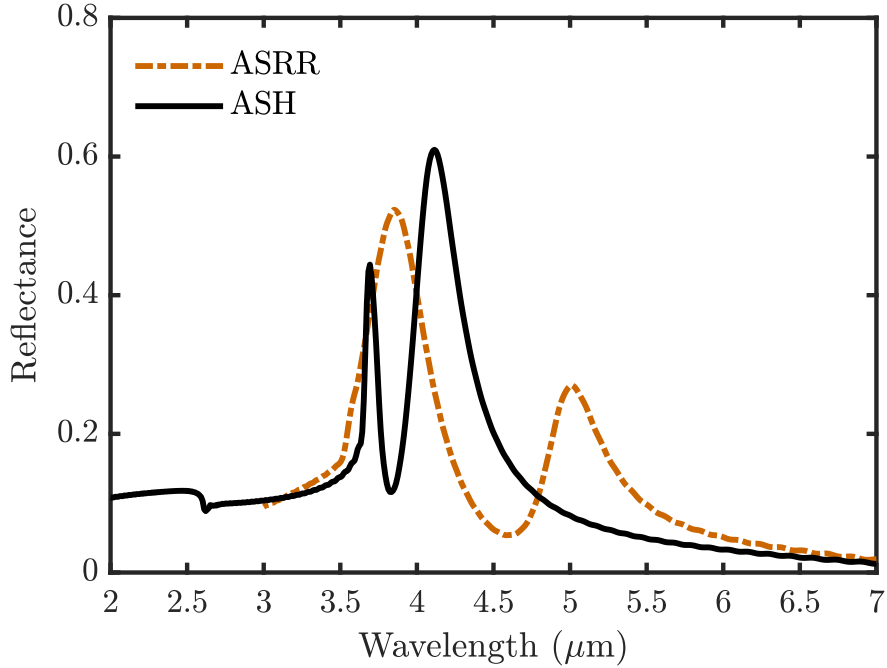


Figure 4.3: The simulation results of the reflectance resonance peak between ASRR and ASH with $2.40 \mu\text{m}$ periodic boundary size. The geometry sizes of ASH are $L_1 = 1.3 \mu\text{m}$ and $L_2 = 1.1 \mu\text{m}$ and the diameter of ASRR is $1.2 \mu\text{m}$. Both of the structures produce the resonances between wavelengths of $3.5 \mu\text{m}$ to $5.5 \mu\text{m}$.

4.3.1 Quality factor in Mid Infrared

In most of the results in the visible and IR spectral ranges, the Q-factors of ASR structures can be as high as 6 compared to the other ranges [17]. This is because of the losses in metal and the influence of the substrate. The Q-factor can be defined as the ratio of the resonance frequency (f_0) and the full width at half maximum (FWHM) (Δf) of the resonance peak [21]. When the structures are less asymmetric, the Q-factors of transmission resonance of trapped mode increases and reflectance resonance of the ASRR also increases. The challenge is to improve on the Q-factors of other metamaterial structures (Table 4.1) and improve on the sensitivity and figure of merit as explained in the previous chapter. The improvement of Q-factors can also be observed by the coupling of structures in both x and y-axes. The reflectance of the resonance increases when the periodic arrangement is decreased and the FWHM of the resonance increases [22].

Table 4.1: Comparison of the Q-factors in the infrared wavelengths.

No	Structure/Shape	Wavelength (μm)	Q-Factors	References
1	CSRR	9	5.7	[19]
2	USRR	1.50-5.50	3.6	[23]
3	Back to back USRR	4.70-7.30	4.5	[24]
4	Tailing symmetry of USRR	1.60-2.10	4	[25]
5	ASRR	3.00-7.00	6	[19]
6	ASH	3.00-7.00	23	[20]

4.4 Modelling and simulation on the silica substrate

4.4.1 Modelling the asymmetrical structure

The ASH nanostructure was formed with dipole strips in both vertical and horizontal orientations with a width (w) and thickness (t) of 100 nm. The symmetric dipole in the horizontal direction can be tuned to an asymmetrical dipole to produce reflectance resonances with different characteristics. The geometry of the ASH one-unit cell is demonstrated in Figure 4.4. The arrays of ASH were arranged on fused silica (SiO_2) substrate and the geometric parameters of the arm-lengths were $L_1 = 1.6 \mu\text{m}$ and $L_2 = 1.2 \mu\text{m}$. The constant gap (g) is 50 nm in between the horizontal dipole (H) of 350 nm. SiO_2 was used as a substrate because of its transparency in the visible and infrared wavelength and lower losses with a refractive index of 1.4 [18]. The gold was used as the metal because of its low losses compared to Al and it is negative permittivity at the shorter wavelength. It also has good resistance to oxidative corrosion when in contact with organic materials.

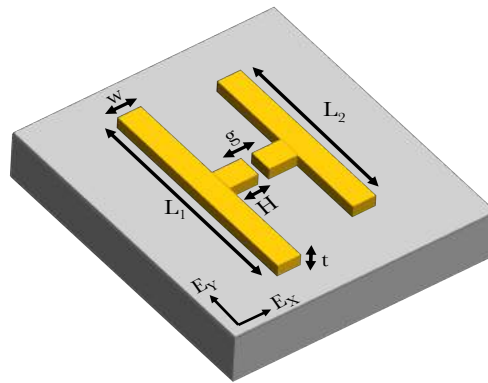


Figure 4.4: Schematic diagrams of Asymmetric H-Shaped (ASH) resonators for FDTD simulation in one-unit cells including the geometrical parameters, arm lengths (L_1 and L_2), horizontal dipole (H) width (w), gap (g) and thickness (t). The incident light polarization, E_Y and E_X are shown in the figure.

4.4.2 Simulations using FDTD Lumerical software

The sample was designed with gold on top of the fused silica substrate using material data from Palik [26]. The simulations used periodic boundary conditions along the x and y-axes with equal periodicity to simulate an infinite array in both directions. Antisymmetric and symmetric boundary conditions were used in the x and y-direction to reduce the simulation time. A perfectly match layer (PML) was used for the z-axis with the wavelength range from 2 μm to 8 μm . The incident wave has been polarized across the x-axis and along the y-axis. The materials were excited by a plane wave propagating along the z-direction with the electric fields in both polarizations. A transmission monitor was placed in between the substrates and the nanostructures and the reflection monitor was placed above the gold nanostructures.

Three different split-H nanostructures; Symmetric split-H resonators (SSH), Asymmetric split-H resonators (ASH) and Double asymmetric split-H resonators (D-ASH) were modelled for comparison with a constant gap. Figure 4.5 shows the transmittance and reflectance spectra in both polarizations; E_X polarization is when the electric field is across the gap and E_Y polarization is with the electric field parallel to the vertical dipole. SSH is composed of all the arm lengths are designed in symmetric structures both in the vertical (identical arm length) when L_1 and L_2 are 1.6 μm and the horizontal dipole, H , is 0.35 μm ; the single resonance peak appears in both polarizations at a wavelength of 4.40 μm . This due to symmetric arm length producing a single resonance peak. Then, the nanostructures modelled were continued by changing the sizes of vertical arm length known as ASH; shortening the arm length L_2 and the arm length L_1 and with H remaining constant. By adjusting the arm length sizes to introduce asymmetry in the structures, two separate resonance peaks appear at 3.8 μm and 4.8 μm under E_Y polarization. Between the two resonances, the reflection trough at 4.40 μm can also be identified as a trapped mode or fano resonance. Lastly, the structures were designed with both arms lengths' vertically and horizontally asymmetric (D-ASH) and the results showed double resonance peaks in both polarizations. Asymmetric horizontal dipole sizes are, H_1 is 0.8 μm and H_2 is 0.7 μm . The measurements show that under E_X polarization double resonances are exhibited at wavelengths of 3.8 μm and 5.00 μm and under E_Y polarization the resonance exhibits the same wavelength as ASH. Changing the arm length for the structure not only produces two resonance peaks but also tunes the position of the resonance peaks [27].

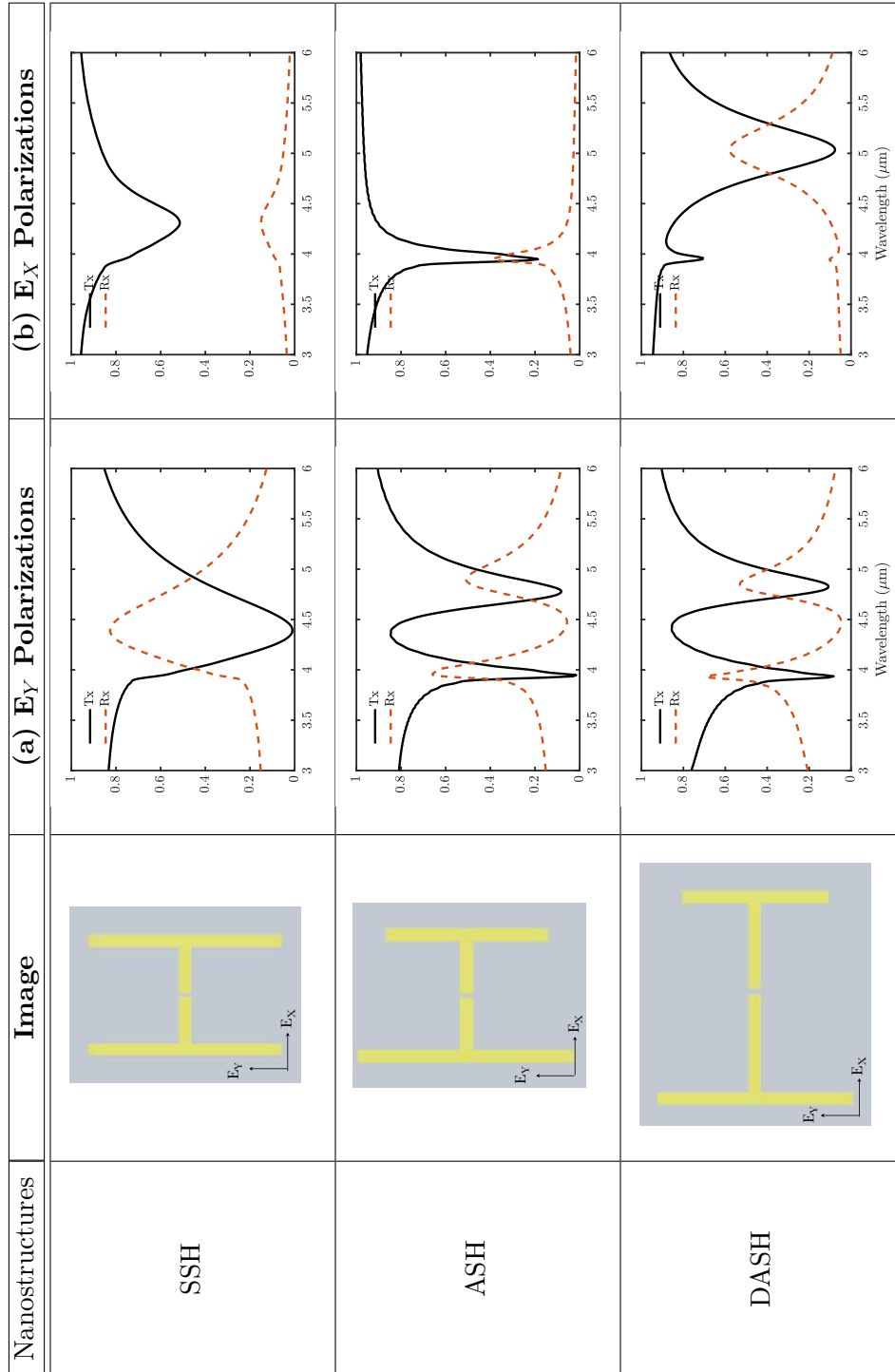


Figure 4.5: Varying the ASH and SSH geometries structure. Transmittance and reflectance spectra at 2.8 μm periodicity in both polarizations; (a) polarization parallel with vertical dipoles (b) polarization perpendicular with horizontal dipoles.

An additional simulation was performed to understand the coupling effect of the ASH with separate arm-lengths as shown in Figure 4.6. Individual arm-length of ASH produce a single resonance that is similar to the resonance hybridization model that has been explored by Giessen *et al.* [28], [29] and explained in other references [30]–[32]. The plasmonic modes of the arm length, L_1 (Figure 4.6(a)) and L_2 (Figure 4.6(b)) are excited at a frequency, ω_1 and ω_2 , when resonance exhibits at the wavelength of $4.8 \mu\text{m}$ (green dashed line) and $4.00 \mu\text{m}$ (orange dotted line). This corresponds to the plasmonic eigenmodes $|\omega_1\rangle$ and $|\omega_2\rangle$. The interaction between these two modes results in a new coupled mode of the plasmonic eigenmodes; $|\omega_+\rangle$ corresponding to symmetric plasmonic mode (high energy mode) and $|\omega_-\rangle$ corresponding to asymmetric plasmonic mode (low energy mode). The reflection dip at a wavelength of $4.4 \mu\text{m}$ in the resonance is due to resonance hybridization between two arms of the ASHs that are positioned close to each other and produce two resonances at a wavelength of $3.8 \mu\text{m}$ and $4.8 \mu\text{m}$ (black line).

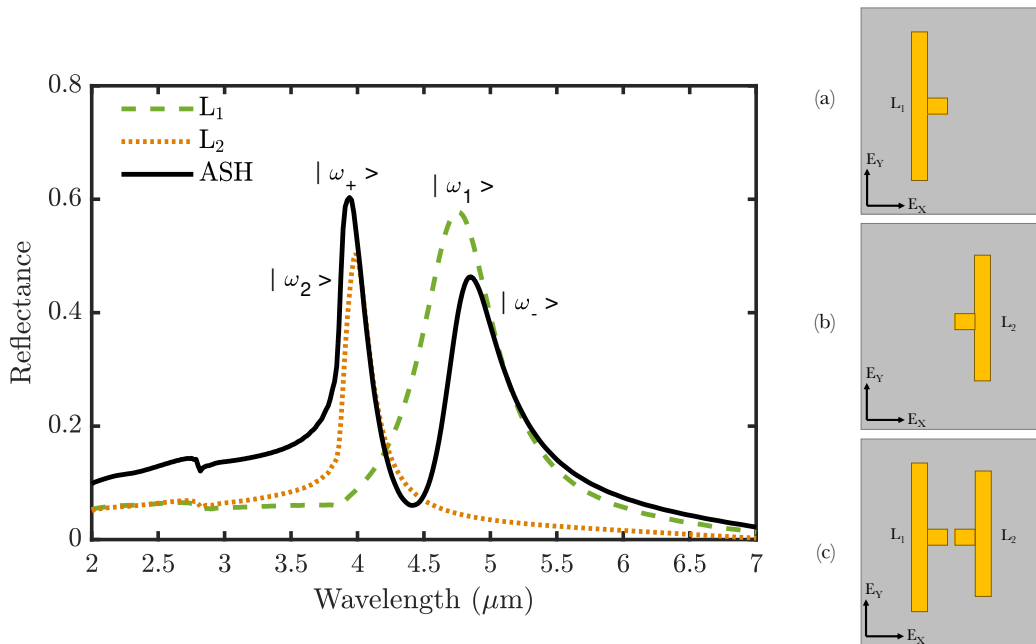


Figure 4.6: Schematic and simulation results of the geometries for ASH and side to side. Illustration of nanostructures with (a) the arm-length, L_1 of ASH produced a resonant with green dashed line, (b) the arm-length, L_2 of ASH with resultants in orange dotted line and (c) ASH with a black line.

Another illustration of the plasmon hybridization is shown in the energy band diagram in Figure 4.7. The resonance is slightly red-shifted, and this is due to the contact between both arm-length, L_1 and L_2 that correspond to symmetric and asymmetric resonances $|\omega_+\rangle$ and $|\omega_-\rangle$. The resonance is redshifted due to a reducing energy level (increasing wavelength). It is observed the resonance $|\omega_1\rangle$ (green dashed line) amplitude is much higher than the amplitude of $|\omega_2\rangle$ (orange dotted line) as demonstrated in Figure 4.6. After the resonance hybridization, the amplitude of symmetric resonance $|\omega_+\rangle$ is much higher than the amplitude of asymmetric resonance $|\omega_-\rangle$. Also, the resonance linewidth of asymmetric resonance $|\omega_-\rangle$ is narrower than the linewidth of resonance $|\omega_1\rangle$. At the asymmetric modes, the electron current is attracted to each other, resulting in a decrease in oscillation amplitude and a narrower linewidth.

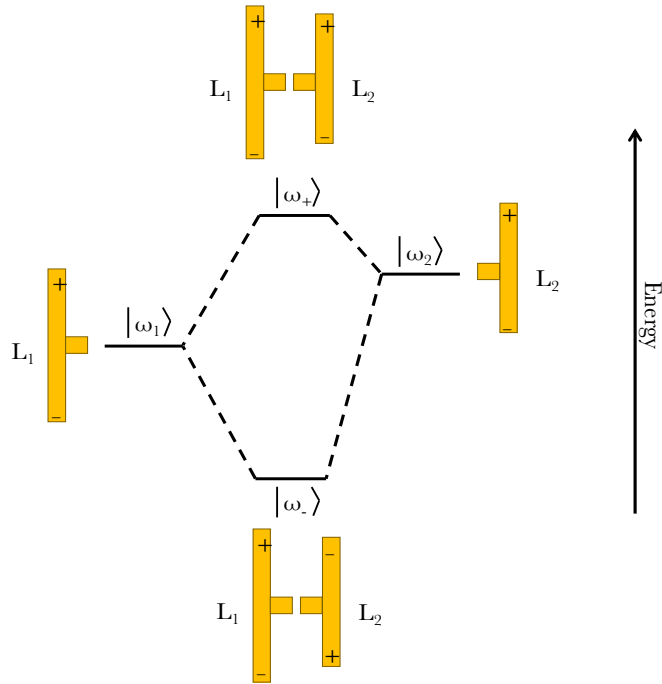


Figure 4.7: An energy level diagram describing the plasmon hybridization of ASH. The coupling effect between both arm-length, L_1 and L_2 produce two new modes, symmetric and antisymmetric.

4.5 Fabrication and measurement

4.5.1 Fabrication on fused silica

The fused silica substrate was purchased from UQG Optics with 50 mm x 50 mm square with a thickness of 500 μm . Using a scribe and diamond pen, the sample sizes were cleaved into small pieces with sizes 15 mm x 15 mm square. Below are the steps of the fabrication method were followed based on the references [21], [32], [33]:

1. The sample is cleaned using acetone in an ultrasonic bath for 3 min followed by methanol and Isopropyl-Alcohol (IPA). Blow-dry the sample using a nitrogen gun after rinsing.
2. The sample was then spin-coated with a bi-layer of polymethyl methacrylate (PMMA) resists. The first layer spin with 8% 2010 PMMA at 5000 rpm for 60 sec and baked for 30 min in a 180°C oven giving thickness 150 nm. The second layer, 4% 2041 PMMA at 5000 rpm for 60 sec to give an additional thickness of 100 nm. The sample was then baked again overnight in a 180°C oven.
3. 20 nm of Aluminium (Al) as a charge dissipation layer is deposited on top of the resists layer using the Plassys evaporator before the patterning.
4. The sample is patterned using electron beam lithography (EBL) with 1 nm resolution, with a beam spot sizes of 4 nm and the VRU is set at 5. The dose is varied from 500 to 1000 depending on the feature sizes.
5. Before the developing process, the Al conduction layer is removed using MF-CD26 for 60 sec depending on the thickness until the sample is clear.
6. Then, the sample is developed using developer conditions with 2.5:1 solution of methyl isobutyl ketone (MIBK) and IPA for 30 sec at the temperature of 23°C. Rinse off with IPA for 1 minute and blow dry.
7. The patterns are deposited with 10 nm adhesion layers of titanium (Ti) and followed by 100 nm thickness of gold (Au) on top of the layered resists.
8. Finally, the sample was immersed in acetone at 50°C for two hours to lift-off additional metal. The sample was then rinsed with IPA and blow dried using nitrogen.

After completing the fabrication process, the sample was inspected using SEM. Since the substrate is a non-conducting material it was coated on top with a 10 to 20 nm Al to reduce the charging effect during the imaging and was removed after completion. The entire steps of fabrication are illustrated in Figure 4.8.

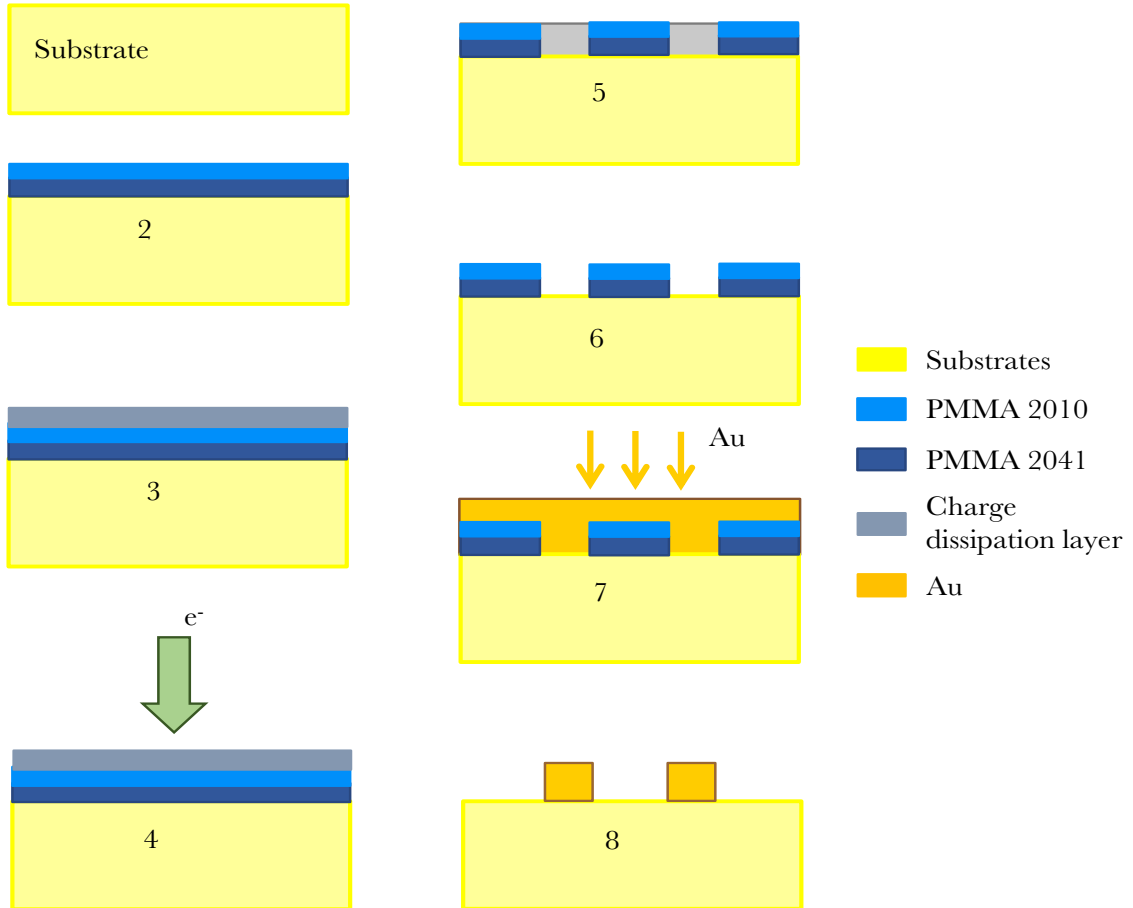


Figure 4.8: Illustration of the fabrication process steps on fused silica or ZnSe substrates as explained in the Section 4.5.

4.5.2 Fabrication on ZnSe substrate

The ASH nanostructures were also fabricated on the ZnSe substrates with a thickness of 1 mm, 12 mm × 12 mm purchased from Crystran Ltd [34]. The fabrication process was almost the same as the fused silica substrate (Figure 4.8). The ZnSe substrate was cleaned using acetone and IPA for 30 sec in the ultrasonic bath without methanol due to the adverse reaction on the substrate. The samples were spun with a bilayer of PMMA resists 4% 2010 with speed 2000 rpm for 60 sec, and PMMA resists 4% 2041 with 5000 rpm for 60 sec to give a thickness of 200 nm. The sample was baked at 180°C in an oven and left for 30 min for the first layer then 120 min for the second resist layer. EBL was used for patterning. Oxygen plasma was used

to remove residues of the resists on the surface before the metalisation and after the lift-off process. After patterning the sample was developed under the mixtures of IPA to reverse osmosis (RO) water (7:3) for 30 sec. Finally, the sample was rinsed with RO water.

4.6 Results and discussions

4.6.1 Effect the period arrangement of ASH

The periodic arrangement (P) along the x and y-axis was varied to tune the width of the resonance peak in order to obtain the highest possible quality factor. In other work, the period size is double the arm-length, $L_1 = 3.2 \mu\text{m}$ but the periodic arrangement of the structures used in this work were varied from $2.0 \mu\text{m}$ up to $3.2 \mu\text{m}$ as shown in Figure 4.9 [20]. Furthermore, by changing the periodicity it will influence the light-matter interactions and coupling effects between the nanostructures. The periodic arrangement and different design of metamaterials can improve the Q-factor and strength of the resonance peak [35]. It is important to achieve a sharp resonance peak with high Q to increase the figure of merit of the structures to refractive index change [22]. The periodic arrangement of ASH was tuned and varied to produce sharpening of the resonances. Figure 4.10 shows, the comparison of reflection spectra of measurement and simulation in both polarizations. Considering the first E_Y excitation in vertical (parallel to the asymmetric arms), the two-resonance peaks respond at wavelengths of $\sim 3.6 \mu\text{m}$ and $\sim 4.9 \mu\text{m}$ and the reflection dip at $\sim 4.5 \mu\text{m}$. The spectral positions of the measurement and simulations agree very well.

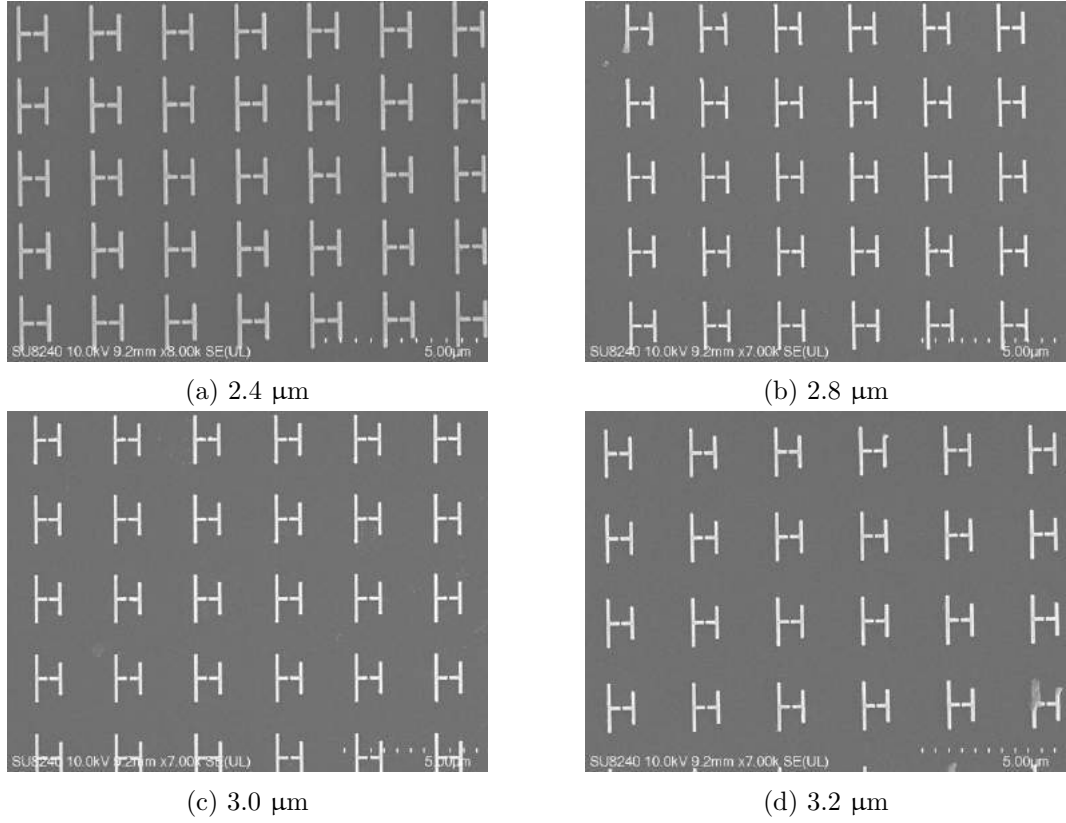


Figure 4.9: Scanning electron micrograph image of ASH nanostructures array with different periodicity (a) 2.4 μm , (b) 2.8 μm (c) 3.0 μm and (d) 3.2 μm .

In the measurement results, the resonance produced by arm length L_1 give a broad resonance peak to narrower resonance peak transition when the periodic arrangement is increased. However, the resonance produced by arm length L_2 exhibits a narrow to broad peak transition when the periodic arrangement is increased. This is due to the less coupling distance between one-unit cell. The simulation results show after the periodic arrays reach 3.2 μm (the maximum value of the arm length, L_2) it became broader and eventually disappears. This significant narrowing of the shorter wavelength peak is not shown in the measurements and is perhaps the result of grating effect in the simulations. When the incident E_X wave is excited across the symmetric crossbar, the structure exhibits single resonance in black dashed lines (Figure 4.10). It can be clearly seen in the symmetric crossbar (second column Figure 4.10) simulation results. The measurement, however, produces three resonance peaks. This is because the fabrication has in all cases not fully formed the gap between the H crossbar. In the measurement represents a combination of the two structures with likely hybridisation [35] of the two resonances leading to the appearance of the peak at $\sim 5 \mu\text{m}$.

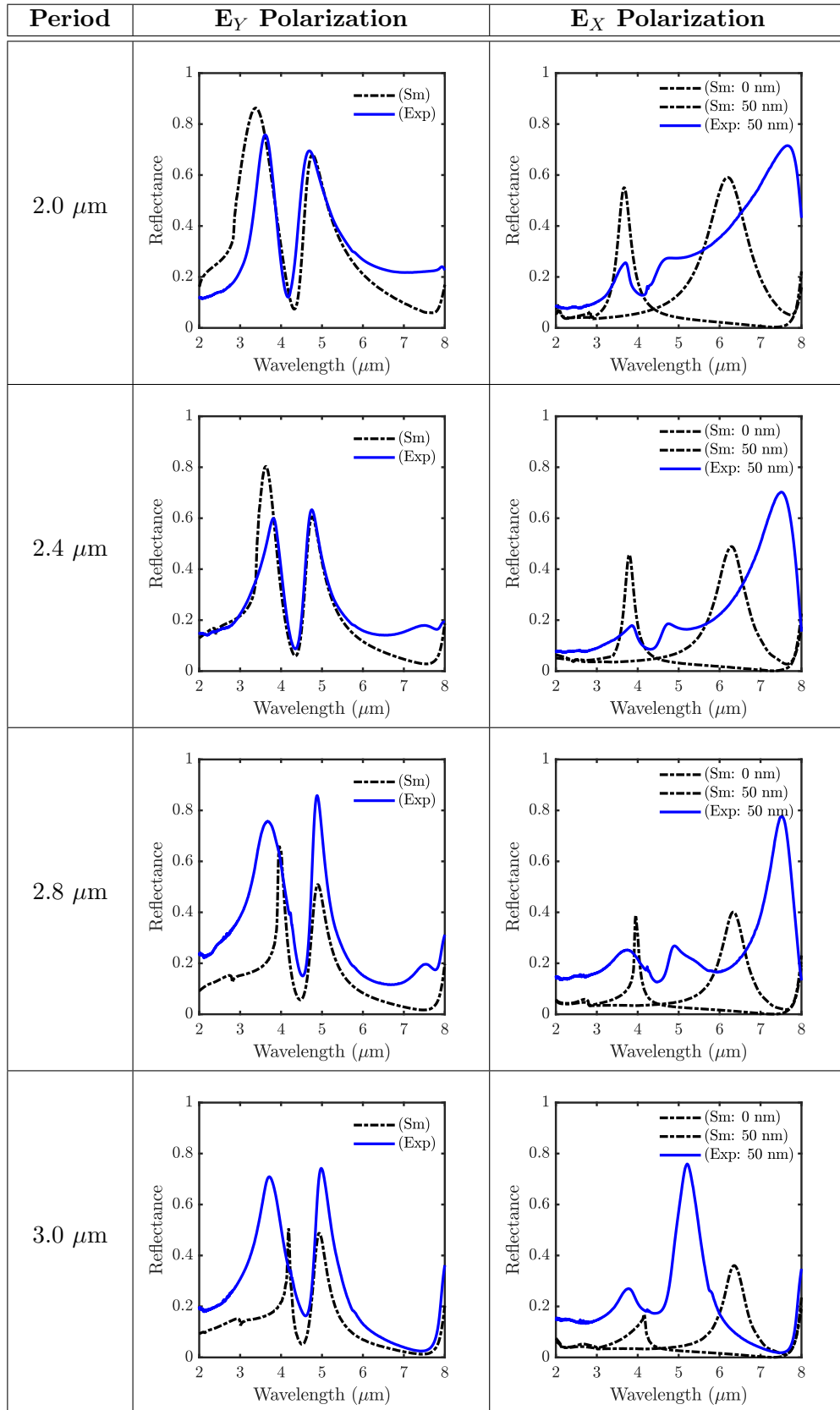


Figure 4.10: Measurement and simulation reflection spectra in different periodicity and polarization. The experimental resonance was plotted in blue line and the simulations resonance peak were plotted in black dashed line. In the E_X polarization, the simulation was performed with 0 nm gap and 50 nm gap.

The Q-factors function with periodic arrangement were plotted in Figure 4.11. The highest Q-factors, 29, was achieved in the simulation is at the resonance peak wavelength $4.2 \mu\text{m}$ with optimum periodicity $3.0 \mu\text{m}$. The highest Q-factors (Figure 4.11b) in the measurement results is 13 at the wavelength of $4.9 \mu\text{m}$ with the periodic array of $2.8 \mu\text{m}$. When the periodicity is larger than $3.2 \mu\text{m}$ in the simulation, the peak disappears due to diminishing coupling effect between nanostructures. As mentioned previously these simulations at this wavelength are characteristic of a grating effect which also manifests itself in the unusual shape of the peak. Figure 4.11c shows the dependence data of the wavelength and periodic array for the arm length, L_1 . As the periodic array increases, the wavelength of the resonance peak also increases.

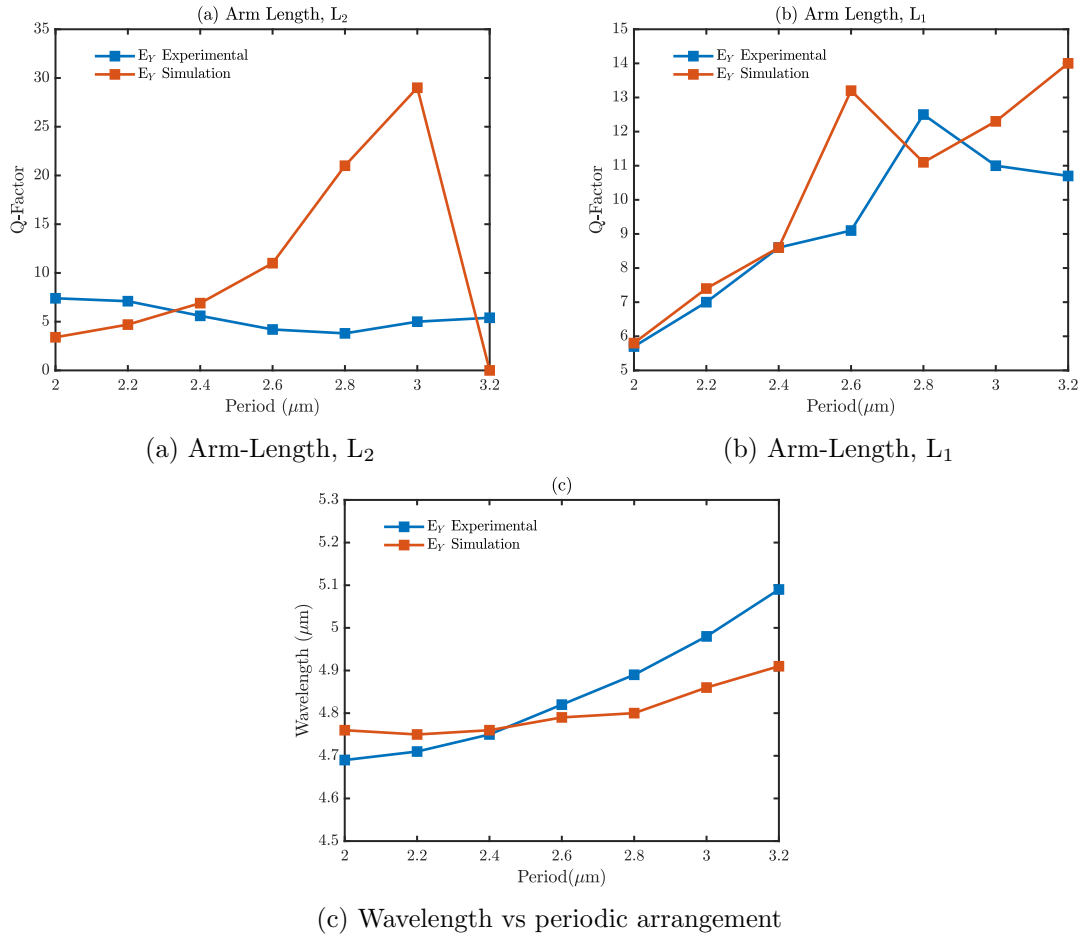


Figure 4.11: Comparison between the measurement and simulation for arm-lengths, (a) $L_2 = 1.2 \mu\text{m}$ and (b) $L_1 = 1.6 \mu\text{m}$ for Q-factors versus periodic arrangement. (c) Wavelength versus periodic arrangement for arm-lengths, L_1 .

4.6.2 Effect of the period arrangement of dual polarization ASH

This work has been published in Applied Physics Letters 112, 073105 (2018), Mbomson *et al.* [36]. The author has carried out the simulations of the fabricated structures shown in this section.

The asymmetric feature of the ASH nanostructure (D-ASH) was orthogonally designed in both x- and y-axes of the electric mode as shown in the schematic image in Figure 4.12(d). A Q-factor of 26 from both experiment and numerical simulation has been achieved in this work, by varying the array period of the D-ASH nanostructure. The asymmetric nanostructures produce two distinct plasmonic resonance peaks at 4.2 μm and 5.2 μm , that are strongly dependent on the dual polarization of the incident electromagnetic waves. By applying a sufficiently large periodic spacing in the dual-polarization dependent on the D-ASH nanostructures array, high Q-factors were achieved in the MIR region. The FDTD simulation region for the D-ASH nanostructure applied to the x- and y-axes used periodicity conditions, with array periods of 2.0 μm , 2.3 μm , 2.6 μm , 2.9 μm and 3.2 μm . The length dimensions of the horizontal asymmetrically located cross-bar sections, with a gap (g) in-between were 0.875 μm and 0.675 μm , respectively and the vertical dipoles were 1.6 μm and 1.4 μm . The width and thickness are 100 nm and the gap is 50 nm. The calculated Q-factor values for both the E_X and E_Y polarizations are based on the plasmonic resonance at the shorter wavelengths ($\sim 4.2 \mu\text{m}$) of the plots.

The plots in Figure 4.12(a)(b) show reductions in the amplitude of the resonant reflection peaks, as the array period and inter-element spacing increase, as observed in the numerical simulations. Figure 4.12(c) shows the simulation results for Q-factors in dual polarization operation for periods in the range from 2 μm to 2.9 μm . In the E_Y polarization, for a high Q-factor, a period value of 3.2 μm which is greater than twice the length of the ASH structure dipole arms was applied. For E_X polarization, the array period is approximately four times the length of the asymmetric arms of the structure. The D-ASH nanostructure arrays may be excited in dual polarization to produce a Q-factor value of 26 in the x-polarization, a value that is twice the previously reported value for plasmonic sensors in the MIR region.

To illustrate the refractive index sensing capabilities of ASH, Poly(methyl methacrylate) (PMMA) was used as analytes. A thin layer of PMMA with 50 nm thicked were simulated on top of the devices and given sensitivity value of D-ASH was 1297 nm/RIU. The presence of PMMA causes a red shifts in the spectral due to high

refractive index around the ASH ($n \sim 1.49$). In the next section 4.6.5, various refractive index value between $n=1.20$ to $n=1.59$ were varied to indicates the resonance shift that have good linearity with the refractive index value.

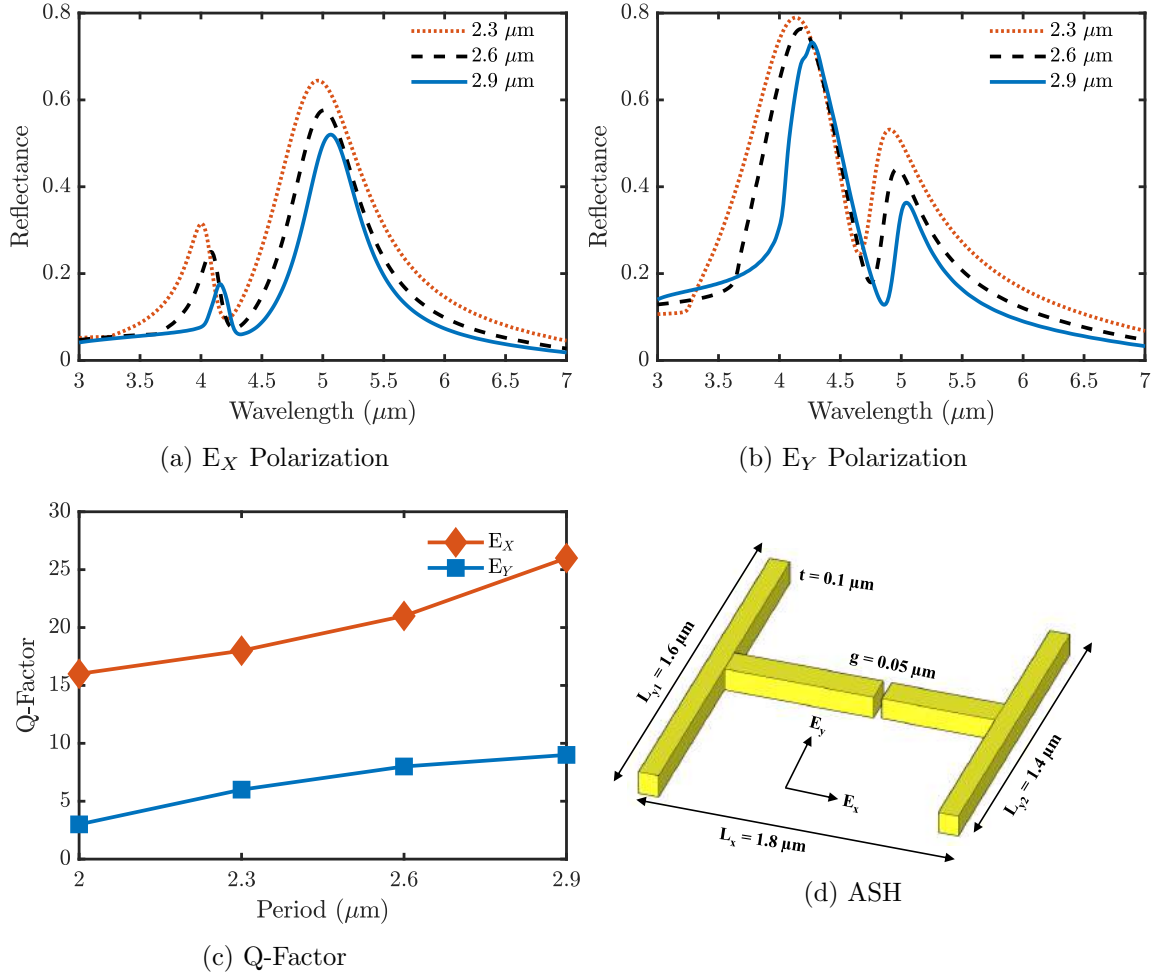


Figure 4.12: The schematic images (d) of the ASH structures on the plots for the reflectance spectral peaks obtained from numerical simulation with the electric field polarized: (a) across the gap along the x-axis and (b) along the y-axis. (c) Comparison graph of the Q-factor for the E_X and E_Y polarizations of the incident light electromagnetic waves.

4.6.3 Varying the gap of dual polarization ASH

The sizes of the vertical and horizontal dipole of dual polarization ASH (D-ASH) were maintained constant however the gap size between the horizontal dipoles shown in Figure 4.13 was varied from 0 nm to 200 nm. The E_X polarizations gave a variation in resonance peak position when the gap sizes were varied as shown in Figure 4.13(b). When ASH gap is closed, 0 nm, the total arm length of the horizontal dipole is equal to 1.55 μm and a single resonance appears at the wavelength of 7.5 μm due to the changes in the length of the dipole. The single resonance is attributed

by the excitation of the surface plasmon along the vertical dipole being parallel with the E-fields as shown in Figure 4.14. The peak positions are affected by the length as discussed earlier in Section 4.4.2. When the gap was increased to 10 nm the resonance was blue-shifted and two plasmonic resonances were produced. These effects are attributed to when the asymmetric horizontal dipoles are perpendicular to the E-fields.

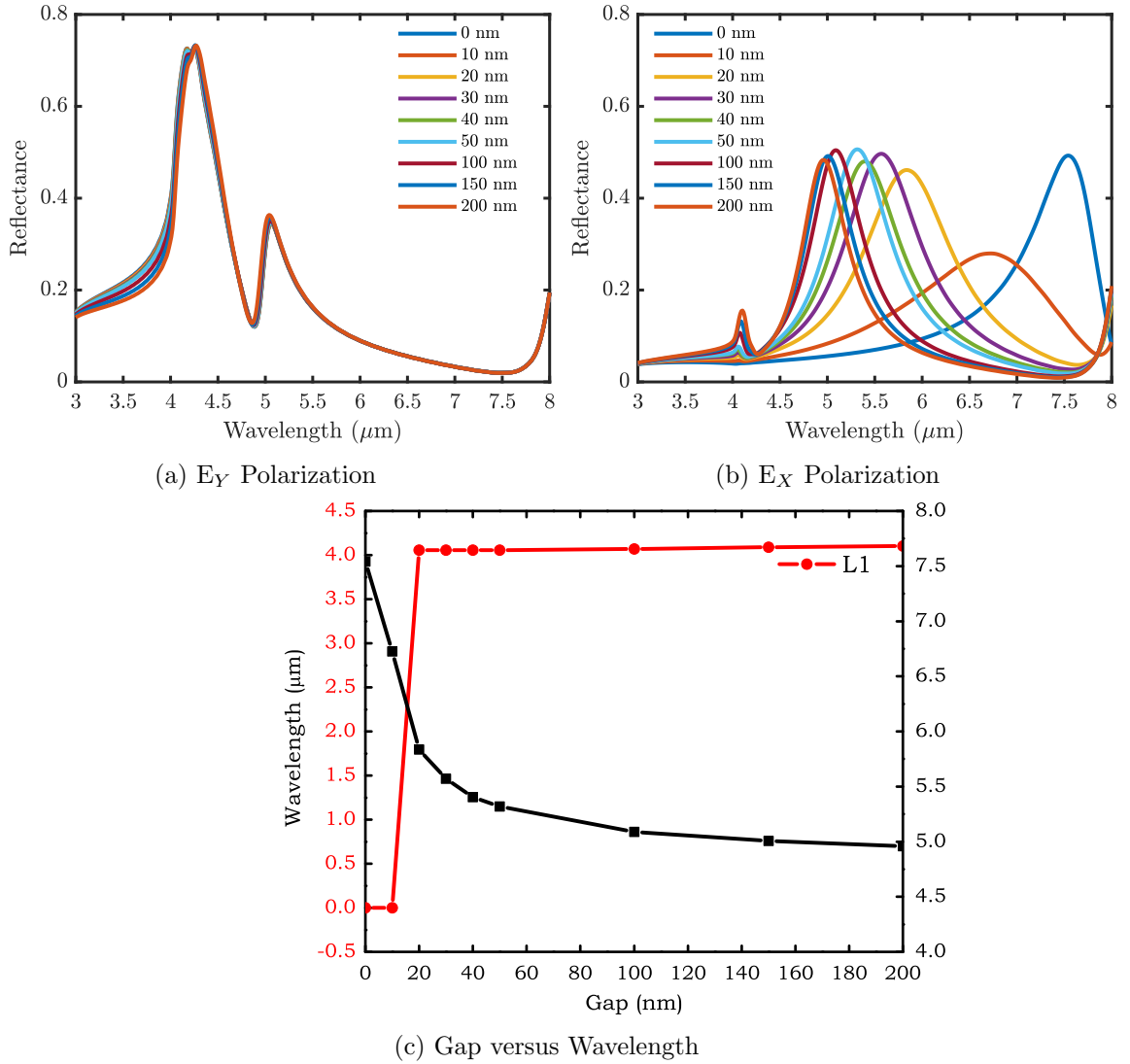


Figure 4.13: Effect on varying the gap sizes from 0 nm to 200 nm on the reflection spectra for both polarization; (a) E_Y polarization and (b) E_X polarization. (c) gap versus wavelength.

Figure 4.14 below shows the electric field (E-Field) plots of D-ASH with varying the gap from 0 nm to 200 nm. The E-field was along the horizontal asymmetrical dipole because the incident light was set to be polarized along the x-axis. The E-field monitor was placed in the centre of D-ASH and the maximum E-fields area appears at the edges of the dipoles. The dark blue shows the minimum E-field intensity and dark red shows the maximum E-field. Note that the maximum brightness of the

colour scale are different in both Figure 4.14. When the horizontal dipoles gap is 0 nm gaps, the highest level of E-fields appears at the vertical arm-length compared to 200 nm gaps where the highest E-fields surround at the gap. These areas are known as a “hot spot”; the strong electric field will trap the light energy and produce a strong absorption.

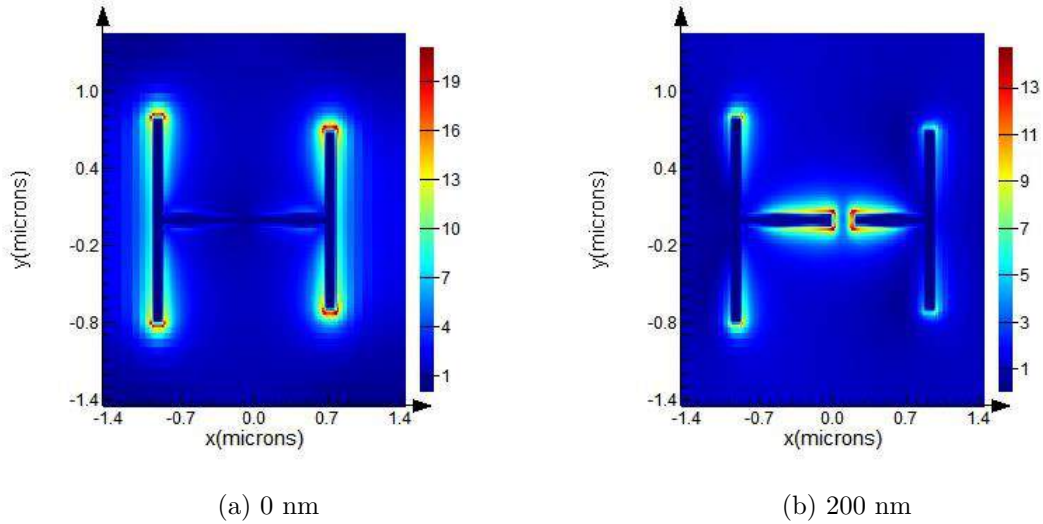


Figure 4.14: E-fields plot at the plasmonic resonance of $7.5 \mu\text{m}$ when the D-ASH with 0 nm gap and at resonance $4.28 \mu\text{m}$ with 200 nm gap.

4.6.4 Effect of different substrates

The response of metamaterial nanostructures is not solely dependent on the size and geometry parameters but also on the choice of the substrate material used. The criteria for choosing the substrate are determined by the transmission range in the infra-red [34], [37]. Generally, optical glass has a refractive index (n) range of between 1.4 to 2. An alternative substrate, ZnSe, is a transparent light-yellow colour and has advantages for aqueous solution because of a wide transmission wavelength range covering from $0.6 \mu\text{m}$ up to $21 \mu\text{m}$ compared to a fused silica substrate. operating from $0.2 \mu\text{m}$ to $4.0 \mu\text{m}$. However, fused silica substrates, due to the low refractive index and the transmittance range up to $4.0 \mu\text{m}$, can be used with metamaterials to produce a plasmonic resonance at a shorter wavelength (visible to IR). Both substrates are highly transparent and insoluble in water compared to other optical materials such as calcium fluoride (CaF_2).

The ASH nanostructures were also modelled and simulated as shown in Figure 4.15 with gold on top of the fused silica and ZnSe substrates. The geometry of the ASH was modelled using the same values on each substrate; where the arm length, L_1 and L_2 are $1.6 \mu\text{m}$ and $1.2 \mu\text{m}$. The periodic arrangement of the ASH array was

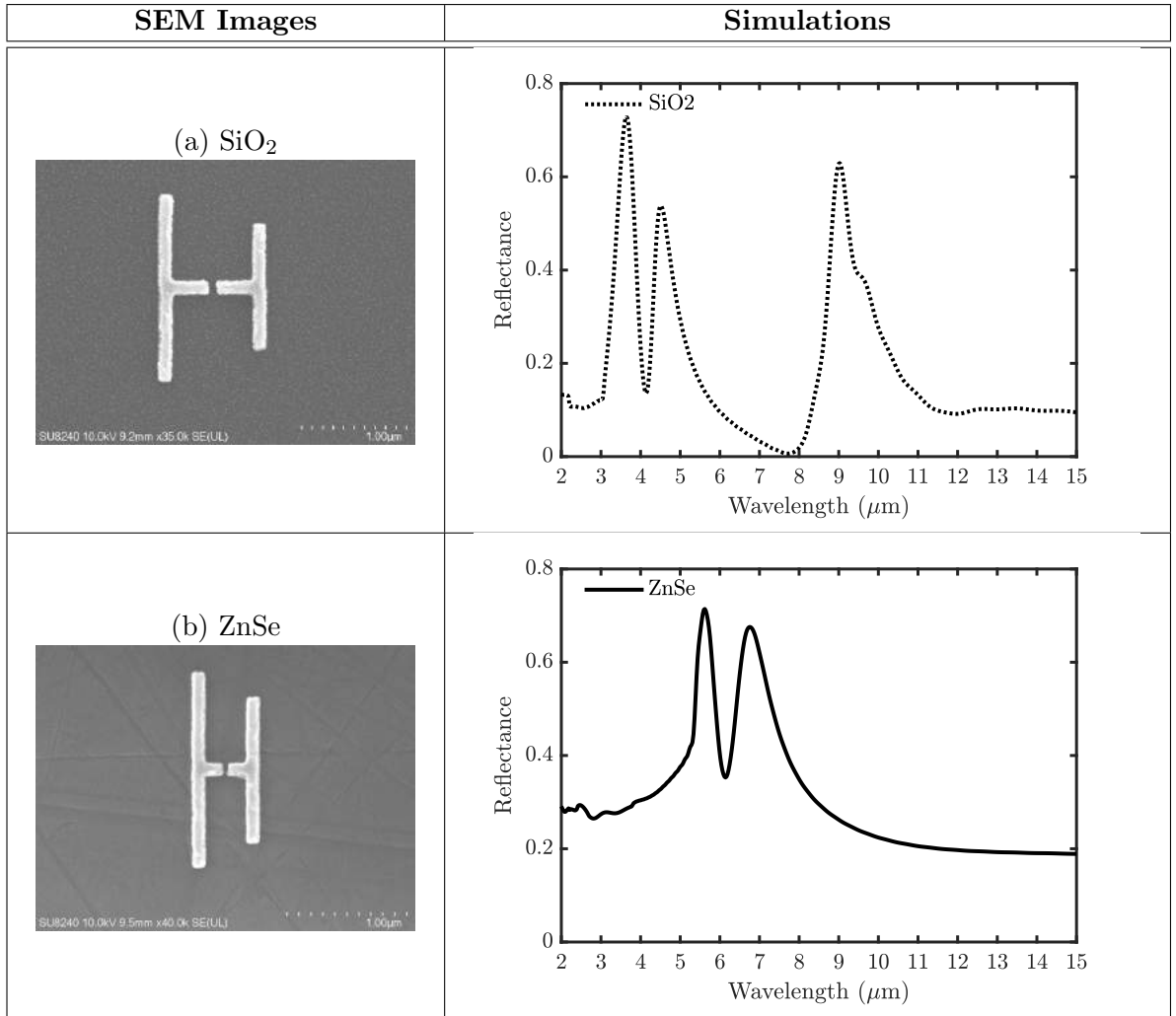


Figure 4.15: Simulation results of ASH on different substrate (a) fused silica and (b) ZnSe substrate. The incident light has been polarized parallel with the asymmetric arm length; $L_1 = 1.6 \mu\text{m}$ and $L_2 = 1.2 \mu\text{m}$.

1.1 μm in both the x and y-axis. The ZnSe substrate refractive index of $n=2.43$ data was taken from Crystran Ltd data sheets and fused silica used data from Palik [34], [37]. The ZnSe substrate has a higher refractive index than fused silica and makes the resonance shift towards longer wavelengths and produce the resonances at 5.5 μm and 6.8 μm . Figure 4.15(a) shows a resonance peak with high reflectance at 9 μm due to the fused silica substrate and the plasmonics resonance exhibit at wavelength 3.8 μm and 4.8 μm . Although the transmission range and refractive index of the ZnSe are very high, the reflection loss is up 30% as shown in Figure 4.15(b). These designed dimensions of the structures have been reduced to a smaller size to obtain the resonance at the shorter wavelength and match with the targeted wavelength.

4.6.5 Variation of the ASH arm-length on ZnSe substrate

The previous work by Mbomson *et al.*, has focused on designing and developing the ASH on a fused silica substrate [36], [38]. Although the resonance can be manipulated by changing the periodic arrangement, the sizes or the arm-length of the ASH also have an effect on producing the resonance. In this design, the periodic arrangement was set to be constant and the arm-length of the ASH on the ZnSe substrate was varied to produce the resonance peak at the targeted wavelength. The periodic arrangement was set with 1.1 μm in both x and y-axes. The ASH nanostructures on ZnSe substrates are much smaller than the sizes of ASH on the SiO_2 substrate as explained in Section 4.6.4. This is due to the ZnSe substrate having a higher refractive index than the SiO_2 substrate.

In order to optimize and demonstrate the coupling of the ASH the structures, the simulations were performed by changing the arm length L_2 and keeping a constant arm length L_1 or vice versa. This work is more focused on the response to each resonance is depending on the vertical dipole length. The arm length L_1 was varied at 0.7 μm and 0.75 μm and while the arm length L_2 was varied from 0.5 μm to 0.6 μm to exhibit a plasmonic resonance between the wavelength 2 μm to 4 μm . As the arm-length is varied, the two resonance peaks are modified by the presence of the reflection dip. Figure 4.16 shows the simulation and experimental results occur from varying the arm length L_2 . The resonance exhibits a red shift and linearly increases as the arms-length gets longer as shown in Figure 4.17a and 4.17b. When the structures are less asymmetric the resonance becomes broader and the amplitude of the resonance peak at a wavelength of 3.5 μm is reduced. The Q-factor value has been calculated and the average Q-factor is 8 for arm length L_1 and 6 for arm-length L_2 . The reflection dip given the Q-factor of 12.

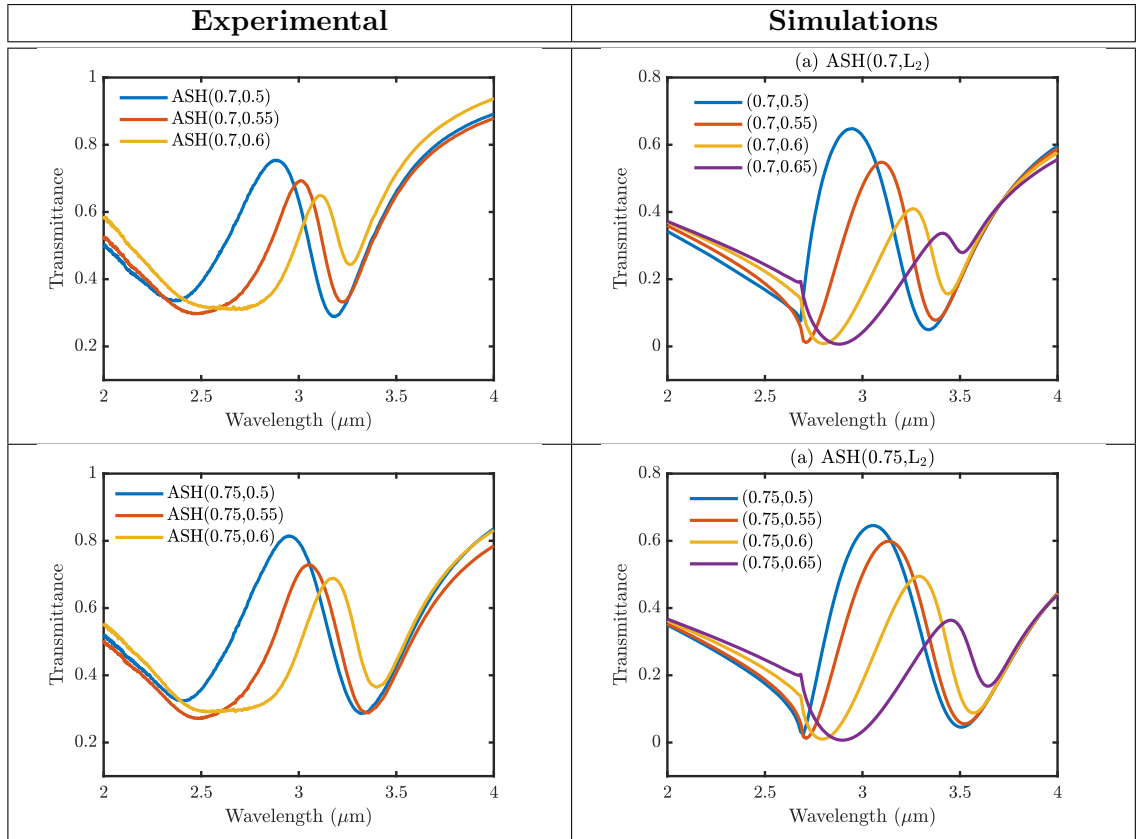


Figure 4.16: Simulation and experimental results of varying the arm length, L_2 with 500 nm, 550 nm, 600 nm, and 650 nm. The arm length, L_1 remains constant. Other parameters remain unchanged. All figures were labelled with ASH (L_1, L_2) μm .

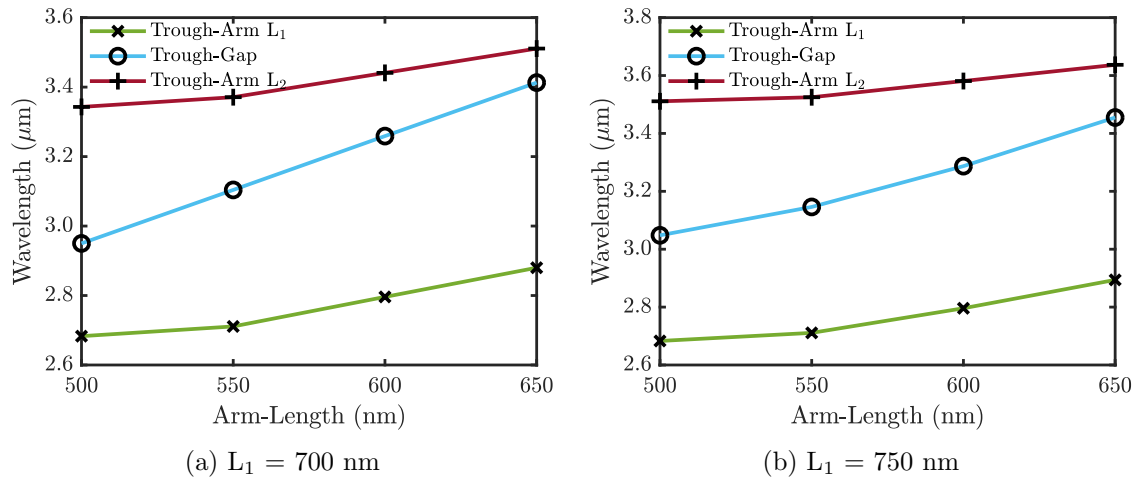


Figure 4.17: The arm-length of L_1 (nm) function of the wavelength (μm). Lines are linear fits with the arm-length (L_1, L_2 and the gap G) is increase the resonance peak position also increased.

To investigate the sensing capabilities of ASH on the ZnSe substrates, a 50 nm thin layer of different refractive indexed dielectric materials were simulated (Figure 4.18(a)). The value of the refractive index is varied from $n=1.20$ to $n=1.59$, the refractive index of water is at $n=1.33$, and the PMMA is $n=1.46$ [18]. The sensitivity were calculated from the refractive index change after the deposition of a thin layer of PMMA. The resonance of bare ASH was red-shifted and linearly increase with the sensitivity is 760 nm/RIU (Figure 4.18(c)). Hence, the resonances shifted around 350 nm from the initial position for ASHs.

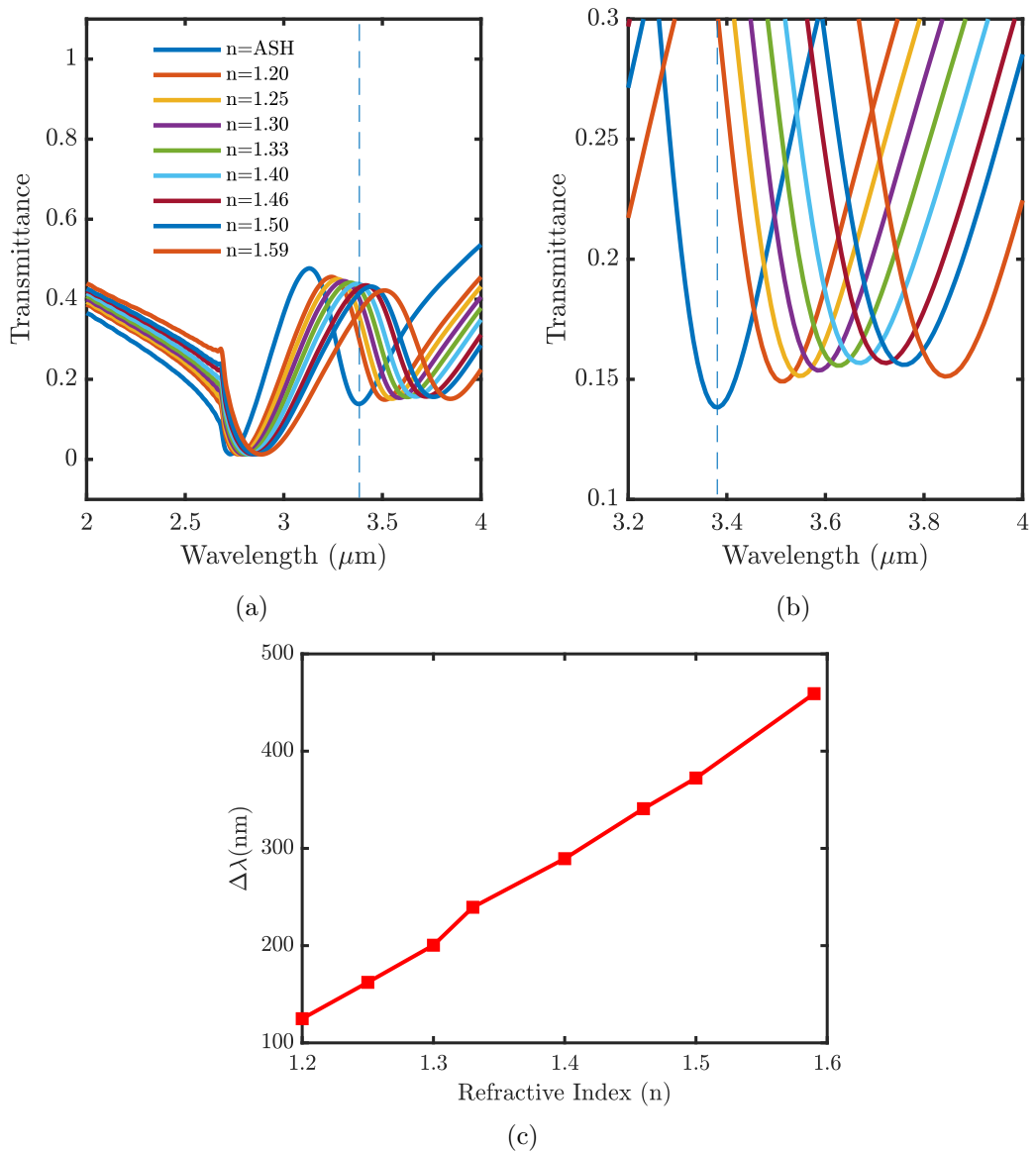


Figure 4.18: (a) Simulated transmittance spectra of a 50 nm thickness with different refractive indexed on ASH, modelled on the ZnSe substrates. (b) Zoom-in on the simulated transmittance spectra of (a). (c) Resonance shifts function ($\Delta\lambda$ nm) of the refractive index (n) of the surrounding for the ASH. Lines are linear fits

4.7 Conclusions

In conclusion, the parameters of the ASH nanostructures such as the periodic arrangement, the effect of changing the substrate and also varying the arm lengths L_1 and L_2 have been described in this chapter. All the parameters effect the resonance wavelength. The asymmetric structures give double resonance peaks with a resonance dip due to the coupling between two arms. The asymmetric structure of metamaterials has been shown to be well suited to organic sensing applications because of their tunable resonance characteristics that can be affected by the geometric sizes, gaps, periodic arrangement, high Q-factor resonance, and also the surrounding dielectric environment. D-ASH nanostructures were reported to produce a Q-factor value of 26 in the x-polarization, which is twice from what has been previously reported. The double resonance peaks produced by the ASH can be used to enhance the sensitivity for two different molecular bonds and also enable for dual polarization mode. The ASH nanostructures will be used to find good matches to the molecular resonances of target organic compounds and using surface enhanced infra-red spectroscopy (SEIRAS) as a detection tool for Mid-IR sensing for organic compounds.

References

- [1] V. M. Shalaev, “Optical negative-index metamaterials,” *Nature Photonics*, vol. 1, no. 1, pp. 41–48, Jan. 2007 (cit. on p. 47).
- [2] A. Boardman, “Pioneers in metamaterials: John Pendry and Victor Veselago,” *Journal of Optics*, vol. 13, no. 2, p. 020401, 2010 (cit. on p. 47).
- [3] S. J. Pendry, “Metamaterials and the Control of Electromagnetic Fields,” EN, in *Conference on Coherence and Quantum Optics*, Washington, D.C.: OSA, Jun. 2007, CMB2 (cit. on p. 47).
- [4] M. Jahn, S. Patze, I. J. Hidi, R. Knipper, A. I. Radu, A. Mühlig, S. Yüksel, V. Peksa, K. Weber, T. Mayerhöfer, D. Cialla-May, and J. Popp, *Plasmonic nanostructures for surface enhanced spectroscopic methods*, 2016. [Online]. Available: <http://xlink.rsc.org/?DOI=C5AN02057C> (cit. on p. 48).
- [5] N. A. Hatab, C. H. Hsueh, A. L. Gaddis, S. T. Retterer, J. H. Li, G. Eres, Z. Zhang, and B. Gu, “Free-Standing Optical Gold Bowtie Nanoantenna with Variable Gap Size for Enhanced Raman Spectroscopy,” *Nano Letters*, vol. 10, no. 12, pp. 4952–4955, Dec. 2010 (cit. on p. 48).
- [6] L. J. Sherry, R. Jin, C. A. Mirkin, G. C. Schatz, and R. P. Van Duyne, “Localized Surface Plasmon Resonance Spectroscopy of Single Silver Triangular Nanoprisms,” *Nano Letters*, vol. 6, no. 9, pp. 2060–2065, Sep. 2006 (cit. on p. 48).
- [7] T. Chung, S. Y. Lee, E. Y. Song, H. Chun, and B. Lee, “Plasmonic nanostructures for nano-scale bio-sensing,” *Sensors*, vol. 11, no. 11, pp. 10907–10929, Nov. 2011 (cit. on p. 48).
- [8] A. Lovera, B. Gallinet, P. Nordlander, and O. J. F. Martin, “Mechanisms of fano resonances in coupled plasmonic systems,” *ACS Nano*, vol. 7, no. 5, pp. 4527–4536, 2013 (cit. on p. 48).
- [9] V. Giannini, Y. Francescato, H. Amrania, C. C. Phillips, and S. A. Maier, “Fano Resonances in Nanoscale Plasmonic Systems: A Parameter-Free Modeling Approach,” *Nano Letters*, vol. 11, no. 7, pp. 2835–2840, Jul. 2011 (cit. on p. 48).
- [10] S. E. Mendhe and Y. P. Kosta, “Metamaterial properties and applications,” *International Journal of Information Technology and Knowledge Management*, vol. 4, no. 1, pp. 85–89, 2011 (cit. on p. 48).

- [11] N. Verellen, P. Van Dorpe, C. Huang, K. Lodewijks, G. A. E. Vandenbosch, L. Lagae, and V. V. Moshchalkov, “Plasmon line shaping using nanocrosses for high sensitivity localized surface plasmon resonance sensing,” *Nano Letters*, vol. 11, no. 2, pp. 391–397, Feb. 2011 (cit. on p. 48).
- [12] S. D. Liu, Z. Yang, R. P. Liu, and X. Y. Li, “Multiple fano resonances in plasmonic heptamer clusters composed of split nanorings,” *ACS Nano*, vol. 6, no. 7, pp. 6260–6271, 2012 (cit. on p. 48).
- [13] Y. Moritake, Y. Kanamori, and K. Hane, “Demonstration of sharp multiple Fano resonances in optical metamaterials,” *Optics Express*, vol. 24, no. 9, p. 9332, May 2016 (cit. on p. 49).
- [14] C.-Y. Chen and P.-H. Hsiao, “Position-dependent sensing performance of coupled resonators with symmetry breaking,” *Journal of Physics D: Applied Physics*, vol. 49, no. 13, p. 135101, Apr. 2016 (cit. on p. 49).
- [15] Y. Y. Yang and L. X. Zhang, “Manipulating Light in Coupled Asymmetric Nanostructures Induced by a Visible–NIR Laser,” *Journal of Russian Laser Research*, vol. 39, no. 3, pp. 267–274, May 2018 (cit. on p. 49).
- [16] K.-H. Kim, S.-H. Kim, and M.-C. Bae, “Fano resonance by dipole – hexapole coupling in a χ -shaped plasmonic nanostructure,” *Appl. Opt.*, vol. 54, no. 10, pp. 2710–2714, Apr. 2015 (cit. on p. 49).
- [17] V. A. Fedotov, M. Rose, S. L. Prosvirnin, N. Papasimakis, and N. I. Zheludev, “Sharp Trapped-Mode Resonances in Planar Metamaterials with a Broken Structural Symmetry,” *Physical Review Letters*, vol. 99, no. 14, p. 147401, Oct. 2007 (cit. on pp. 50–52).
- [18] B. Lahiri, A. Z. Khokhar, R. M. De La Rue, S. G. McMeekin, and N. P. Johnson, “Asymmetric split ring resonators for optical sensing of organic materials,” *Optics Express*, vol. 17, no. 2, p. 1107, Jan. 2009 (cit. on pp. 51, 53, 71).
- [19] J. Chae, B. Lahiri, and A. Centrone, “Engineering Near-Field SEIRA Enhancements in Plasmonic Resonators,” EN, *ACS Photonics*, vol. 3, no. 1, pp. 87–95, Jan. 2016 (cit. on pp. 51, 53).
- [20] I. G. Mbomson, S. G. McMeekin, R. M. De La Rue, and N. P. Johnson, “The effect of geometry on the quality factor of resonance peaks in asymmetric nano-antennas at mid-infrared wavelengths,” in *SPIE Optics + Optoelectronics*, V. Kuzmiak, P. Markos, and T. Szoplik, Eds., International Society for Optics and Photonics, May 2015, p. 95020L (cit. on pp. 51, 53, 60).
- [21] B. Lahiri, “Split Ring Resonator (SRR) based metamaterials,” PhD thesis, University of Glasgow, 2010 (cit. on pp. 52, 58).

- [22] L. Wu, Z. Yang, M. Zhao, Y. Zheng, J. Duan, and X. Yuan, “Polarization-insensitive resonances with high quality-factors in meta-molecule metamaterials,” *Optics Express*, vol. 22, no. 12, p. 14 588, 2014 (cit. on pp. 52, 60).
- [23] M. J. Dicken, K. Aydin, I. M. Pryce, L. A. Sweatlock, E. M. Boyd, S. Walavalkar, J. Ma, and H. a. Atwater, “Frequency tunable near-infrared metamaterials based on VO₂ phase transition,” *Opt. Express*, vol. 17, no. 20, pp. 18 330–18 339, Sep. 2009 (cit. on p. 53).
- [24] W. Yue, Z. Wang, J. Whittaker, F. Schedin, Z. Wu, and J. Han, “Resonance control of mid-infrared metamaterials using arrays of split-ring resonator pairs,” *Nanotechnology*, vol. 27, no. 5, p. 055 303, Feb. 2016 (cit. on p. 53).
- [25] K. Aydin, I. M. Pryce, and H. a. Atwater, “Symmetry breaking and strong coupling in planar optical metamaterials,” *Optics express*, vol. 18, no. 13, pp. 13 407–13 417, 2010 (cit. on p. 53).
- [26] E. D. Palik, “List of Contributors for Volume III,” in *Handbook of Optical Constants of Solids*, vol. 2, Elsevier, 1997, pp. xiii–xv (cit. on p. 54).
- [27] S. Linden, “Magnetic Response of Metamaterials at 100 Terahertz,” *Science*, vol. 306, no. 5700, pp. 1351–1353, Nov. 2004. arXiv: [science.1105371](https://arxiv.org/abs/science.1105371) [10.1126] (cit. on p. 54).
- [28] H. Guo, N. Liu, L. Fu, T. P. Meyrath, T. Zentgraf, H. Schweizer, and H. Giessen, “Resonance hybridization in double split-ring resonator metamaterials,” *Optics Express*, vol. 15, no. 19, p. 12 095, Sep. 2007 (cit. on p. 56).
- [29] L. Na, G. Hongcang, F. Liwei, H. Schweizer, S. Kaiser, and H. Giessen, “Electromagnetic resonances in single and double split-ring resonator metamaterials in the near infrared spectral region,” in *Physica Status Solidi (B) Basic Research*, vol. 244, John Wiley & Sons, Ltd, Apr. 2007, pp. 1251–1255 (cit. on p. 56).
- [30] B. Lahiri, S. G. McMeekin, R. M. De La Rue, and N. P. Johnson, “Resonance hybridization in nanoantenna arrays based on asymmetric split-ring resonators,” *Applied Physics Letters*, vol. 98, no. 15, p. 153 116, 2011 (cit. on p. 56).
- [31] S. M. Kandil, I. A. Eshrah, I. S. El Babli, and A. H. Badawi, “Plasmon hybridization in split ring nanosandwich for refractive index sensing– Numerical Investigation,” *Optics Express*, vol. 24, no. 26, p. 30 201, Dec. 2016 (cit. on p. 56).
- [32] I. G. Mbomson, “Mid-infrared photonic sensors based on metamaterial structures,” PhD thesis, University of Glasgow, 2016 (cit. on pp. 56, 58).

- [33] G. J. Sharp, “Metamaterials and optical sensing at visible and near infra-red wavelengths,” PhD thesis, University of Glasgow, 2015 (cit. on p. 58).
- [34] Crystran Ltd., “Zinc Selenide (ZnSe) Optical Material,” pp. 3–4, 2018 (cit. on pp. 59, 67, 68).
- [35] T. Chen, S. Li, and H. Sun, “Metamaterials application in sensing.,” en, *Sensors (Basel, Switzerland)*, vol. 12, no. 3, pp. 2742–65, Jan. 2012 (cit. on pp. 60, 61).
- [36] I. G. Mbomson, I. F. Mohamad Ali Nasri, R. M. De La Rue, and N. P. Johnson, “Dual polarization operation of nanostructure arrays in the mid-infrared,” *Applied Physics Letters*, vol. 112, no. 7, p. 073 105, Feb. 2018 (cit. on pp. 64, 69).
- [37] E. D. Palik, *Palik, Handbook of Optical Constants of Solids, Vol.2*. 1991, vol. 2 (cit. on pp. 67, 68).
- [38] I. G. Mbomson, S. Tabor, B. Lahiri, G. J. Sharp, S. G. McMeekin, R. M. De La Rue, and N. P. Johnson, “Asymmetric split H-shape nanoantennas for molecular sensing,” *Biomedical Optics Express*, vol. 8, no. 1, p. 395, Jan. 2017 (cit. on p. 69).

Chapter 5

Detection of estrogenic hormones using plasmonic nanostructures

5.1 Abstract

Due to their sensitivity and flexibility, metamaterial structures such as nanoantennas have been widely employed as label-free optical sensors for the detection of organic compounds. Detection, however, has so far often mostly exploited sensors with only a single plasmonic resonance. By optimising the geometry of asymmetric split-H (ASH) resonators that are formed by a crossbar (with a gap) placed between asymmetric (unequal arm-length) vertical dipoles, double plasmonic resonances was successfully produced. The particular ASH design has been demonstrated where resonances are controllably tuned to align with the molecular vibration resonances of C-H (at 3.42 μm and 3.49 μm), C=O (at 5.8 μm) and C=C (6.63 μm and 6.68 μm) bonds of the four estrogenic hormones. The devices were fabricated on zinc selenide (ZnSe) substrates and the resonances are clearly red-shifted with when the hormones are deposited, from solution, on the ASH structures.

5.2 Estrogenic hormones

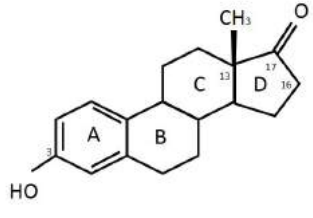
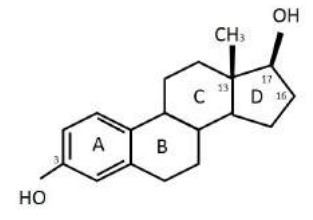
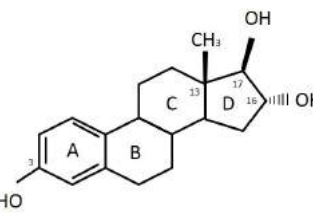
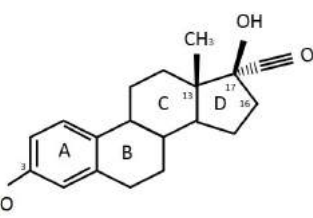
Estrogenic hormones are a class of endocrine-disrupting compounds (EDC) that are discovered regularly in various water sources. Estrogens in the environment mainly originate from humans and animals excretions and from industrial and agricultural waste [1]–[3]. They have been found at low concentrations around the water surface of groundwater due to its poor solubility [4]. EDC contamination can potentially be found in food, in water supply and in consumer products and can lead to adverse health effects, particularly with regard to reproduction and developmental growth. The EU government has recommended monitoring the issues in the wa-

ter because of the potential harm to aquatic species, such as alterations of sexual development and inter-sex species (e.g feminization of male fish) [1], [5]–[8]. Several traditional analytical methods have been used to measure estrogens such as gas chromatography (GC), high-performance liquid chromatography (HPLC), human estrogen-receptor (hER) sensors, spectroscopic methods, immunosensors and biosensors [4], [8]–[10]. The HPLC and GC methods are typically highly automated and very sensitive and specific for the detection and observation of multiple species at trace level. Although these methods provide accurate and sensitive detections, they are very time-consuming, expensive and complicated and cannot be deployed as in the field [11].

The natural estrogenic hormones are Estrone (E1), 17β -Estradiol (E2), Estriol (E3); where 17α -Ethinyl Estradiol (EE2) is the most common synthetic estrogen [1], [12], [13]. 17β -Estradiol is the most potent hormone found in females. Estrone can be found after the menopause stage. 17β -Estradiol is the main strongest estrogen found in females for growing, reproductive, and childbearing women and estriol is produced during pregnancy [5]. E2 is most stable in air and possesses the highest hydrophobicity but it is freely soluble in ethanol or other alcohols. EE2 is used in contraceptive pills to make the estrogen more stable and as a post-menopausal hormone replacement [14]. It remains longer in the body compared to natural estrogens. Estrone can be found in the human body after menopause and it is less biologically active than E2 [14]. Estriol is the most abundant estrogenic hormone; it is produced by the placenta during pregnancy and practically insoluble in water, and it is soluble in alcohol, dioxane, vegetable oil and ether. In comparison to estrone and 17β -estradiol, estriol is the weakest hormones. Estrogenic hormones can also have negative effects on physiological processes; breast and endometrial cancer can occur if there is insufficient or too much estrogen in the body [15].

The four estrogenic hormones share the same tetracyclic molecular form with four rings that have a phenolic ring (A), two cyclohexanes (B and C) and one cyclopentane (D) rings in their chemical structures as shown in Table 5.1 [5], [16]. All estrogens have the same substituent, a phenolic OH group on the A-ring. The differences between the four estrogenic hormones are substituents on the cyclopentane ring (D-ring) at the position C16 and C17. E1 has a carbonyl group at C17, E2 has a hydroxyl group at C17, E3 and EE2 have the two-hydroxyl group at C16 and C17.

Table 5.1: Illustration of (a) Estrone (b) 17β -Estradiol (c) Estriol and (d) 17α -Ethinyl Estradiol chemical structures showing the common regions and in functional groups.

Compound	Formula	Molecular Weight (g/mol)	Chemical Structure	Ref
Estrone (E1)	$C_{18}H_{22}O_4$	270.366		[17]
17β -Estradiol (E2)	$C_{18}H_{24}O_4$	272.38		[18]
Estriol (E3)	$C_{18}H_{24}O_3$	288.38		[19]
17α -Ethinyl Estradiol (EE2)	$C_{20}H_{24}O_6$	296.403		[20]

This chapter presents the fabrication and characterization of plasmonic metamaterial nanostructures arrays based on asymmetric split H-shape (ASH) structures that has been designed and optimized to produce plasmonic resonances that matched the molecular vibrations of the four estrogens presented in Table 5.1. Estrogenic hormones were chosen as analytes for coupling with plasmonic resonances. The aim was to identify the common and different molecular bonding between the four estrogens in the infrared wavelengths. The resonances were measured at normal incidence using a microscope coupled Fourier Transform Infrared (FTIR) spectrometer and observed at mid-infrared wavelengths in the range between 2 and 8 μm , both experimentally and by simulation. Two geometries of ASH resonators, labelled as ASH₁ and ASH₂, were fabricated on a zinc selenide (ZnSe) substrate. ZnSe substrate was chosen because it is a transparent and high refractive index materials that enables the detection over a broader wavelength range from 600 nm to 21 μm . The results

show that the distinct plasmonic resonances are match closely with the five molecular bond resonances (for O-H, C-H, C=O, C=C and C≡C-H bonds) observed for estrogens and that it is possible to differentiate E2 in mixture with E1, E3 and EE2. The purpose of modelling the ASH nanostructures is to design a multiband molecular sensor for a detection of the estrogenic hormone.

5.3 Materials and Methods

5.3.1 Gold nanostructures fabrication

The gold nanostructures were fabricated using electron beam lithography on a ZnSe substrate. ZnSe substrates were purchased from Crystran Ltd [21], [22]. The substrates were cleaned in an ultrasonic bath and a bilayer of PMMA positive resists was spun on top of the substrate, producing a thickness of 400 nm. A thin layer of aluminium deposited over the PMMA bilayer resists acts as a charge dissipation layer to avoid charging effect during patterning. After the patterning, the samples were developed with IPA:RO water (ratio 7:3). A 10 nm thick of titanium film, used as an adhesion layer and 100 nm of gold were deposited followed by the lift-off process in warm acetone. The pattern was written over a square array with an area of approximately $400 \times 400 \mu\text{m}^2$ and consisting of 160 000 ASHs. Oxygen plasma was used to remove residues of the resists on the surface before metallisation and after lift-off.

5.3.2 FTIR measurement

Fourier Transform Infrared (FTIR) transmittance spectra of gold nanostructures arrays were measured in normal incidence using Bruker Vertex 70 spectrometer coupled to Nicolet Continuum Hyperion microscope with Cassegrain objective (15 \times , NA = 0.4) and KBr beamsplitter in the range of 8000 to 400 cm^{-1} (1.25 μm to 16.67 μm). A liquid nitrogen-cooled mercury-cadmium-telluride (MCT) detector was used in the measurement detector to measure the interferogram signal, which was converted into the spectrum. The IR spectra were collected in the same area for all array with aperture sizes of $380 \times 380 \mu\text{m}^2$. The FTIR beam was polarized using ZnSe IR polarizer inserted in the beam path before the sample. All the measurement spectra were normalized to the transmittance of plain ZnSe substrate. The interferometer was maintained under the vacuum and the microscope was constantly purged with nitrogen gas to eliminate water and CO₂ influence.

5.3.3 FDTD simulations

To verify the experimental measurement, the structures were modelled and simulations were carried out using Lumerical finite difference time domain (FDTD) Simulation software [23] modelled with gold on top of the ZnSe substrate and using data from Palik [24] for the complex refractive index of gold. The ZnSe substrate refractive index of $n=2.43$ was taken from Crystran Ltd material data sheets [21]. The simulations used periodic boundary conditions along the x and y-axes with equal periodicity to simulate an infinite array in both directions. A perfect-matched layer (PML) was used for the z-axis with a wavelengths range between 2 μm and 8 μm . A plane wave source and power monitors were used to obtain the reflectance and transmittance simulation spectra.

5.3.4 Estrogenic hormone preparation

Estrone (E1) (99% purity) was purchased in powder form from Acros Organic, and 17 β -Estradiol (E2) (98% purity), Estriol (E3) (98% purity), and 17 α -Ethinyl Estradiol (EE2) (98% purity) were purchased from Sigma Aldrich. All the stock solutions for E1, E2, E3, and EE2 were prepared in absolute ethanol (EtOH) with a concentration of 1 mg/ml and formed clear solutions after sonication for five minutes. 10 μl of the solutions was deposited on a ZnSe substrate and allowed to evaporate overnight in order for the estrogen to crystalize on top of the substrate [25]. The solutions for the mixture of two estrogens were prepared with 4 mg of each powder in 4 ml of EtOH, giving a total concentration of 2 mg/ml estrogens with a 50:50 ratio or 1 + 1 mg/ml. Then, five different ratios of E2 to E1 were prepared, 50:50, 37.5:62.5, 25:75, 12.5:87.5, and 0:100 that is corresponding to 1 + 1 mg/ml, 0.75 + 1.25 mg/ml, 0.5 + 1.5 mg/ml, 0.25 + 1.75 mg/ml and 0 + 2 mg/ml. The molecular deposition was carried out at room temperature under the fume hood cabinet. Between experiments, the solutions were kept in a -20°C freezer.

5.4 Results and discussions

5.4.1 Molecular bonds of the estrogenic hormones

The bond vibration fingerprint of the estrogenic hormones were recorded with FTIR over the broadband range from 1.25 μm to 16.67 μm (8000 – 600 cm^{-1}). The spectral region can be divided into four regions; single bonds (N-H, O-H, C-H bond) appear between 2.5 and 4.0 μm or 4000 and 2500 cm^{-1} , double bonds (C=O, C=N, C=C) between 5.0 and 7.69 μm or 2000 and 1300 cm^{-1} and triple bonds (C \equiv C,

$\text{C}\equiv\text{N}$) between 6.7 and 25 μm or 1400 and 400 cm^{-1} [26].

Between 4.2 μm and 4.3 μm (2380 and 2300 cm^{-1}), all spectra displayed two peaks from atmospheric CO_2 while ripples from atmospheric water (H_2O) vapour were present in the region between 2.50 μm and 2.85 μm (4000 and 3508 cm^{-1}). The CO_2 peaks are not displayed on the figures. E1, E2, E3 and EE2 absorbed in the infrared radiation between 2.98 μm and 3.45 μm and 5.70 μm and 6.80 μm as shown in the zoomed in spectra on Figure 5.1. The circular black dashed line indicates molecular vibrational bonds of O-H, C-H, C=O, C=C and C \equiv C-H. Phenolic O-H bond absorbs between 2.86 and 3.10 μm (3496 and 3225 cm^{-1}) in the broadband. The strong and sharp peaks featured around 3.40 and 3.43 μm (2941 to 2915 cm^{-1}) and 3.49 to 3.51 μm (2865 to 2849 cm^{-1}) were present in all four spectra due to the absorption by the C-H bonds in the group CH_2 and CH_3 . Most of C-H bonds in the analytes had fairly strong absorptions band. The peak corresponding to carbon to carbon double bonds stretching (C=C) appears at the wavelength ranges of 6.23 μm to 6.68 μm (1605 to 1496 cm^{-1}). The unique features of individual estrogen compounds can be seen in Figure 5.1. The C \equiv C stretching bond of EE2 absorbs at 3.03 μm (3300 cm^{-1}) and C=O bond of E1 in the range between 5.79 μm and 5.85 μm (1727 and 1709 cm^{-1}) (see Table 5.2). The estrogenic hormones peak positions and peak shapes are in good agreement with literature and infrared spectrum by NIST Chemistry WebBook [17]–[20]. Table 5.2 summaries the observable molecular vibrations and absorption for all four estrogenic hormones using FTIR spectroscopy.

Samples of the estrogens deposited on unpatterned ZnSe substrates were characterized by atomic force microscopy (AFM) for thickness and crystallization behavior (see in Appendix Figure A.1). The thickness of the crystallized estrogen films as measured in 2D images range from 50 to 600 nm; E1 giving an average thickness of $E1 \pm 400$ nm, $E2 \pm 100$ nm, $E3 \pm 600$ nm and $EE2 \pm 50$ nm. The AFM profiles showed the large variations in the roughness on the deposited surface. To understand these variations, microscopic images of the samples were produced with 5 \times and 100 \times magnification (Figure 5.2). E2 and EE2 crystallised in small homogenous spheres, while E3 formed bigger aggregates of rod-shaped crystals. The crystallization of E1 was very heterogenous presenting large clusters of crystals.

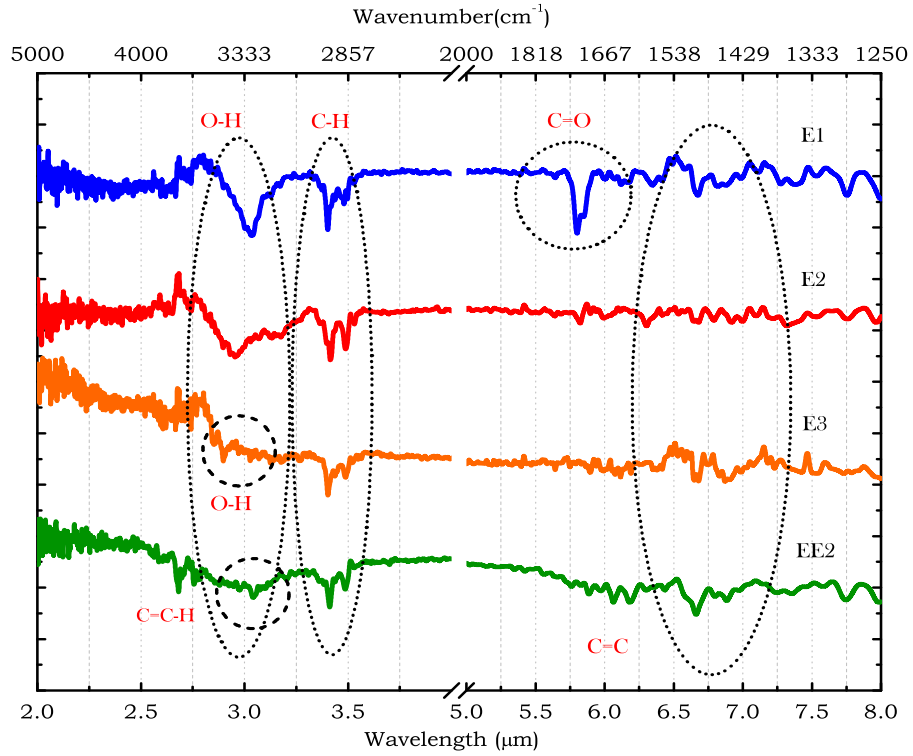


Figure 5.1: The magnified transmittance measurement results of the 10 μg estrogenic hormones deposited on the plain ZnSe substrates between 2.00 μm to 8.00 μm . The signals were recorded with $380 \times 380 \mu\text{m}^2$ sized area. For the purpose of better visibility, shows in the stacked plot. The circular dashed line indicates the molecular vibrational bonds of O-H, C-H, C=O, C=C and C \equiv C-H appeared in estrogenic hormone spectra.

Table 5.2: The summary of molecular vibrational peaks and absorption features extracted from the estrogenic hormones deposited on plain ZnSe substrate in the mid-IR wavelength between 2.00 μm to 8.00 μm .

Molecular Bonds	E1 (μm)	E2 (μm)	E3 (μm)	EE2 (μm)
O-H (C17)		2.96	2.90	2.92
O-H (C16)	3.05		3.05	
C \equiv CH				3.03
C-H	3.40	3.41	3.41	3.41
C-H	3.48	3.49	3.48	3.48
C=O	5.79			
C=O	5.85			
C=C	6.30	6.30	6.30	6.30
C=C	6.67	6.67	6.67	6.67
C=C	6.80	6.80	6.80	6.80
C17-O-H	7.76	7.76		
C16-O-H				

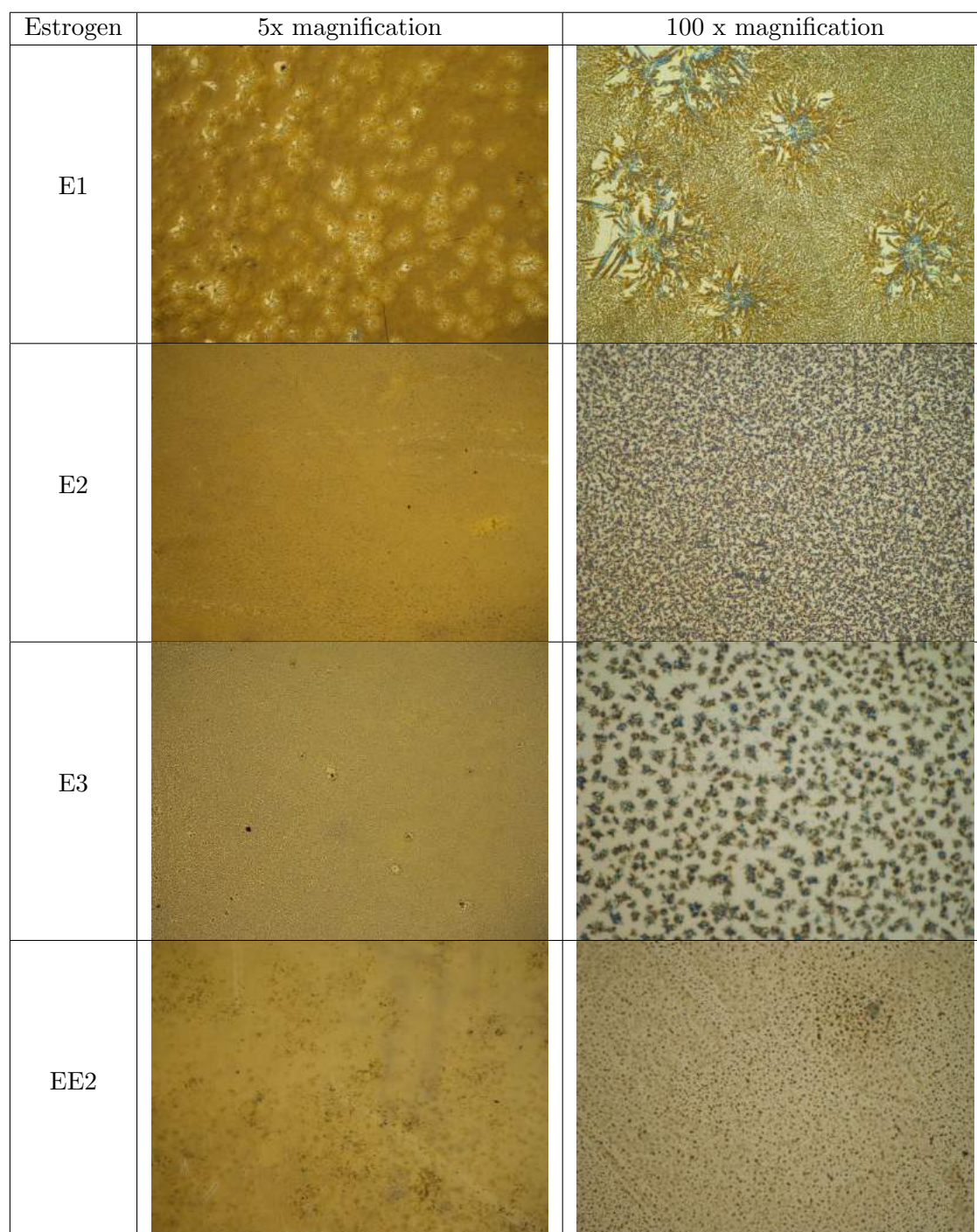


Figure 5.2: The microscope images of the 10 μg estrogenic hormones on the plain ZnSe substrates with 5x and 100x magnification.

5.4.2 Matching the molecular bonds of estrogens with ASH resonance

The fabricated ASHs had two arms of different lengths, which produced two plasmonic resonances due to coupling. Their thickness (t) and width (w) were 100 nm and they presented a constant gap (g) of 50 nm between the cross-bar dipoles. The lateral spacing between the ASHs along the x and y-axes were 1.1 μm for ASH₁ and 2.2 μm for ASH₂ and were fixed for all array sizes of $400 \times 400 \mu\text{m}^2$. In order to optimise their sensing capability, the arm lengths of the ASHs were tuned so their resonances matched or overlapped with the molecular vibrations of the estrogens as presented in Table 5.2. To be able to cover the plasmonic resonance in the mid IR wavelength range between 2 to 8 μm , ASH structures with two sets of different dimensions were designed; ASH₁, the smaller structure, with arm lengths between 450 nm and 800 nm, and ASH₂, the bigger structure, with double the arm lengths (1.2 μm to 1.6 μm). The FTIR transmittance spectra were measured at normal incidence, where the incident wave is polarized along the y-axis, parallel with the vertical asymmetric arms. Reference measurements were performed on the plain ZnSe substrate. The effects of varying the arm lengths can be seen in Figure 5.3; L_1 and L_2 were varied from 450 nm to 800 nm (ASH₁) and 1.2 μm to 1.6 μm (ASH₂) respectively. The two resonances of ASH₁, λ_1 , corresponding to the transmittance peak of L_2 and λ_3 to the transmittance peak of L_1 were observed at wavelengths between 2.5 μm to 3.5 μm and the reflectance dip located between the two transmittance peak and denoted as λ_2 was between 2.8 μm and 3.2 μm . The denotation is shown in Figure 5.4. For ASH₂, λ_1 and λ_3 produced transmittance resonances between 5.5 μm and 7.0 μm and λ_2 between 5.8 μm to 6.3 μm . From the observation, when L_2 was increased the peak position of λ_2 and λ_3 were red-shifted. The distinct plasmonic resonances peaks varied linearly depending on the arm length. The experimental transmittance peaks were in good agreement with the simulated results that can be found in the previous chapter 4, section 4.6.5.

Amongst the various designs, ASH₁ with $L_1 = 800$ nm and $L_2 = 600$ nm produced a plasmonic resonance matching with the wavelength of the C-H bonds, as indicated in Figure 5.3, while for ASH₂ with $L_1 = 1.5 \mu\text{m}$ and $L_2 = 1.2 \mu\text{m}$ demonstrated close matches to the two double bond resonances. The measured transmittance spectra for these two ASHs presented a good match with the simulation spectra shown in Figure 5.4 and the scanning electron micrograph (SEM) images of a single unit and arrays are shown in Figure 5.5. Initially, the effect of the deposition of estrogen on the selected nanostructures was investigated by measuring E2. When deposited on the nanostructures, E2 crystallized on top of the resonators giving a thickness of

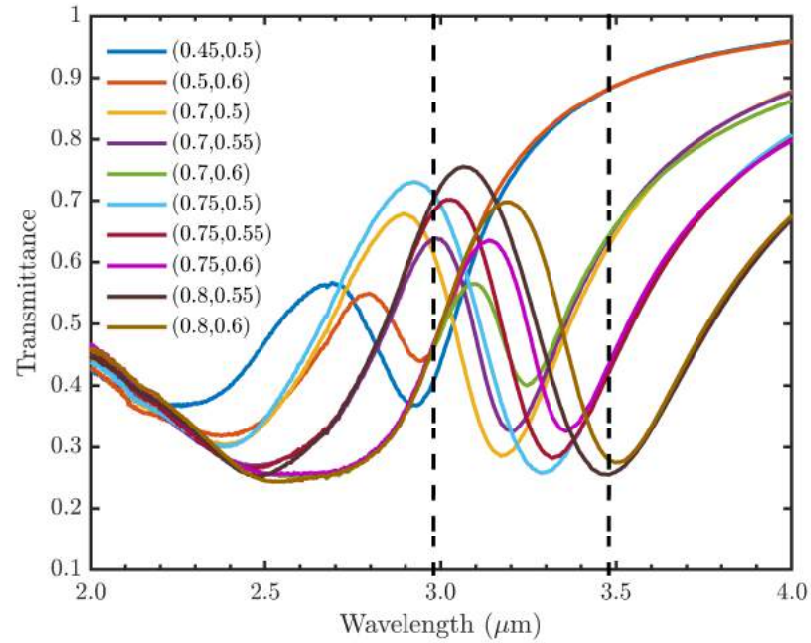
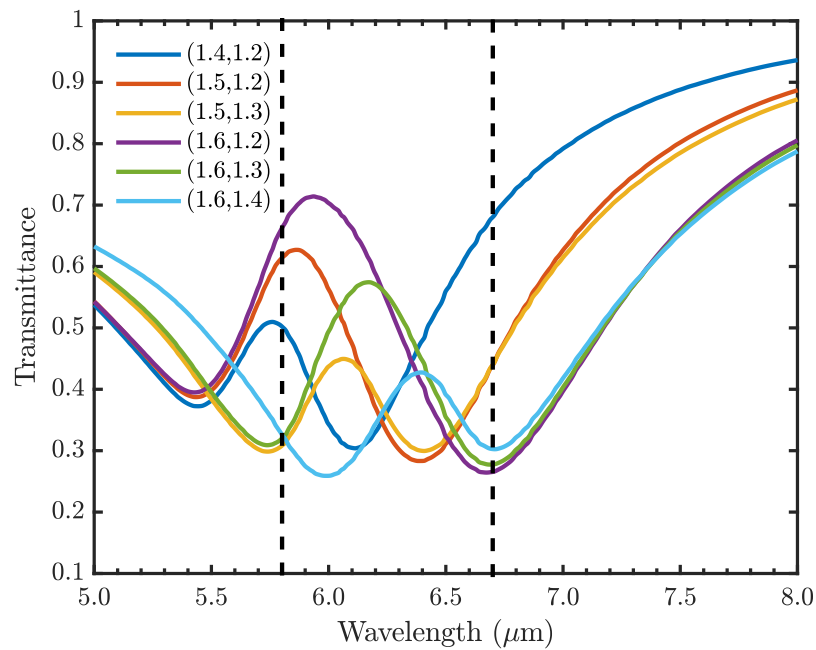
(a) ASH₁(b) ASH₂

Figure 5.3: Experimental results of tuning the arm-length of ASH₁ to produce resonance at 2 to 4 μm and ASH₂ at 5 to 8 μm. The black dashed lines are the highlighted area of the position of the molecular vibrations bond resonance.

approximately $100 \text{ nm} \pm 2 \text{ nm}$. Figure 5.6 shows the 2-D AFM images of ASH₁ arrays on the ZnSe substrate before (left image) and after deposition of 1 mg/ml concentration of E2 in EtOH (right image).

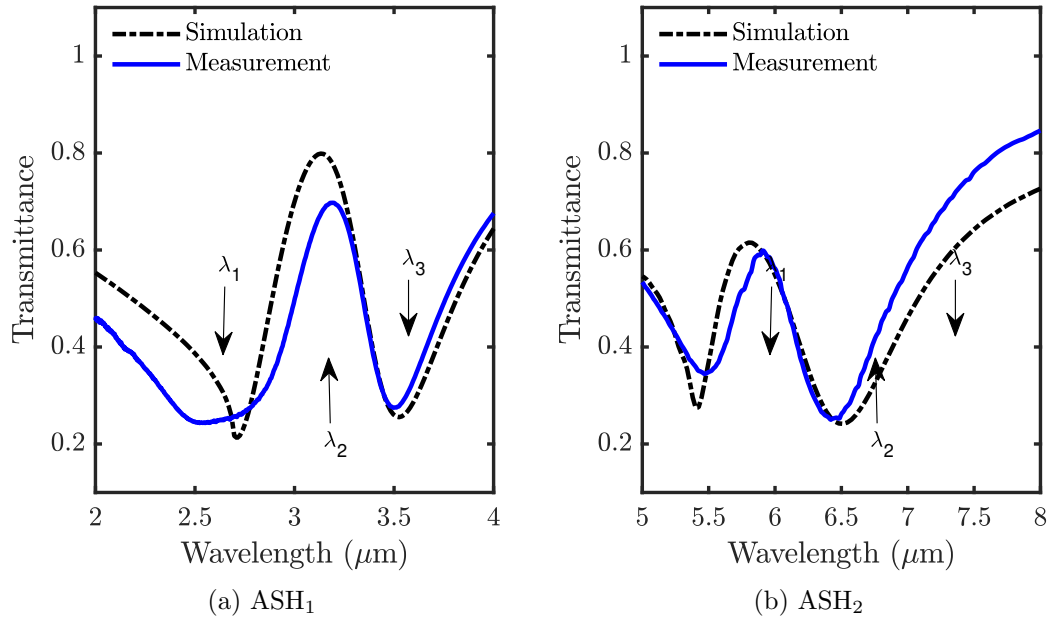


Figure 5.4: Simulated and measurement spectra of (a) ASH₁ and (b) ASH₂. The black dashed line is the simulated results obtained by Lumerical FDTD and the blue line is the measurement results using for corresponding ASH (L_1, L_2) - ASH₁ (800 nm, 600 nm) and ASH₂ (1.5 μm , 1.2 μm)

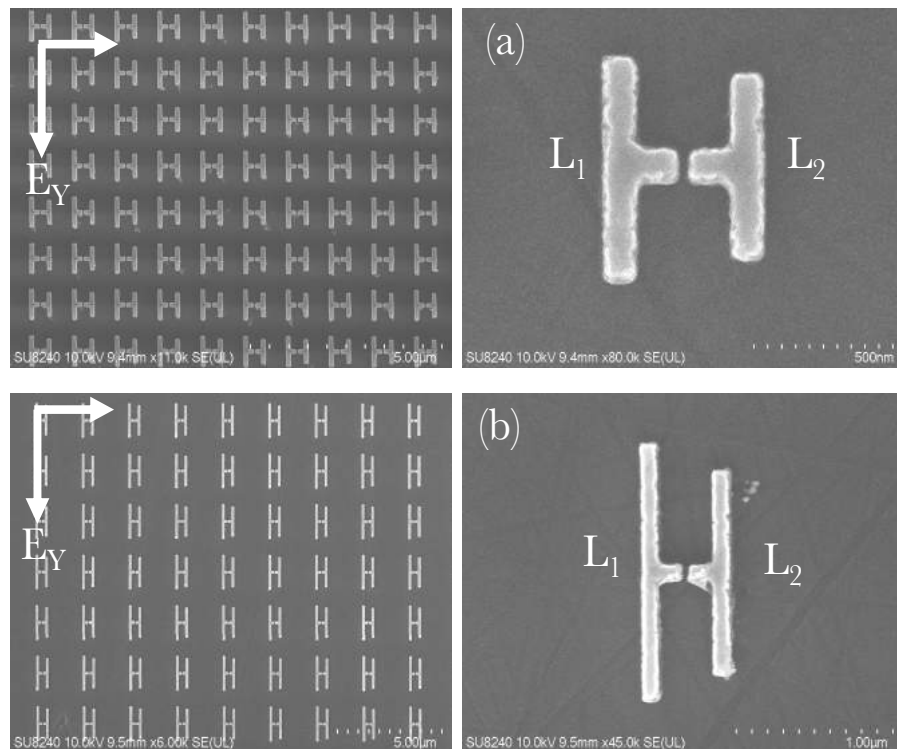


Figure 5.5: Scanning electron micrograph image of an array and one-unit cell of asymmetric split H (ASH) resonators with different sizes; (a) ASH₁ and (b) ASH₂.

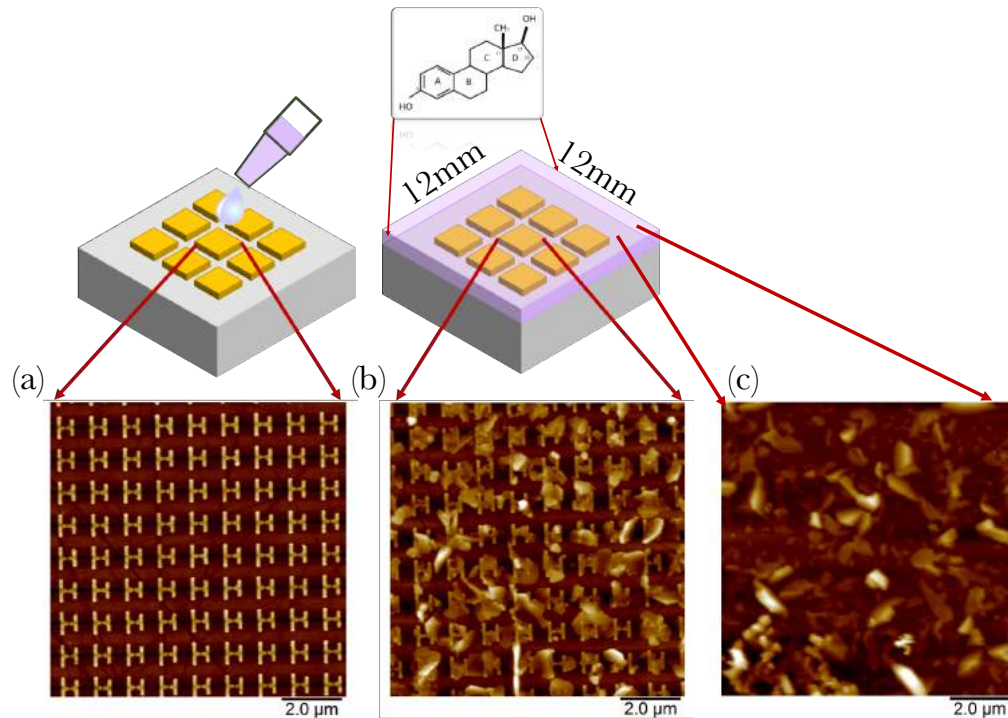


Figure 5.6: AFM images show 1 mg/ml concentration of E2 in EtOH (a) before and (b) after deposition on the ASH arrays (c) on the ZnSe substrate alone over an area of $10 \times 10 \mu\text{m}^2$. The E2 was crystallized on top of the sample.

As a result, the plasmonic resonances were distorted and a substantial red-shift was produced compared to the bare ASH. This is due to higher refractive index of E2 ($n \approx 1.55$) [25], [27] compared to refractive index of air ($n = 1$). As shown in Figure 5.7, the ASHs resonances shifted from their initial wavelengths; for ASH₁ from $3.27 \mu\text{m}$ to $3.47 \mu\text{m}$ and $3.50 \mu\text{m}$ to $3.71 \mu\text{m}$, and for ASH₂ from $5.92 \mu\text{m}$ to $6.27 \mu\text{m}$ and $6.49 \mu\text{m}$ to $6.79 \mu\text{m}$. Hence, the resonances shifted around 200 nm from the initial position for ASH₁ and around 300 nm for ASH₂. All the resonance shifts data are presented in Table 5.3. The spectral sensitivity, s (nm/RIU) of the nanostructures was calculated using the ratio between the changes in resonance peak position ($\Delta\lambda$) and the changes in the refractive index (Δn). The sensitivity of ASH₁ and ASH₂ was 363 nm/RIU and 636 nm/RIU respectively. Figure of merit (FOM) values also were calculated using the formula $FOM = s/FWHM$ to evaluate the quality of the plasmonic sensors. Thus, the maximum value of FOM, ASH₁ was $FOM_1 = 0.9$ RIU and ASH₂ was $FOM_2 = 1.3$ RIU. To evaluate the vibrational signal enhancement of estrogen on nanostructures, results were compared to E2 deposited on the bare ZnSe substrate as a reference signal (red line in Figure 5.7). The two peaks of C-H bond vibrations were matched with the reflection dips of ASH₁; while the three main C=C bonds peaks were matched with the reflection dips and transmittance peak of ASH₂ as shown at Figure 5.7.

To illustrate the enhancing power of matching the resonance of molecular bonds, the FTIR spectra of ASH_1 with different sizes of L_1 s are presented in Figure 5.8. The chosen arm lengths L_1 with the different dimensions of 700 nm, 750 nm and 800 nm, respectively, required to provide the transmittance resonance to be matched with the molecular bond resonance of C-H. The magnified spectrum over the wavelength range from 3.35 to 3.55 μm shows the different enhanced signals of the C-H bond vibration. The strongest signal enhancement is observed when the coupling between plasmonic resonance and the molecular vibrational was the closest; for C-H bonds this meant for an arm length L_1 of 800 nm. For the C-H bond vibration at 3.41 μm , the signal on bare ZnSe was 0.01% transmittance while it reached 5% when matched with reflection dip of the nanostructures. Because the same amount of E2 was deposited in both case, the enhancement factor is 500. At 750 nm the vibration of the bond peak matched with the transmittance peak and the peak intensity was reduced to 4%. At 700 nm the vibration bond peak appeared on the slope of the resonance and was further reduced to 2%. The coupling effect also attributes from the line width of the plasmonic resonance.

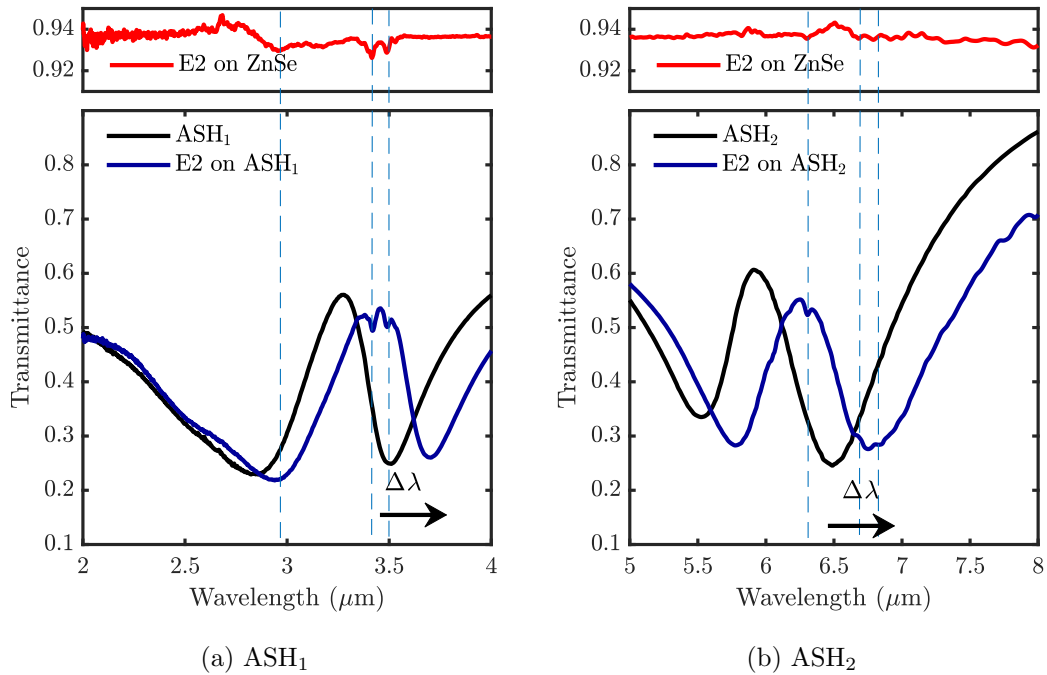


Figure 5.7: Top panel: The red line in both plots shows the deposition of E2 on the bare ZnSe substrate. Bottom panel: The figures showed the shift in the position of the transmittance resonance from (a) ASH_1 (b) ASH_2 sample before (black line) and after (blue line) the deposition of 1 mg/ml concentration of E2. The dashed blue line indicates the molecular bond vibration matched with the resonance shifted.

Table 5.3: Summary of the initial position of ASH_1 and ASH_2 and resonance shifted after deposition of E2 on the nanostructures. The sensitivity was calculated by spectral shift to the refractive index change. The value of refractive index change is $\Delta n \approx 1.55$.

ASH ₁					ASH ₂				
	Initial (μm)	Shift (μm)	λ (μm)	S		Initial (μm)	Shift (μm)	λ (μm)	S
λ_1	2.84	2.96	120	218	λ_1	5.54	5.79	250	454
λ_2	3.27	3.47	200	363	λ_2	5.92	6.27	350	636
λ_3	3.50	3.70	200	363	λ_3	6.49	6.79	300	545

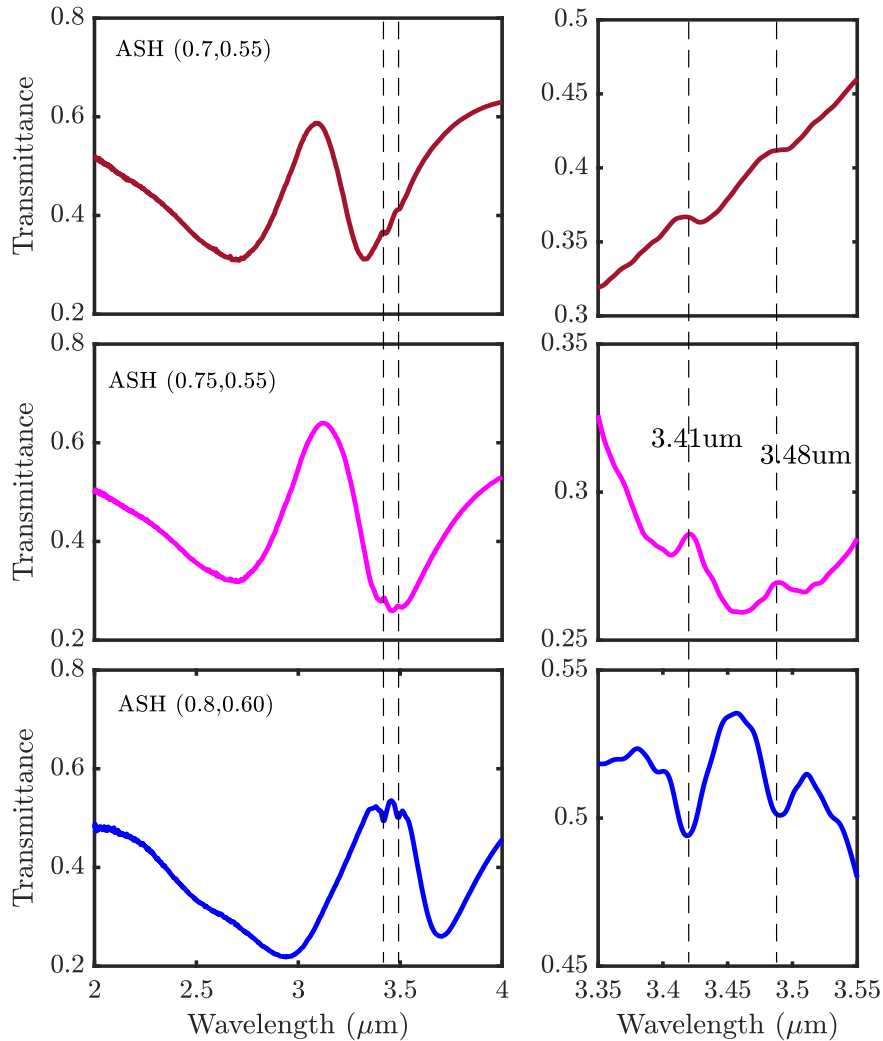


Figure 5.8: The transmittance spectra of three selected sizes of ASH as indicated covered with a thin layer of E2. The plot on the right is the magnified to the molecular vibration of the C-H bond. The black dashed line is referring to the C-H bond resonance at 3.41 μm and 3.48 μm .

The other three estrogenic hormones (E1, E3, and EE2) were also deposited on the nanostructures (Appendix A.2). The sizes of the nanostructures have been kept the same for these three estrogens. For EE2 the resonance effect was also clearly visible, while for E1 and E3 the enhancement did not occur strongly. This is might

be explained by the previous observation that crystallization of E2 and EE2 formed much more homogenous layers than E1 and E3. The crystal aggregation may be blocking the enhancement. Additionally, the O-H bonds were clearly resolved, even when the resonance was matched, which might be due to the O-H bonds producing a relatively broad absorption peak spectrum.

In order to quantitatively evaluate the experimental results, baseline correction was used to extract the peak intensity for various molecular vibrations. Baseline correction was carried out using the asymmetric least squares smoothing (AsLSS) algorithm MATLAB code were introduced by Eilers [28]. The calculations were performed by dividing the transmittance resonance of analyte (T_{ES}) with the corresponding baseline (T_{BASE}) and so that only the enhanced signal appears ($T_{REL} = T_{ES} / T_{BASE}$). The peak amplitude of the enhanced signal was calculated on the basis of a peak-to-peak value and Fano-resonant line-shape was produced. In Figure 5.9, the results for the baseline correction of each estrogen are presented for both ASH_1 and ASH_2 . The peaks for C-H molecular vibration of E1 and E3 were not enhanced by the plasmonic nanostructure. The results show that the molecular bond peak were enhanced by a factor up to 500 times compared to the bare ZnSe substrate.

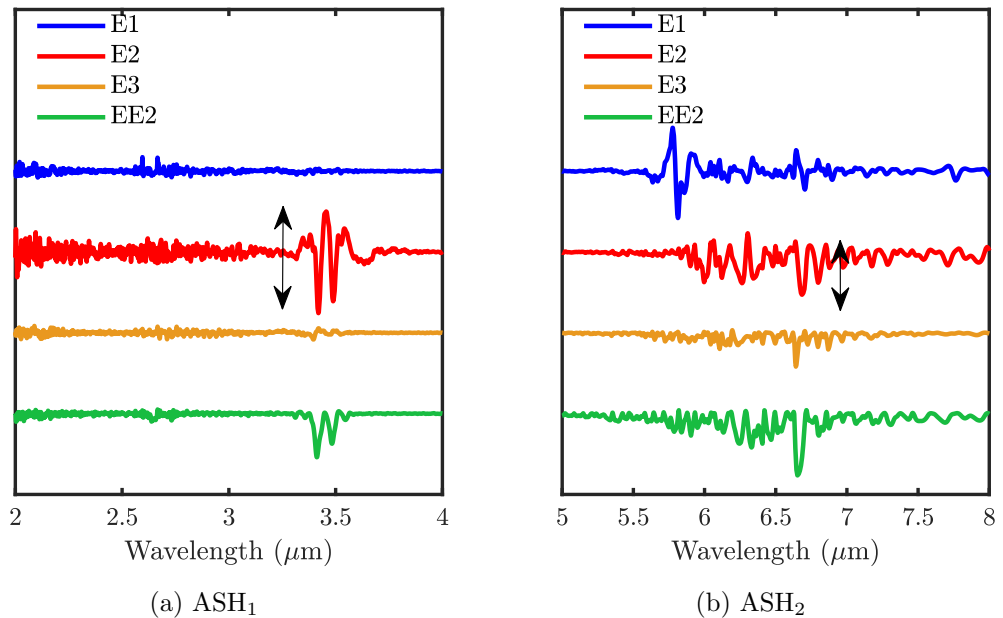


Figure 5.9: Shows the vibrational resonance after the baseline correction spectra of 1mg/ml solution of E1 (blue line), E2 (red line), E3 (orange line) and EE2 (green line) on ASH_1 and ASH_2 . The spectra are plots in stacked for better visibility. The black arrow indicated the peak-to-peak amplitude.

5.4.3 Detection of the mixture of two estrogenic hormones

The plasmonic nanostructures were coated with a thin layer of a mixture of E2 with one of the other hormones, E1, E3 and EE2 in absolute ethanol with a total estrogen concentration of 2 mg/ml as shown in Table 5.4 For mixtures of E2 and E1, E2:E1 ratios were also varied (Table 5.5). The estrogen mixtures was deposited as described previously on all the samples and was left to dry overnight. The significant chemical difference between E2 and E1 lies in a single bond, which is a C-OH in E2 and the C=O bond in E1 (see Table 5.2). To detect the molecular response of the mixtures of estrogen, the transmittance spectra were measured over an area of $380 \times 380 \mu\text{m}^2$ and the results are shown in Appendix Figure A.3 and Figure A.4. When the mixture of E2 and E1 was deposited on the nanostructures, a small feature could be observed from the transmittance resonance (Figure 5.10(a) and (b) in red lines) at a wavelength of around $5.79 \mu\text{m}$ as shown for ASH_2 in Figure 5.10(b), that matched the vibration of the C=O bond present in E1. The vibrational signal enhancement of estrogen deposited on nanostructure arrays could be quantified by comparison with the deposition of the estrogen mixtures on the bare ZnSe substrate (green line in Figure 5.10).

Table 5.4: Compositions of E2 - E1 mixtures with different ratios, diluted in absolute ethanol and having the same total concentration of 2mg/ml.

Mix	E2+E _x (mg)	EtOH (ml)	Ratio	E2 (g/l)	E _x (g/l)	E2 (mM)	E _x (mM)
E2+E1	4 + 4	4	50 : 50	1	1	3.67	3.69
E2+E3	4 + 4	4	50 : 50	1	1	3.67	3.45
E2+EE2	4 + 4	4	50 : 50	1	1	3.67	3.37

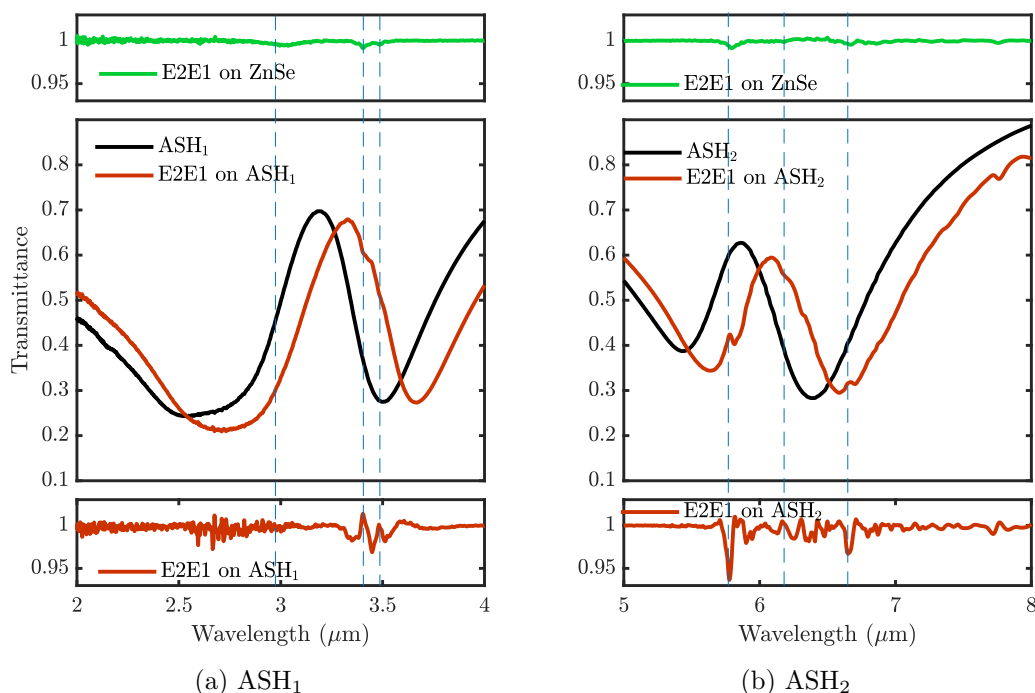


Figure 5.10: The upper panel: The vibrational transmittance spectrum of E2: E1 on the 1mm thickness ZnSe substrate alone measured with $380 \times 380 \mu\text{m}^2$. Middle panel: Plots transmittance resonances of shift in position (a) ASH_1 and (b) ASH_2 before (black colour) and after coated (red line) with the mixtures of E2 and E1 (50:50). Bottom panel: show the vibrational resonances after the baseline correction in the fingerprints of O-H, C-H, C=O and C=C bonds. The position of the respective vibrational resonances are shown with the blue dashed lines.

Figure 5.11, shows the comparison of the signals after baseline correction of the spectra of the mixture of E2 to E1 (green line), E2 to E3 (olive line) and E2 to EE2 (purple line). The peak that appears between 2.50 to 3.00 μm is the ripple from H_2O vapour that is present in the atmosphere. The molecular bond resonance of O-H and $\text{C}\equiv\text{C}$ -H fell on the slope of the plasmonic resonance and could hardly to be seen even after baseline correction. After baseline correction, the peak intensities of 3.1%, 3.29% and 3.57% for the CH_2 respectively can be easily identified (Figure 5.12). The peak intensity was similar for each mixture due to the CH bond existing in all the estrogens. The CH_3 peak intensity was much lower than the peak intensity of CH_2 at 2.7%, 2.45% and 3.34% respectively due to the weaker signals from CH_3 . Comparison of the peak intensities in the various mixtures showed that by using ASH_1 and ASH_2 , the different estrogens could be identified and their molar fractions could potentially be determined particularly for E1 and E2 has the peak of C=O, distinctive of E1, was enhanced (Figure 5.14).

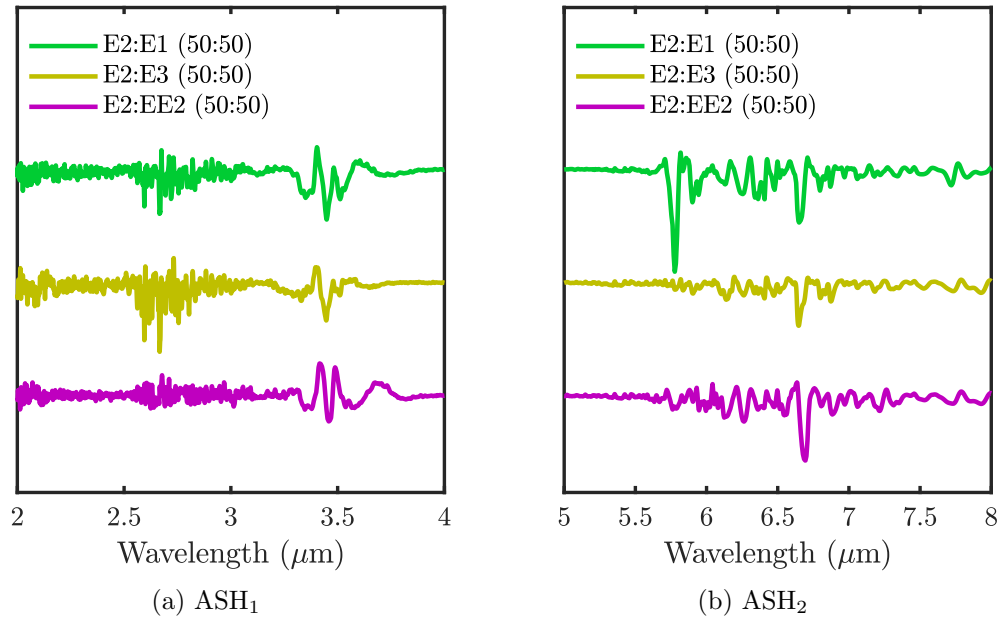


Figure 5.11: Baseline correction spectra of the mixtures E2 with E1 (green line), E3 (olive line) and EE2 (purple line). The peak amplitude of the enhanced signal was calculated based on a peak to peak value. The peak position agrees well with the deposition on the ZnSe substrate alone. Stacked plots were used for the purpose of better visibility.

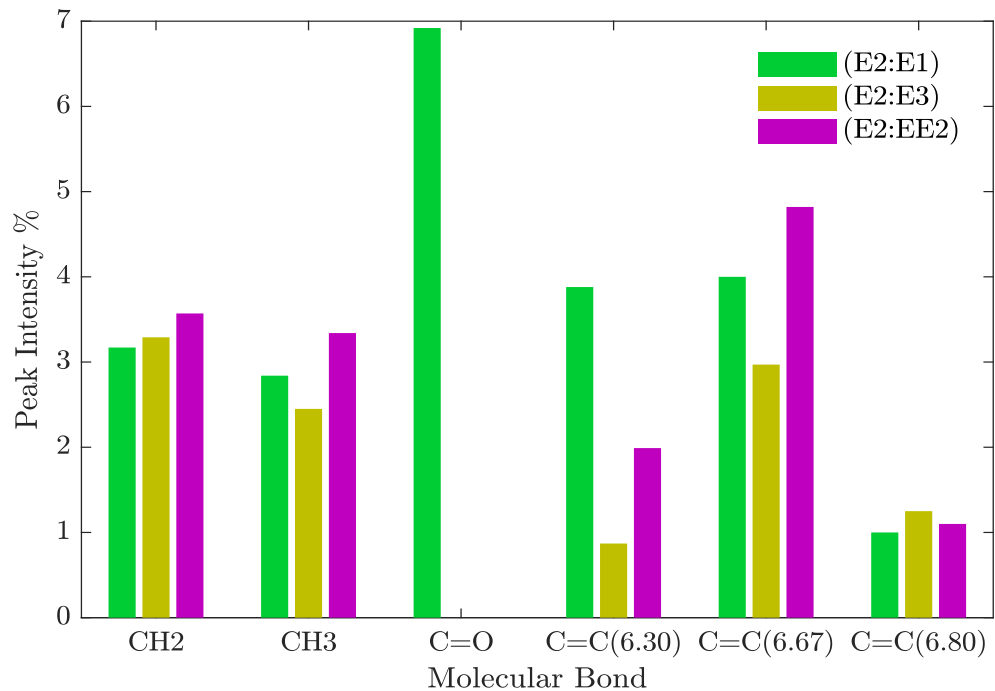


Figure 5.12: Determination of percentage peak intensity of each of the molecular bond resonances C-H, C=O and C=C in three different mixtures of E2 with E1, E3, and EE2.

Table 5.5 indicate the different ratios of mixtures of E2 to E1 with a total concentration of 2mg/ml that were deposited on the nanostructures (Appendix A.4). The resonance shift In the E2:E1 mixtures of (25:75) and (0:100), the resonances exhibits small shifts because the total amount of mole of estrogen does not vary much. The resonance shifts of all E2:E1 mixtures are approximately 180, 210, 80, 168 and 30 nm. The peak intensity of the C=O bond increased from 6.9%, 7.5%, 8.4% and 9.7% as the ratio of E1 increased (Figure 5.13). The peak intensity of the C=C bond remains nearly constant for each ratio, this was expected because both estrogens have the same C=C bonds. Quantitatively, the C=C bond peak intensity can, therefore, be used to indicate the total amount of the estrogen. It is also noteworthy that the shape of the C-H bond at 3.41 μm and 3.49 μm slowly change depending on the ratios of E1 and E2. The peak of C-H bond for E1 appeared at 3.40 μm and 3.49 μm and E2 is at 3.41 μm and 3.48 μm . When the amount of E2 was reduced the peak at 3.41 μm was also reduced but the peak at 3.49 μm increased due to the increase of E1 as shown in Figure 5.15(a). Additionally, the contribution of both type of estrogen could be quantitatively separated out as shown in Figure 5.14. Also, Figure A.6 in the appendix shows the deposition of the estrogen on one sample in three different areas with the same sizes of ASH. The sample was systematically measured and found the peak position is consistent in different areas.

Table 5.5: Table of the mixtures between E2 and E1 with different ratios diluted in the absolute ethanol giving the same total concentration of 2mg/ml.

E2+E1 (mg)	<i>EtOH</i> (ml)	Ratio	E2 (mg/ml)	E1 (mg/ml)	E2 (mM)	E1 (mM)
4 + 4	4	50 : 50	1	1	3.67	3.69
3 + 5	4	37.5 : 62.7	0.75	1.25	2.75	4.62
2 + 6	4	25 : 75	0.5	1.5	1.83	5.55
1 + 7	4	12.5 : 87.5	0.25	1.75	0.92	6.47
0 + 8	4	0 : 100	0	1	0	7.39

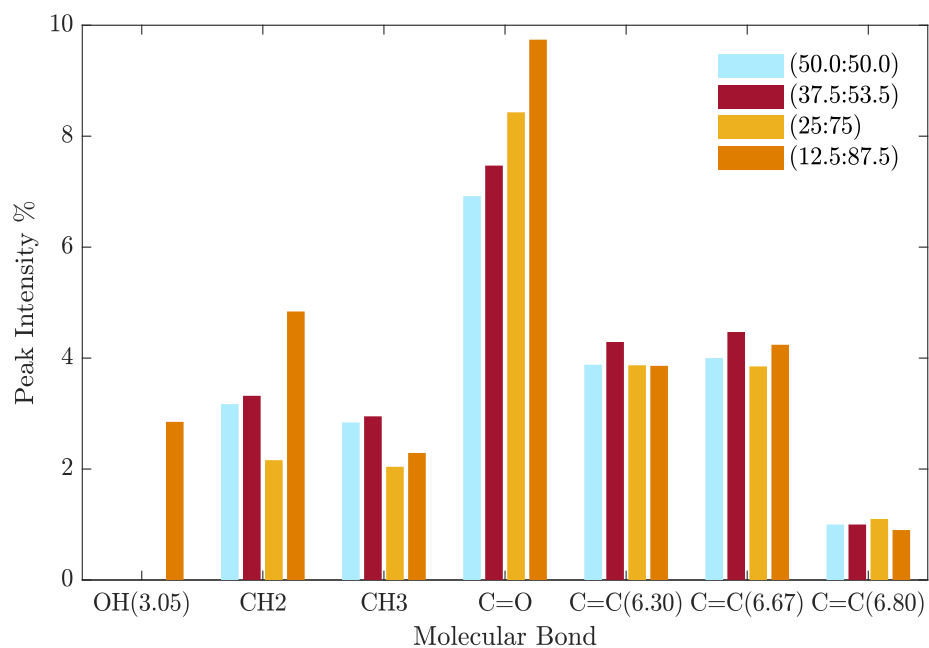


Figure 5.13: Determination of percentage peak intensity of each molecular bond resonances C-H, C=O and C=C in three different ratios of E2 to E1.

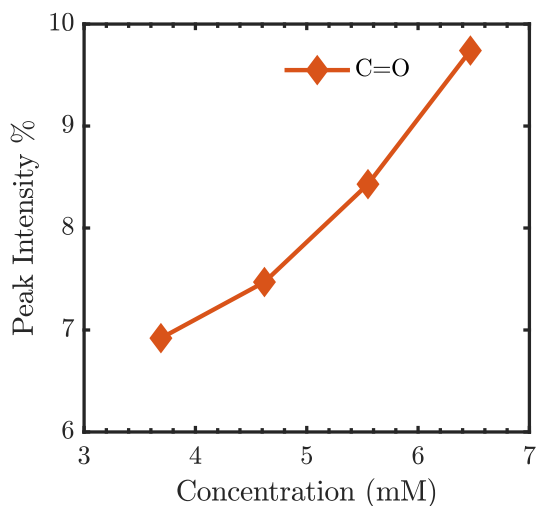


Figure 5.14: The peak intensity after baseline correction of the C=O group as a function of E1 concentration. The peaks are linearly correlated to the concentration of E1.

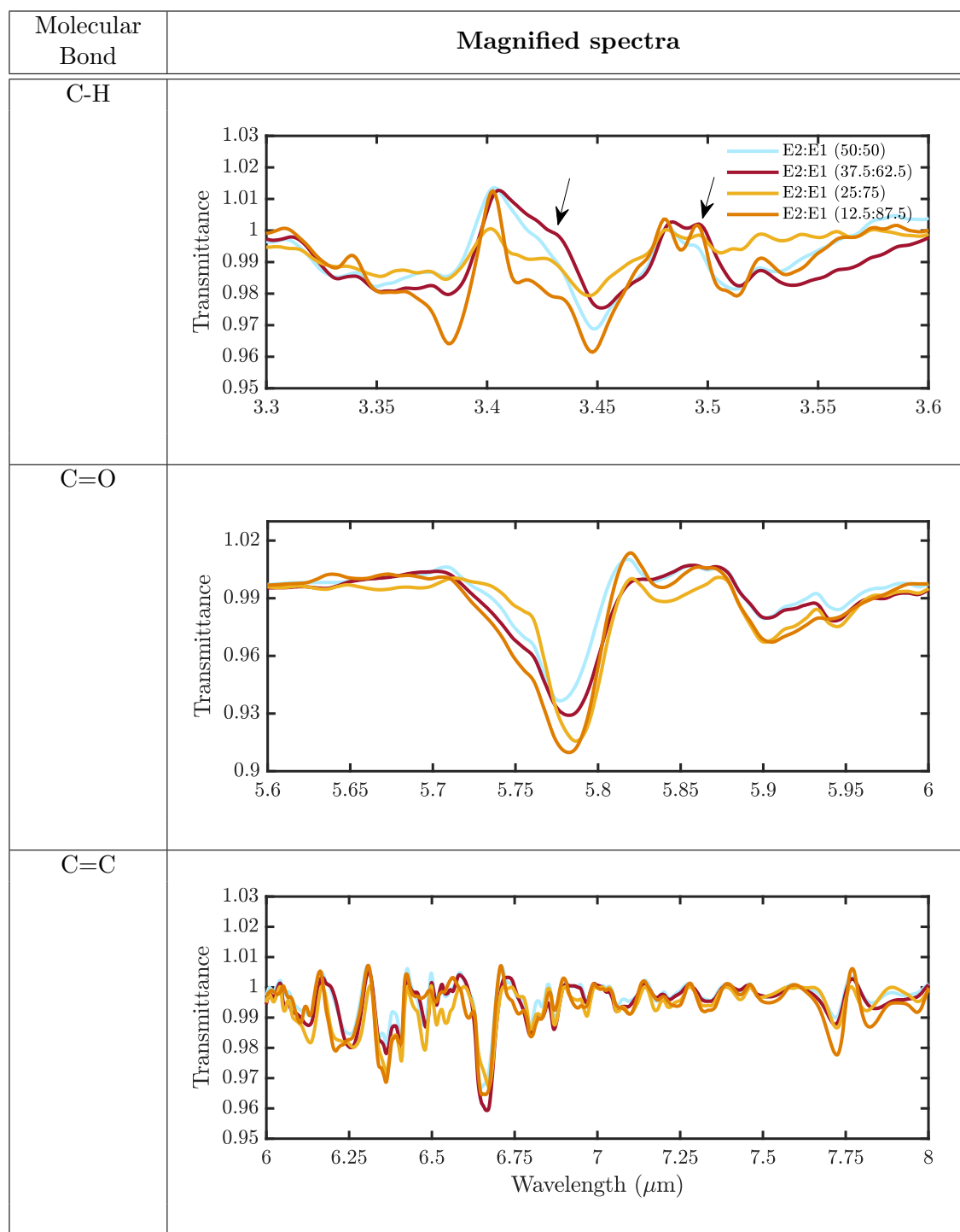


Figure 5.15: Fingerprint signal intensities for mixtures of two estrogens E2: E1 on ASH arrays showing transmittance resonances extracted after baseline correction. The C=O molecular peak intensity increases directly with the amount of E1 in the mixtures. The double-bond resonance peak occurs at the same peak intensity, in order to indicate the total concentration of the mixtures of estrogens.

5.5 Conclusions

In conclusion, the geometry of the asymmetric split-H resonators has been tuned and varied which can be utilized to enhance the molecular C-H, C=O and C=C bond resonances of the estrogenic hormones. The plasmonic resonance was red-shifted towards longer wavelengths with the deposition of organic materials on the nanostructures. From these observation, the molecular bond resonances are typically five hundred times larger, are easily visible and enables differentiation of various estrogens, as compared with those deposited on bare substrates. The used of plasmonic resonant coupling techniques enables identifications of the common (O-H, C-H and C=C bonds) and different (C=O bonds) molecular bond resonances for the two estrogen molecules in the mid-infrared wavelength range from 2 to 8 μm . The ASH nanostructures can be flexibly designed over this broad wavelength range and can be tuned to enhance the differences between the different estrogens and aid quantitative detection.

References

- [1] M. Adeel, X. Song, Y. Wang, D. Francis, and Y. Yang, “Environmental impact of estrogens on human, animal and plant life: A critical review,” *Environment International*, vol. 99, pp. 107–119, Feb. 2017 (cit. on pp. 77, 78).
- [2] A. Wise, K. O’Brien, and T. Woodruff, “Are Oral Contraceptives a Significant Contributor to the Estrogenicity of Drinking Water? †,” *Environmental Science & Technology*, vol. 45, no. 1, pp. 51–60, Jan. 2011 (cit. on p. 77).
- [3] H. Chang, Y. Wan, S. Wu, Z. Fan, and J. Hu, “Occurrence of androgens and progestogens in wastewater treatment plants and receiving river waters: Comparison to estrogens,” *Water Research*, vol. 45, no. 2, pp. 732–740, Jan. 2011 (cit. on p. 77).
- [4] A. J. Murk, J. Legler, M. M. H. Van Lipzig, J. H. N. Meerman, A. C. Belfroid, A. Spenkeliink, B. Van der Burg, G. B. J. Rijs, and D. Vethaak, “Detection of estrogenic potency in wastewater and surface water with three in vitro bioassays,” *Environmental Toxicology and Chemistry*, vol. 21, no. 1, pp. 16–23, Jan. 2002 (cit. on pp. 77, 78).
- [5] H. Hamid and C. Eskicioglu, *Fate of estrogenic hormones in wastewater and sludge treatment: A review of properties and analytical detection techniques in sludge matrix*, 2012 (cit. on p. 78).
- [6] M. Velicu and R. Suri, “Presence of steroid hormones and antibiotics in surface water of agricultural, suburban and mixed-use areas,” *Environmental Monitoring and Assessment*, vol. 154, no. 1-4, pp. 349–359, Jul. 2009 (cit. on p. 78).
- [7] European Commission, *Introduction to the new EU Water Framework Directive - Environment*, 2015. [Online]. Available: http://ec.europa.eu/environment/water/water-framework/info/intro%7B%5C_%7Den.htm (visited on 02/17/2019) (cit. on p. 78).
- [8] B. J. Sanghavi, J. A. Moore, J. L. Chávez, J. A. Hagen, N. Kelley-Loughnane, C. F. Chou, and N. S. Swami, “Aptamer-functionalized nanoparticles for surface immobilization-free electrochemical detection of cortisol in a microfluidic device,” *Biosensors and Bioelectronics*, vol. 78, pp. 244–252, Apr. 2016 (cit. on p. 78).
- [9] F. Long, M. He, A. N. Zhu, and H. C. Shi, “Portable optical immunosensor for highly sensitive detection of microcystin-LR in water samples,” *Biosensors and Bioelectronics*, vol. 24, no. 8, pp. 2346–2351, 2009 (cit. on p. 78).

- [10] W. J. Backe, “An Ultrasensitive (Parts-Per-Quadrillion) and SPE-Free Method for the Quantitative Analysis of Estrogens in Surface Water,” *Environmental Science and Technology*, vol. 49, no. 24, pp. 14 311–14 318, Dec. 2015 (cit. on p. 78).
- [11] Y. Dai and C. Liu, “Detection of 17 β -Estradiol in Environmental Samples and for Health Care Using a Single-Use, Cost-Effective Biosensor Based on Differential Pulse Voltammetry (DPV),” *Biosensors*, vol. 7, no. 2, p. 15, Mar. 2017 (cit. on p. 78).
- [12] C.-H. Huang and D. L. Sedlak, “Analysis of estrogenic hormones in municipal wastewater effluent and surface water using enzyme-linked immunosorbent assay and gas chromatography/tandem mass spectrometry,” *Environmental Toxicology and Chemistry*, vol. 20, no. 1, pp. 133–139, Jan. 2001 (cit. on p. 78).
- [13] O. A. Alsager, S. Kumar, B. Zhu, J. Travas-Sejdic, K. P. McNatty, and J. M. Hodgkiss, “Ultrasensitive Colorimetric Detection of 17 β -Estradiol: The Effect of Shortening DNA Aptamer Sequences,” *Analytical Chemistry*, vol. 87, no. 8, pp. 4201–4209, Apr. 2015 (cit. on p. 78).
- [14] *Handbook of Hormones*. Elsevier, 2016. DOI: [10.1016/C2013-0-15395-0](https://doi.org/10.1016/C2013-0-15395-0) (cit. on p. 78).
- [15] E. V. Jensen, “Estrogenic Hormones,” in *Encyclopedia of Cancer*, Berlin, Heidelberg: Springer Berlin Heidelberg, 2011, pp. 1331–1333 (cit. on p. 78).
- [16] A. Nezami, R. Nosrati, B. Golichenari, R. Rezaee, G. I. Chatzidakis, A. M. Tsatsakis, and G. Karimi, “Nanomaterial-based aptasensors and bioaffinity sensors for quantitative detection of 17 β -estradiol,” *TrAC Trends in Analytical Chemistry*, vol. 94, pp. 95–105, Sep. 2017 (cit. on p. 78).
- [17] National Center for Biotechnology Information, *Estradiol*, 2004. [Online]. Available: <https://pubchem.ncbi.nlm.nih.gov/compound/5757> (visited on 05/03/2017) (cit. on pp. 79, 82).
- [18] —, *Estrone*, 2004. [Online]. Available: <https://pubchem.ncbi.nlm.nih.gov/compound/5870> (visited on 05/03/2017) (cit. on pp. 79, 82).
- [19] —, *Estriol*, 2004. [Online]. Available: <https://pubchem.ncbi.nlm.nih.gov/compound/5756> (visited on 05/03/2017) (cit. on pp. 79, 82).
- [20] —, *Ethinyl Estradiol*, 2004. [Online]. Available: <https://pubchem.ncbi.nlm.nih.gov/compound/5991> (visited on 05/03/2017) (cit. on pp. 79, 82).
- [21] Crystran Ltd., “Zinc Selenide (ZnSe) Optical Material,” pp. 3–4, 2018 (cit. on pp. 80, 81).

- [22] J. Paul, G. J. Sharp, B. Lahiri, R. M. De La Rue, and N. P. Johnson, “Simulation and experimental responses of the asymmetric split ring resonators (A-SRRs) for sensing applications in the mid-infrared region,” in *2015 9th International Congress on Advanced Electromagnetic Materials in Microwaves and Optics (METAMATERIALS)*, IEEE, Sep. 2015, pp. 469–471 (cit. on p. 80).
- [23] *Lumerical Solutions*, 2015. [Online]. Available: <https://www.lumerical.com/tcad-products/fdtd/> (cit. on p. 81).
- [24] E. D. Palik, *Palik, Handbook of Optical Constants of Solids, Vol.2*. 1991, vol. 2 (cit. on p. 81).
- [25] I. G. Mbomson, S. G. McMeekin, B. Lahiri, R. M. De La Rue, and N. P. Johnson, “Gold asymmetric split ring resonators (A-SRRs) for nano sensing of estradiol,” in *SPIE Photonics Europe*, A. D. Boardman, N. P. Johnson, K. F. MacDonald, and E. Özbay, Eds., International Society for Optics and Photonics, May 2014, 91251O (cit. on pp. 81, 88).
- [26] R. C. Gore, “Infrared Spectroscopy,” *Analytical Chemistry*, vol. 30, no. 4, pp. 570–579, Apr. 1958 (cit. on p. 82).
- [27] I. G. Mbomson, S. Tabor, B. Lahiri, G. J. Sharp, S. G. McMeekin, R. M. De La Rue, and N. P. Johnson, “Asymmetric split H-shape nanoantennas for molecular sensing,” *Biomedical Optics Express*, vol. 8, no. 1, p. 395, Jan. 2017 (cit. on p. 88).
- [28] P. H. Eilers, *A perfect smoother*, Jul. 2003. [Online]. Available: <http://pubs.acs.org/doi/abs/10.1021/ac034173t> (cit. on p. 91).

Chapter 6

Aptamers as bio-recognition element for plasmonic estrogenic hormone biosensor

6.1 Abstract

Optical sensors based on metamaterial nanostructures allow new developments by combining the elements of biochemistry, nanotechnology, physics, and electronics. Due to their high-sensitivity and flexibility, array metasurfaces have been widely employed as label-free optical sensors for organic compounds and eventually used for rapid environmental analysis. A sensing platform for the specific detection of 17β -Estradiol (E2) using an array of asymmetric split-H (ASH) resonators have been developed. The surface functionalization of an ASH with specific thiol-terminated aptamers for the targeted analyte was described in chapter. Different concentrations of E2 ranging from 1 nM to 100 μ M were deposited on the geometries of ASH resonators, labelled as ASH₁ and ASH₂, fabricated on a zinc selenide (ZnSe) substrate. These various efforts have demonstrated novel efficient approaches for SEIRA and RI sensing for estrogenic hormones.

6.2 Aptamer-based biosensor

Several recent examples of the development of environmental aptasensors, biosensors that use aptamers as a bio-recognition element, have been presented in the literature. They have been coupled with electrochemical, optical fibres, fluorescence, colourimetric and gold nanoparticles detection methods with sensitivity as low as fM [1]–[3]. Aptamers can bind to many types of analytes such as proteins, adenosines, toxins, thrombin and have been used for detection in tap water, lake water, wastewater

and in the urine. Hou *et al.* produced aptasensors based on cantilever array sensors to detect the contamination of food products and pharmaceutical preparations with a detection limit of 0.2 nanoMole (nM). The detection technique was based on a microfabricated cantilever array. In this case, aptamers specifically bind with the oxytetracycline (OCT) by mechanical bending of the cantilever. This is generated by a change in the surface stress on the functionalized cantilever surface compared to reference cantilevers (functionalized with 6-mercapto-1-hexanol) [4]. The advantage of using cantilever sensors is that the molecular recognition can be directly and specifically transduced into mechanical responses.

17 β -Estradiol (E2) and 17 α -ethynylestradiol (EE2) have been widely detected in natural water sources, often at high concentrations. ELISAs (enzyme-linked immunosorbent assays) that use antibody as recognition elements are sensitive enough to detect estrogen in natural waters but are still expensive and suffer with interferences of other components [5]. To provide a sensitive biosensor platform for specific detection with low-cost synthesis, aptamers can be used as an alternative to antibodies. Amongst the published aptasensors, only a limited number presents binding to estrogenic hormones. In 2007, Kim *et al.* developed an electrochemical aptamer-based assay for E2 using a DNA aptamer immobilized on a gold electrode chip [6]. The E2 binding DNA aptamer was selected by Kim *et al.* using the SELEX process from a starting library containing around 7.2×10^{14} DNA molecules (shown in Chapter 2: Figure 2.9). The DNA aptamer was attached using immobilization on streptavidin modified gold surface via the avidin-biotin interaction. Several concentrations from 0.01 nM to 100 nM of the E2 were tested on the 1 nM DNA aptamer immobilized on the gold electrode surface and the lowest concentration detected was 0.13 μ M.

Later, Yildirim *et al.* (2013) developed a portable and all-fibre platform for detection of E2 in wastewater using a fluorescent-labelled DNA aptamer [3]. The aptamer can competitively bind with the β -estradiol 6-(O-carboxy-methyl)oxime-BSA complex immobilized on the optical fibre sensor surface and E2 in solution. The sensor was reported to have low fluorescent response signals in the wastewater sample when it bound with higher concentrations of E2. The sensing process took less than 10 min with a detection limit of 2.1 nM (0.6 ng mL^{-1}) on a basis of the dose-response curve and the signal to noise ratio. In 2014, Huang *et al.* reported a new electrochemical aptasensor by immobilizing the aptamer on the surface of gold nanoparticles and vanadium disulfide (VS₂) nanoflowers modified with a glassy carbon electrode (GCE) [7]. The VS₂ nanoflower surface provided a more active surface and exhibited signal amplification for E2 detection. Concentrations of E2 in

the range of 0.01 – 10 nM were analysed, and the detection limit was 1.0 pM.

Later, Fan *et al.* developed a photochemical (PEC) sensor, coupling photoirradiation with electrochemical detection, using an aptamer as bio-recognition element immobilize onto CdSe nanoparticles-modified TiO₂ nanotubes array [8]. The PEC aptasensor successfully detected estradiol in environmental water samples and had a reported detection limit of 33 fM; lower than any other reported previously. Akki *et al.* (2015) tested four new DNA aptamers (E2Apt1, E2Apt2, EEApt1, and EEApt2) for E2 and EE2 [9]. E2Apt1 and E2Apt2 strongly bound to E2 followed by estrone (E1) compared to EE2. EEApt1 bound to EE2 with a 53-fold higher selectivity over E2 or E1 and the EEApt2 did not discriminate between the three estrogens E1, E2 and EE2. According to these studies, a new aptamer was 74-fold more sensitive for E2 as compared to the previous study before and did not lose the sensitivity or selectivity when tested in natural water. In other studies by Alsager *et al.*, aptamers were shortened to 35-mer and 22-mer and it was found to improve the sensitivity of colourimetric assays using gold nanoparticles coated with aptamers for E2 detection in water and urine samples [2]. The studies started with investigating the detection using 75-mer long aptamers before shortening to 35-mer and 22-mer. The resulting 35-mer had improved affinity for E2 and a detection limit of 200 pM was found in this study.

An aptamer-based surface-enhanced Raman spectroscopic sensor developed by Liu *et al.* successfully detected E2 with high specificity and selectivity in complex environmental waste [10]. The system was based on gold-silver core-shell nanoparticles (Au@Ag CS NPs) functionalized with 4-mercaptobenzoic acid (4-MBA). The sensor detection limit was 0.05 pM. The interference of dibutyl phthalate (DBP) and bovine serum albumin (BSA) were tested in the system and found that there was no interference on the E2 response. This showed that the aptamer had a strong binding affinity with E2. More recently, Liu *et al.* (2019) [11] proposed an electrochemical label-free aptasensor to detect E2 using a signal amplification of bi-functional graphene. The graphene is not only used to adsorb the E2 binding but also used as a recognition element to E2. The work shows the aptamer-graphene (Apt-G) complex taking advantages of excellent electron transfer and high sensitivity of E2 were obtained and the detection limit was 50 fM.

In the previous chapter, asymmetric split-H resonators (ASH) were tuned to be matched with the molecular bonds of four estrogen compounds in the mid-infrared range. In this chapter, the use of ASH as sensor surface has been investigated and the ASHs were functionalised with thiol-terminated aptamers. The aptamer denoted

as APT, the single-stranded of deoxyribonucleic acid (DNA) isolated by Kim *et al.* [6] was used as the bio-recognition element to specifically binds to the targeted molecule of 17 β -estradiol (E2). 6-Mercapto-1-hexanol was used as a blocking agent to prevent non-specific binding on the ASH gold surface. The same principle is used in this chapter, where the ASH shows the have efficient approaches for RI sensing.

6.3 Materials and Methods

6.3.1 Chemicals

DNA Aptamer: Single-stranded DNA aptamers specific to E2 was synthesized and purified from Eurofins Genomics with the following DNA sequences:

Single stranded DNA Sequence: 5'Thiol-C6-GCT-TCC-AGC-TTA-TTG-AAT-TAC-ACG-CAG-AGG-GTA-GCG-GCT-CTG-CGC-ATT-CAA-TTG-CTG-CGC-GCT-GAA-GCG-CGG-AAG-C-3'

It has been isolated by SELEX process from a random ssDNA library by Y.S. Kim *et al* [6]. The DNA aptamer strand is 76-mer long and 23 kDa. The 5' end was modified with a thiol linkage for sulphur gold (S-Au) bonding on the gold surface and the other 3' end was kept label-free.

Tris (hydroxymethyl)-aminomethane (Tris) base was purchased from Fisher Scientific, other reagents; magnesium chlorides (MgCl₂), sodium chloride (NaCl) and hydrochloric acid (HCl) were purchased from Sigma-Aldrich.

An aptamer stock solution was prepared in 20 mM Tris-HCl buffer solution contained with 1 mM HCl, 0.1 M NaCl, 5 mM MgCl₂ at pH of 7.3. The buffer was prepared as follow: 1.2114 g Tris base was dissolved in 500 ml of deionized water with 18 M Ω , Milli-Q using a magnetic stirrer. Then, the pH of Tris was adjusted to 7.3 by slowly adding HCl from a 1M solution, then 2.922 g of NaCl and 0.5083 g of MgCl₂ was added to the solution. The solution was autoclaved before further used. The different concentrations of aptamers were prepared in the Tris-HCl buffer stored at -20°C.

Blocking agent: The blocking agent, 6-mercapto-1-hexanol (MCH) (a short alkanethiol) with 97% purity was purchased from Sigma-Aldrich. 20 μ l of MCH was dissolved in a mixture of 10 mM phosphate buffer solution (PBS) with 10 mM MgCl₂. PBS was purchased from Fisher scientific in a tablet. A tablet of PBS was

dissolved with 100 ml of deionized water and 0.2033 g of MgCl_2 were added. In all experiments, the concentration of MCH was constant at 14.6 μM .

17 β -Estradiol preparation: The material of E2 in this chapter is the same as in the previous chapter. 15 mg of E2 powder was dissolved with 1ml of absolute ethanol (99.9%) in high concentration, 15 mg/ml or 55 mM and diluted using deionized water with 18m Ω , Milli-Q for six different concentrations: 0.27 ng/ml, 2.7 ng/ml, 27.4 ng/ml, 272 ng/ml, 2.72 $\mu\text{g}/\text{ml}$ and 273.4 $\mu\text{g}/\text{ml}$ equivalent to 1 nM, 10 nM, 100 nM, 1 μM , 10 μM , 100 μM .

6.3.2 Fabrication, measurements and characterization

The fabrication and measurement methods used in this chapter were as described in previous chapter. The samples were fabricated using electron beam lithography on the ZnSe substrate and the measurement was taken using FTIR. The measurement was taken in four stages directly after the sample was rinsed; the first spectra were taken from the bare ASH nanostructures (without any molecules), the second measurement on the aptamer (APT) functionalised ASH nanostructures, the third measurement on the ASH with aptamer and blocking agent (APT+MCH), and the final measurement is taken on ASH with aptamer, blocking agent and 17 β -estradiol (APT+MCH+E2).

Atomic force microscopy: Three dimensional and two-dimensional images of the characterization of the sensor surface were obtained using atomic force microscopy (AFM; Dimension Icon by Bruker). Morphologies of the Au were evaluated using ScanAsyst mode (PeakForce tapping mode) that enable to create high-resolution AFM images. The images were taken over areas of 10 μm x 10 μm and 1 μm x 1 μm with 512 scans. The height of the nanostructures was 104 nm.

6.3.3 Surface functionalization of the gold nanostructures surface

The surface functionalization techniques were adapted from protocols established in Dr Nathalie Lidgi-Guigui's laboratory [12] and the training was carried out in that lab at Université Paris 13, IUT de Bobigny during Mobility visit. The techniques were optimised there on gold nanoparticles samples were fabricated by A. Li Bassi *et al.* from Polytechnico di Milano. This work, beyond the scope of this thesis, will be the subject of a peer-review article under preparation.

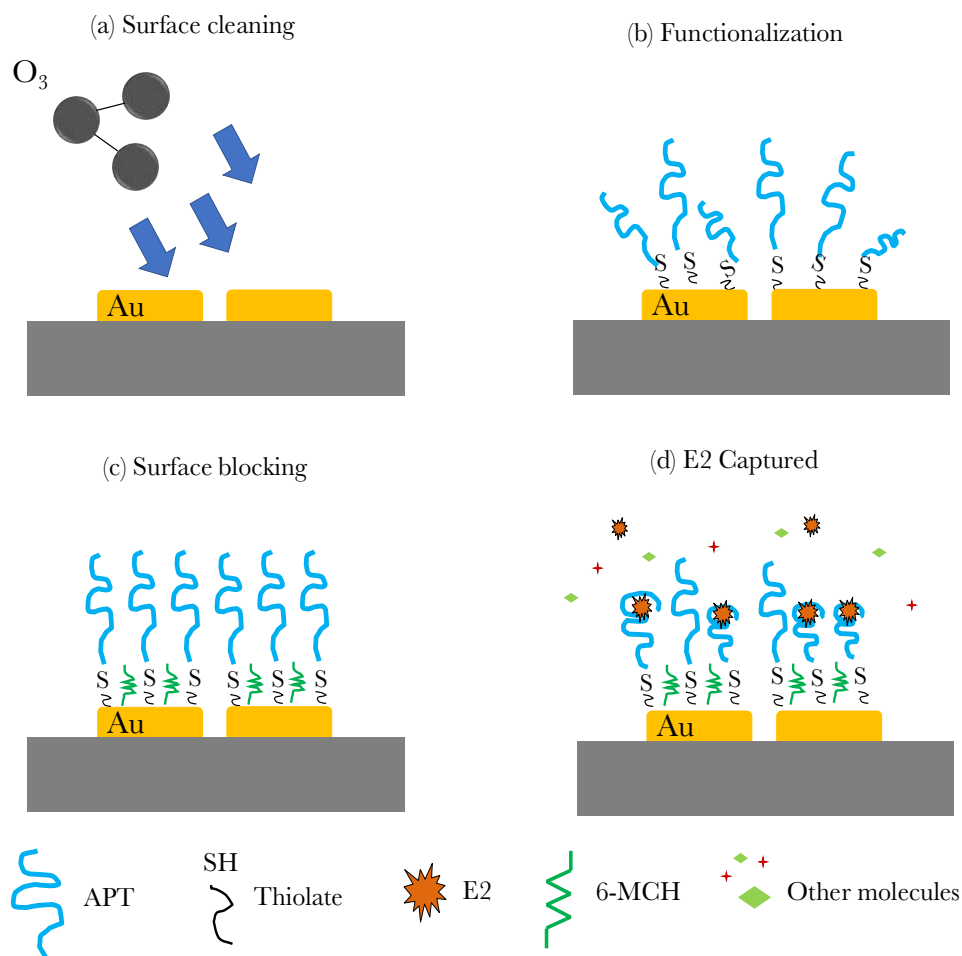


Figure 6.1: Schematic images of the surface functionalization of APT on the gold nanostructures samples following the protocol [12]. (a) the sample was clean with UV ozone, (b) surface functionalization to attach the aptamer on gold surface (c) surface blocking to cover the empty space on gold surface (d) E2 to be captured by the aptamer.

The same method was performed on the ASH nanostructures samples to produce a monolayer of APT on the gold surface with homogenous surface and orientation. Schematic images of the surface functionalization on the ASH samples were as shown in Figure 6.1. The sample was first rinsed using absolute ethanol and blown dry using nitrogen gun. Then, the sample was placed under UV ozone for 20 minutes to remove any residues or organic materials on top of the sample. Next, a drop of 50 μl of APT solutions was deposited on the nanostructure surface to activate the thiol terminal groups. Wet paper was added to the petri dish to prevent the sample from drying. Incubation was carried out for one hour at room temperature and all the work was done under the fume hood cabinet to avoid any contamination. Unbound APT was removed by rinsing the sample three times in clean Tris-HCl buffer solution and rinsed with DI water. The sample was blow-dried before the measurement. Samples could be kept for a few weeks due to the stability of the APT. Then, the 6-Mercapto-1-hexanol was used to block the free sites on the gold

surface to avoid non-specific binding. The surface was then rinsed with PBS three times to remove any excess MCH after one-hour deposition. The sample is blown dry again. Finally, different concentrations of E2 solutions in DI water were deposited for one hour on the surface. Unbound E2 was washed three times with DI water.

6.4 Results and discussions

6.4.1 Detection of 6-mercapto-1-hexanol

MCH was deposited on ASH sample and on bare ZnSe substrate. The vibrational modes in MCH are the O-H stretching at 2.98 μm , C-H stretching at 3.42 μm and 3.50 μm , S-H stretching at 3.9 μm , and C-H bending at 7.11 μm [13], [14]. MCH did not bind to the ZnSe substrate and produced the results same as plain ZnSe substrate. The thiol groups of MCH were chemically adsorbed to the ASH surfaces and a self-assembly monolayer (SAM) of MCH was formed. As a result, the ASHs resonances shifted from their initial wavelengths; for ASH₁ from 3.41 μm to 3.47 μm , and for ASH₂ from 5.37 μm to 5.44 μm and 6.59 μm to 6.69 μm indicating binding of MCH and increased local refractive index introduced by the MCH ($n \equiv 1.48$) [14] in Figure 6.2. The resonance peak of ASH₁ red-shifted 60 nm and the C-H stretching bond matched well with the ASH peak at 3.42 μm and 3.50 μm . The C-H bending adsorption wavelength fell on the slope of the ASH₂ resulting in the molecular bond peak intensity being very weak compared to the coupling resonant. The spectral sensitivities of the ASHs are $S_1 = 125 \text{ nm/RIU}$ and $S_2 = 208 \text{ nm/RIU}$. Baseline correction (as mentioned in the Chapter 5)) was carried out on the ASH transmittance measurement to bring out the features of the MCH IR spectrum on the ASH surface. The C-H stretching bonds were strongly enhanced on the ASH₁ resonance. The peak position of MCH agreed with the data sheet from Sigma Aldrich for C-H stretching vibrational mode [14]. Subsequently, an E2 solution at 100 μM was deposited on the same sample. It was found that E2 was not retained on the nanostructures as no additional resonance shift was measured (Figure 6.3). This demonstrated the efficiency of MCH as a blocking agent: it binds to gold but does not attach E2. MCH also helps the orientation of the aptamers on the gold surface (Figure 6.1). As a control measurement, 100 μM of E2 solution was deposited on the samples and left sit for an hour. After deposition, the sample was rinsed and blow-dried.

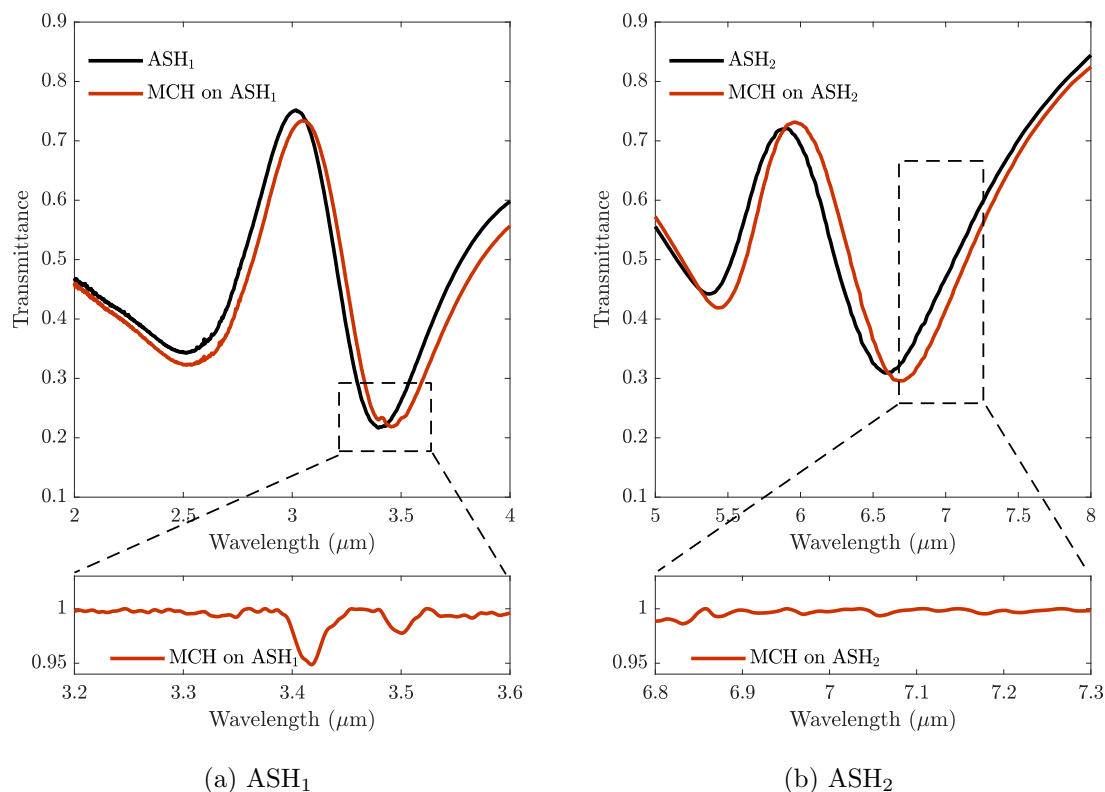


Figure 6.2: The FTIR transmittance spectra of (a) ASH_1 and (b) ASH_2 after deposition of MCH with a concentration of $14.6 \mu\text{M}$. The bottom panel is the zoom in view of the transmittance spectra in (a) to indicate the C-H stretching and C-H bending bond of the MCH.

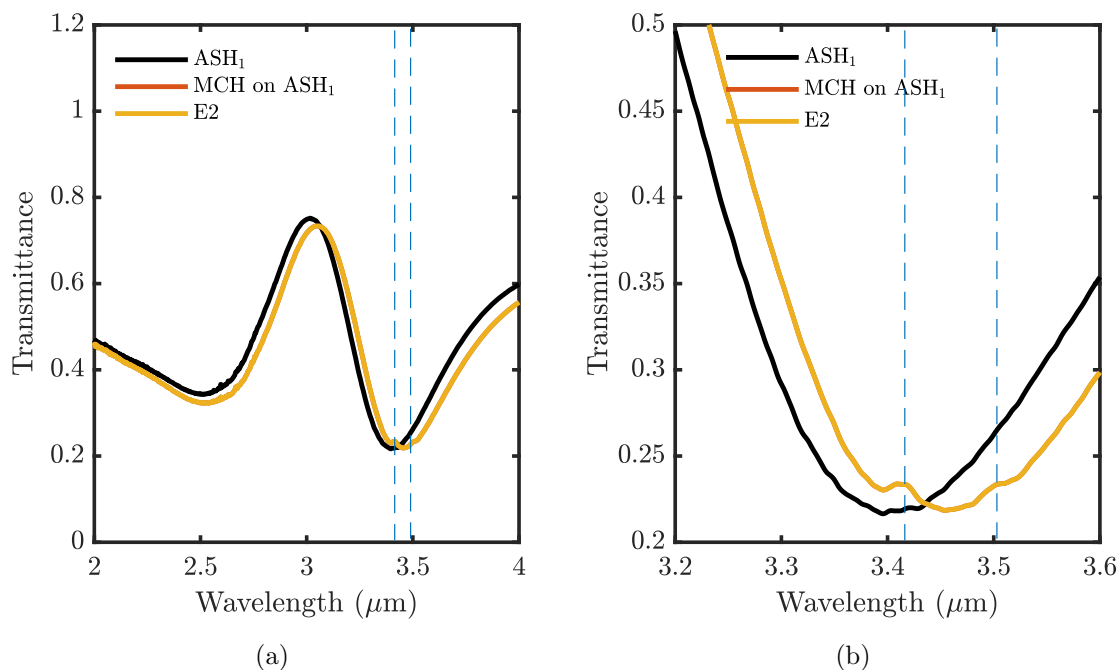


Figure 6.3: The FTIR transmittance spectra of ASH_1 after deposition of $100 \mu\text{M}$ of E2 on MCH (b) The zoom-in view of the transmittance spectra in (a) to indicate no interaction or no resonance shift.

6.4.2 Immobilization of aptamers

6.4.2.1 Experimental Results

Two separated SEIRA experiments were performed to detect DNA molecules. The aptamer was functionalized on two different samples with the same concentration of 18 μM : on the bare ZnSe substrate and on 100 nm thick gold films deposited on ZnSe substrate. After the surface functionalization, the transmittance measurements were performed using FTIR to verify the interaction between the aptamers and these two surfaces. Aptamers did not bind on the ZnSe substrate and on the gold thin film, the features of the aptamer molecular bonds resonances were hardly seen.

A response curve was then built by depositing various concentrations of the aptamers on the samples. The resonance shift of ASH_1 (black line) and ASH_2 (grey line) were measured in response to concentrations of aptamer between 1 μM and 18 μM as shown in Figure 6.4. The resonances were systematically blue-shifted as opposed to the very clear red shift obtained with MCH and the resonance shift value depended on the concentration of APT. The response curve is bell-shaped, with shifts increasing up to 5 μM for ASH_1 then decreasing again sharply above 6 μM . At concentration between 9 μM and 18 μM the resonance shifts were comparable to each other and very small ($< -10\text{nm}$). The surface modification was further confirmed by AFM imaging as shown in Figure 6.13 and 6.14. However, while there was a visible change in the surface when APT were added at a concentration of 3 μM , there was no measurable change in thickness.

6.4.2.2 Simulation

Simulations were performed by varying the thickness of the aptamer in order to understand the experimental results for the blue resonance shift. The ambient dielectric constant of the ASH was modified by varying the refractive index (n) of the aptamer $n = 1.10$ and $n = 1.55$ to find the value that closest matched with the measurement results as shown in Figure 6.5. The ASH arm length was set as 800 nm and 550 nm. Aptamer diameter is around 2 nm to 5 nm and [15], for the simulation the thickness of the aptamer was assumed to be 5 nm thick around the ASH. The thickness was set constant for each value of the refractive index. In particular, as the refractive index increased, the resonance was shifted to longer wavelengths (red shifts), and the peak intensity remained the same. But when the index was below that of the native index the resonance shifted to shorter wavelengths. Initially, when the refractive index is equal to $n = 1.10$ with thickness 5 nm, the resonance was

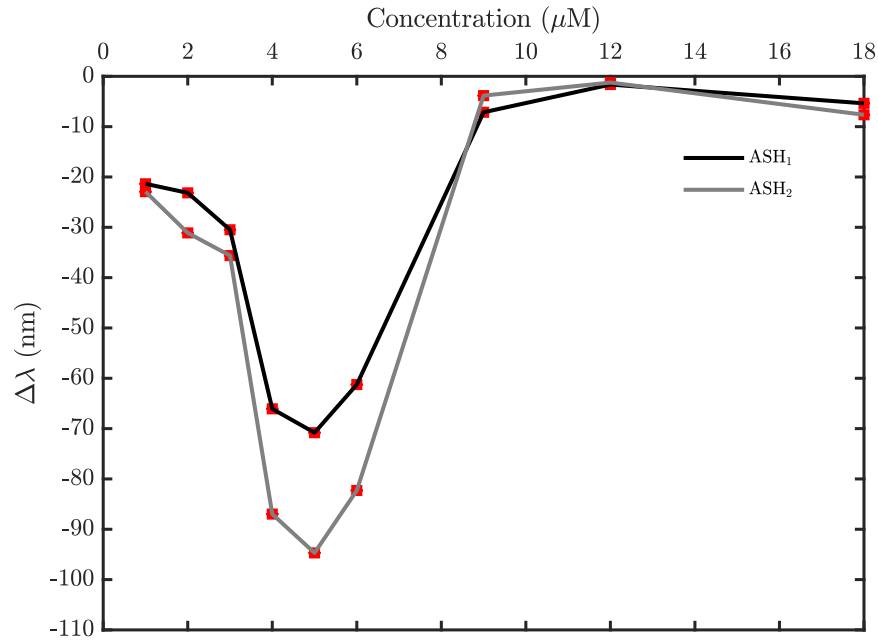


Figure 6.4: Measured wavelength shifts of the ASH₁ (black line) and ASH₂ (grey line) transmittance resonance as a function of aptamer (APT) concentration. The error bars are representing the standard deviation of three measurements were taken in the same sample with different arrays. The negative values represent the blue shifting of the resonance.

blue shifted from the initial wavelength was at 3.55 μm, giving new resonance at 3.51 μm. As the value of the refractive index increased, the resonance was still red-shifted but to longer wavelengths.

The aptamer was dissolved in Tris HCl buffer and the refractive index of Tris HCl buffer is between $n = 1.35$ and $n = 1.36$ and the refractive index of the water, $n = 1.33$. The resonance shift for $n = 1.52$ matched best the experimental results of 12 μM aptamer concentration. The simulated resonance peak positions with respect to the refractive index values are plotted in Figure 6.7(a). In addition, Figure 6.5 shows the effect of the thickness of the aptamer layer, and the simulation was performed with a constant value of the refractive index of $n = 1.52$. Resonance shift was measured in a response to different thickness of aptamer from 0 nm to 10 nm thick with the refractive index, $n = 1.52$ shown in Figure 6.7(b). Initially, the largest blue shift of 35 nm was observed when the thickness was 2 nm. However, when the thickness was 6 nm, the resonance did not shift and as the thickness was increased over 6 nm, the resonance became red-shifted. When the thickness was 10 nm the graph shows the saturation effect.

6.4.2.3 Discussion

The properties of oligonucleotides monolayers on gold have been well characterised. When the concentration of aptamers is too low, physisorption via van der Waals bonding between the aptamers' amine groups and the gold also occurs additionally to the Au-S bonding. Effectively, the aptamer is "lying down". When the aptamer is "lying down", the thickness on the gold surface is reduced, which can explain why the resonance is blue-shifted as demonstrated by simulation. When the concentration of the aptamers is increased, the aptamers are forced "up" by electrostatic repulsion [16]. However, as the density was expected to increase with higher concentration of aptamer, the blue shift became larger not smaller as anticipated by the simulation. While MCH is a neutral compound and produced the expected red shift that come with high concentration, aptamers carry a negative (one electron) charge for each 'mer. The orientation in which the aptamer is immobilized affects its folding and hence its conformation and the effective charge density of the aptamer is very sensitive to its conformation [17]. Therefore, the charge differences between the shift value at 2 μM and 6 μM could be due to a drastic change in conformation related to the aptamers being "up". The red shift of MCH was attributed to a change of refractive index in the surrounding environment of the nanostructures. The systematic blue shift observed here has also been reported in the literature for self-assembly on gold of negatively charged aromatic carboxylates. The effect might be attributed to three different factors; the Stark tuning effect, metal-adsorbate charge transfer and lateral dipole-dipole interactions [18]–[20] and it might be further enhanced by conformational change. The very low shift for high density of aptamers, however, could not be explained by current literature on aptamer SAM. The experimental results also does not show the saturation level, this is might be the aptamers were lose their binding after the immobilizations due to the three different factors as explained; the surface may be directly interfere with the aptamer folding, the aptamers is highly negative charge, and the immobilization density. Future experiments are needed to investigate the APT conformation on the gold surface and its surroundings.

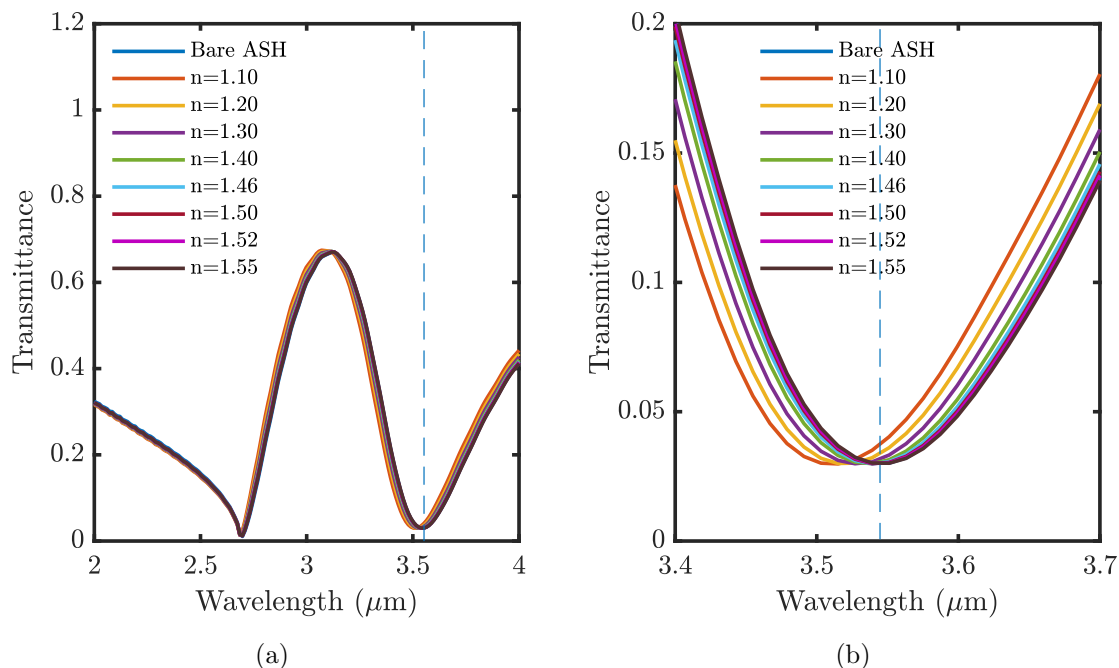


Figure 6.5: (a) Simulated transmittance spectra of ASH with a different value of the refractive index (n). The blue dotted line indicated the initial resonance of the bare ASH. (b) the zoom-in view of (a) showing the resonance was blue-shifted.

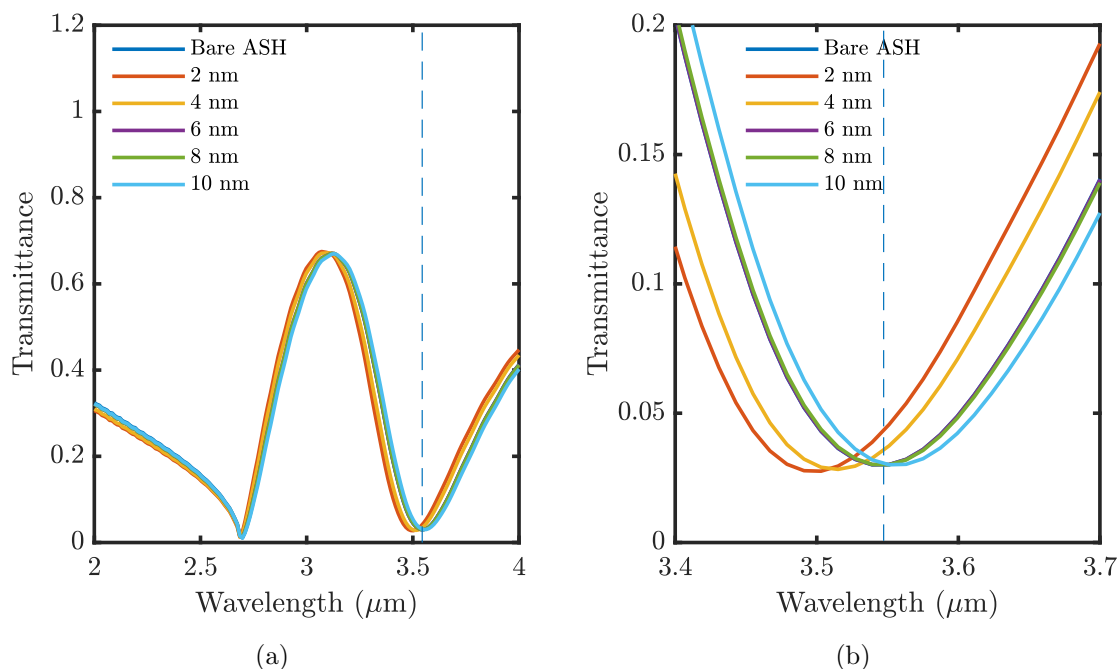


Figure 6.6: (a) Simulated transmittance spectra of the different thickness of aptamer varied from 2 nm to 10 nm (b) zoom-in view of (a) showing the transmittance spectra are blue-shifted and red-shifted depending on the thickness of aptamer.

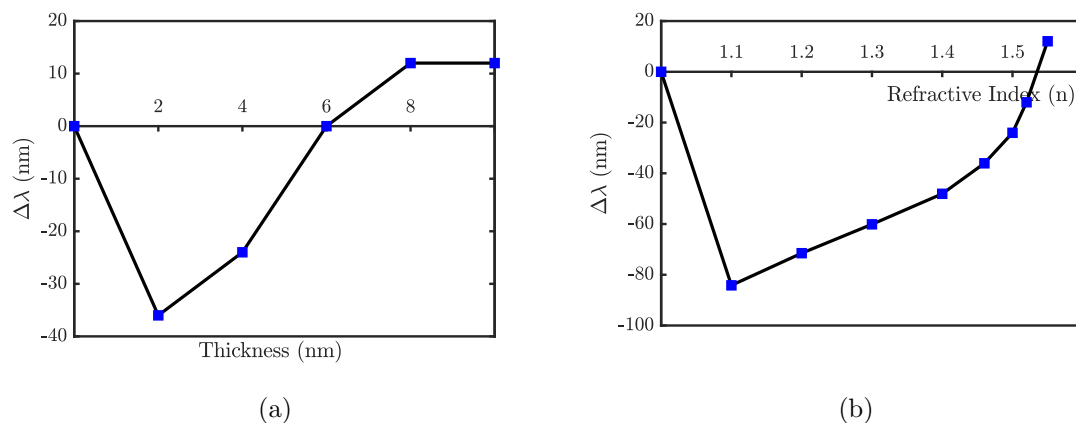


Figure 6.7: (a) Simulation transmittance peaks as a function of the refractive index value (b) Simulations wavelength shifts of the ASH transmittance spectra as a function of the thickness of aptamer. The refractive index of the aptamer was set, $n = 1.52$.

6.4.3 Detection of 17 β -Estradiol (E2)

As reflected in the previous chapter, by tuning the ASH resonance to be matched with the molecular bond resonances, large enhancements can be obtained. The ASH₁ nanostructures were designed purposely to exhibit resonances between 2.00 to 4.00 μm that covers the molecular vibration of C-H bonds. The intend is that the method implemented in this chapter will be used for optical biosensing for specific detection of E2. The ASH has been functionalized following the protocol and methodology in the section above. Aptamers concentration of 1 μM , 3 μM and 12 μM of DNA were selected for the following experiment for E2 detection were performed. A calibration curve was built with various concentration of E2. The range of detection is between 0.27 ng/ml to 270 $\mu\text{g/ml}$ equivalent 1 nM to 100 nM. Three identical arrays were fabricated on the same sample to test the reproducibility of the spectra. The assumption of the thickness after the functionalization is less than 5 nm because the diameter of the aptamer is up to 5 nm. The AFM images did not show major increase of the thickness compared to the bare ASH.

6.4.3.1 Refractive index sensing

The total resonance shifts after of deposition of MCH and of the various E2 solutions were calculated based on the peak position of the bare ASH as the initial value. Figure 6.8 shows the resonance shifts as a function of the concentration of the E2 on ASH₁. For nanostructures functionalised with 1 and 3 μM of aptamers, the addition of MCH did not create a significant additional shift. In all cases, higher concentrations of E2 lead to stronger blue shift. 3 μM showed a better sensitivity than 1 μM , indicating that indeed more aptamers were assembled on the gold. When 12 μM of APT were used, the addition of MCH produced an important red shift (43 nm).

This is an indication that many sites were available on the gold and hence that at high concentration of aptamers adsorption was less efficient. The addition of E2 did re-establish the blue shift. For small molecules, the binding of the target analyte to aptamers triggers a conformation change, to a more structured and possibly smaller structure, which in turns leads to a change in charge density. This change could explain why increasing concentration of E2 lead to a larger blue shift. The results for 12 μM would indicate that the charge density changes produce bigger refractive index changes than thickness.

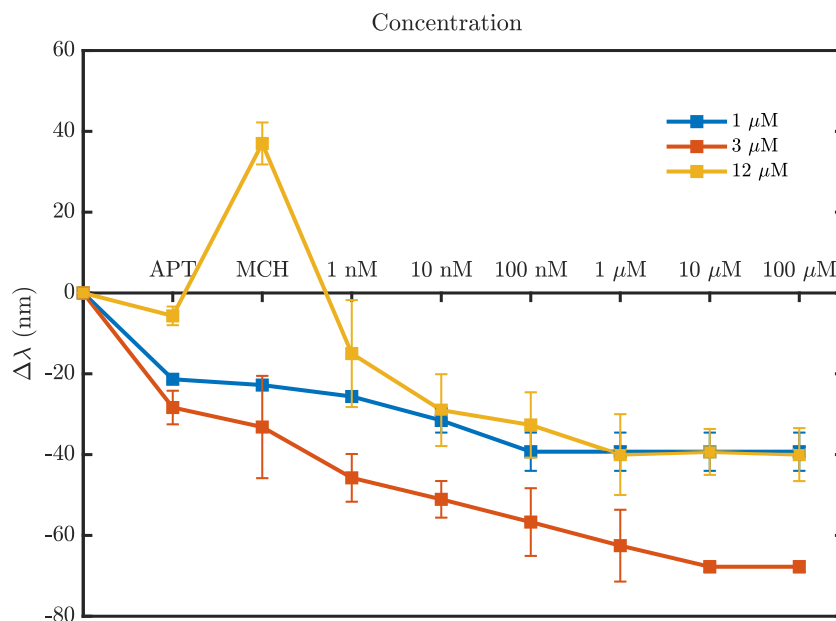


Figure 6.8: The resonance shifts as a function of the concentration of the E2 on ASH1. The resonance shifts were calculated based on the peak position of the bare ASH as the initial value. Two different concentration of aptamer was used in this experiment.

Figure 6.9 shows the same concentration of 3 μM aptamers on ASH₁ and ASH₂. In ASH₁, there was a strong log₁₀ relationship between E2 concentration and blue shift between 1nM and 10 μM whereas ASH₂'s response to E2 addition presented plateaux of shifts. The lowest detection of E2 was 1 nM. APT functionalised ASH₁ nanostructures were demonstrated to be effective refractometric sensors for E2 over 5 orders of magnitudes. When 3 μM of aptamers were used, saturation for E2 occurred between 10 and 100 μM of E2. Further experimental work is needed to calculate the lower detection limit and finding the K_D value. Figure 6.10 shows the same concentration of 3 μM aptamers on ASH₁ and ASH₂ with and without the deposition of MCH. After the deposition of various concentration of the E2, with the help of MCH, the orientation of the APT is in “force up” position and the ASH surface density was fully covered and allowed the APT to fold up the E2. Without

MCH, the aptamer is “lying down”, the RI sensitivity of the ASH was reduced, thus, APT might not be able to fold up the E2.

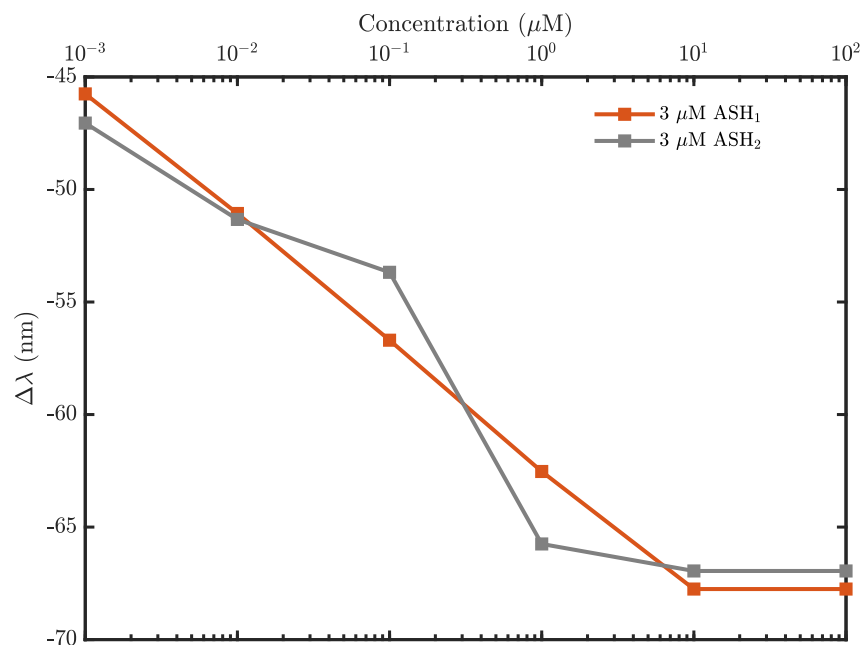


Figure 6.9: Resonance shifts as a function of the same concentration of 3 μM APT and various concentrations of E2 on ASH₁ (red line) and ASH₂ (grey line).

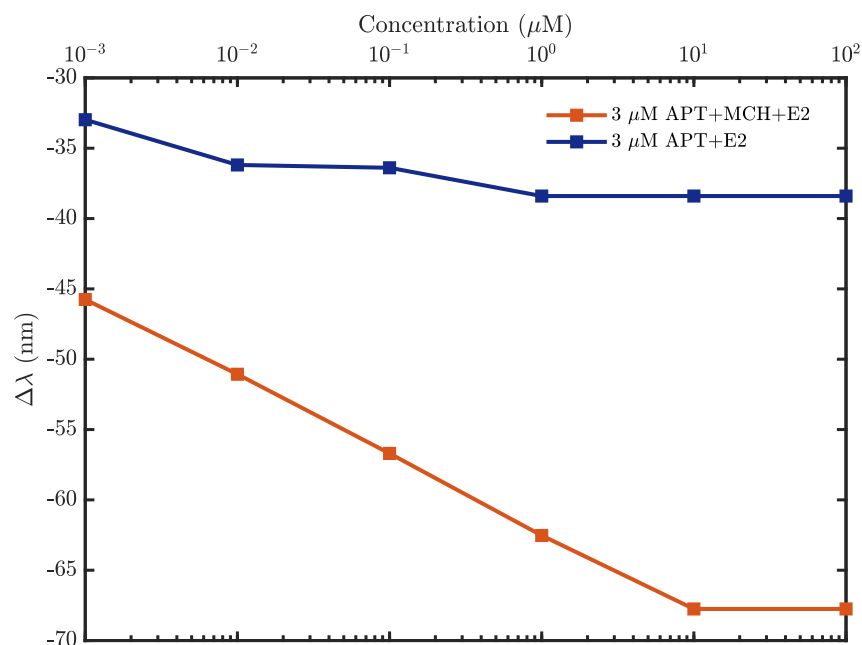


Figure 6.10: RI sensitivity of the ASH with (red line) and without (blue line) the deposition of 6-mercapto-1-hexanol (MCH).

6.4.3.2 Molecular bond sensing

ASH₁ arm lengths of 800 nm and 550 nm were found to provide a resonance with a good match for the C-H stretching bond of E2 as shown in Figure 6.11(a) and 6.11(b). The molecular bond resonance was coupling with the transmittance peak of arm length L_1 compared to the previous chapter 5 in section 5.4.2 where the C-H stretching bond was found to match well with the ASH₁ (800 nm and 600 nm) and the molecular bonds resonance were matched to the reflection dips of the plasmonic resonance. The plasmonic resonance of ASH₂ is used to match with the double bond molecular resonance. Subsequently, molecular bond vibration peak of aptamer does not match (non-resonant coupling) with the transmittance peak of ASH₂, the arm length of ASH₂ can be tuned to longer wavelength between 7 to 8 μm . Therefore, the ASH₂ results will not be discussed in this section and no relevant data will be shown.

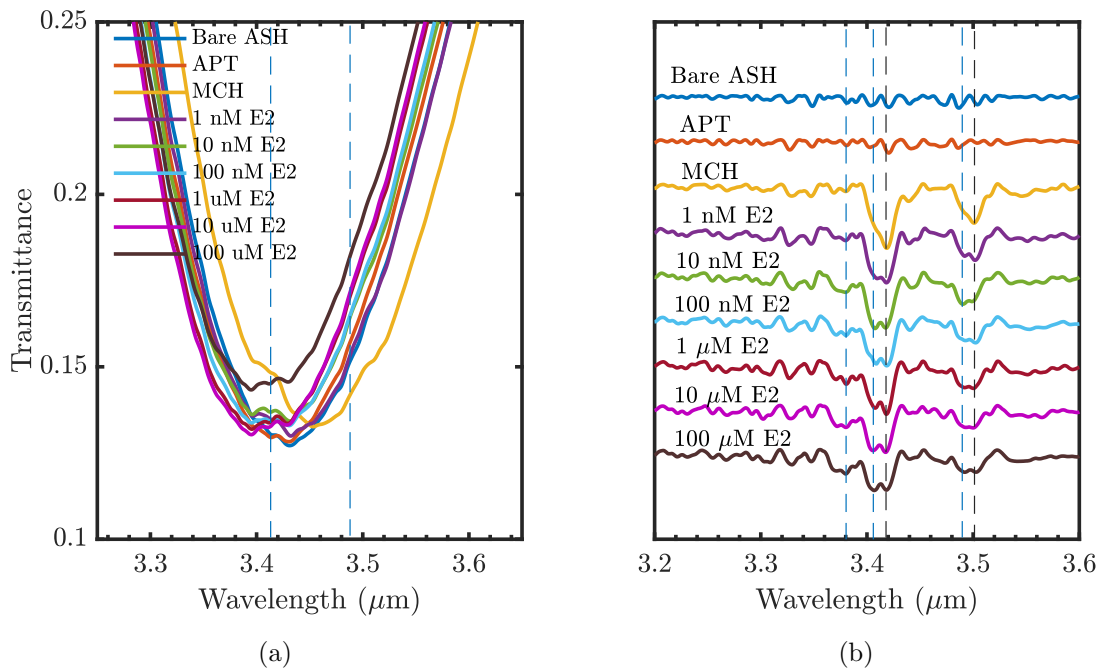


Figure 6.11: (a) Measured transmittance spectra (zoomed in) of ASH arrays after functionalizing the sensor surface with aptamer, the blocking agent (MCH) and subsequent binding with 17 β -Estradiol (E2) with different concentrations. The molecular vibration of C-H bonds is highlighted in blue, respectively. (b) Shows the vibration resonance of each concentration after the baseline correction of the transmittance spectra in (a). The spectra are plots in stacked for better visibility. The respective C-H molecular bond resonance of E2 is shown by the blue dashed line; the C-H bonds of MCH is shown by black dashed line.

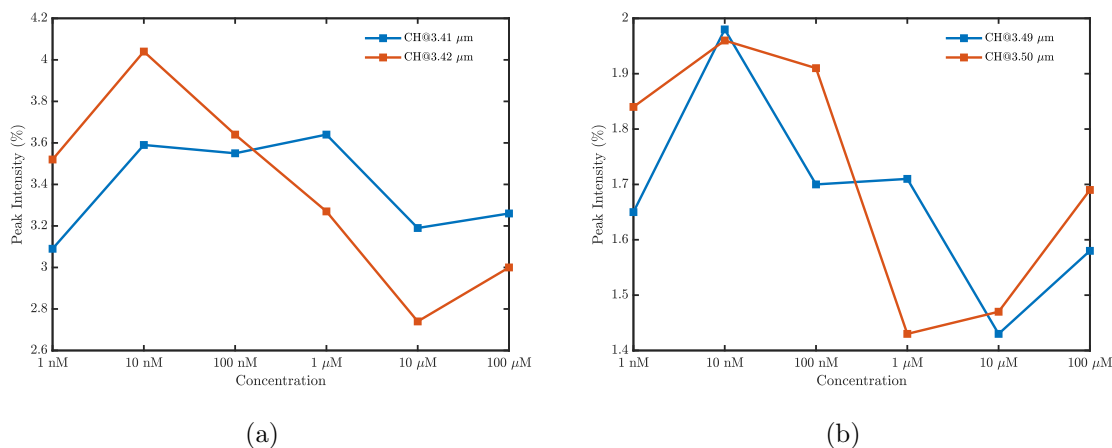


Figure 6.12: Peak intensity observed at 3.41 μm and 3.49 μm as a function of the concentration of E2. The blue line indicated the peak intensity of E2, and the red line indicated the reducing of peak of MCH at 3.42 μm and 3.50 μm.

The vibrational signal of the C-H bond was barely seen even in the resonance coupling condition. The spectra were magnified over the range of 3.25 to 3.65 μm, the vibrational signal of C-H bonds of E2 (symmetric and asymmetric stretching of CH₂ and asymmetric stretching of CH₃) observed at 3.41 μm and 3.49 μm become quite prominent. The two dotted lines (Figure 6.11) are the highlighted area is the position of the C-H stretching vibrations bond resonance. The peaks at 3.42 μm and 3.50 μm were assigned to the C-H stretching bond of the MCH. The detected vibrational molecular bond was calculated as the difference between peak to peak after the baseline correction. It was found that the peak intensity of E2 slowly increased and reaches 0.034 at 1 nM and the peak of MCH decreased to 0.03. As the concentration increased from 1 nM to 100 μM the peak signal at 3.41 μm and 3.49 μm also increased as shown in Figure 6.12(b). The ASH nanostructures amplified the vibrational signals by one order magnitude comparing to the deposition of E2 on the bare gold surface. The resonance blue shift with increasing E2 concentration, however, will also affect the peak intensity. At the concentration of 100 μM the peak amplitude of the resonance was reduced to 20% compared to the previous concentration at 10 μM. The resonance has not shifted but the amplitude of the resonance was reduced. This could be due to saturation, where the signal does not increase further with further concentration, was reached between these two concentrations (Figure 6.8) (Figure 6.11(b)). The sensor was able to detect E2 specific molecular bond but in contrast to results obtained in the previous chapter, there was no linear relationship between the concentration and peak intensity.

6.4.4 Surface modification characterized by AFM

The ASH nanostructure surfaces were characterized by Atomic force microscope (AFM). The cross-section tool used to measure the height variation across the 1 μm square scan. As shown in the AFM images below, the initial average thickness of the bare ASH was at $116 \text{ nm} \pm 5 \text{ nm}$. After the immobilization of the APT, the average thickness of the new ASH was found to be $119 \text{ nm} \pm 5 \text{ nm}$. The thickness of the aptamer calculated from the different of the average thickness of ASH with APT and the bare ASH, was found to be approximately $\pm 2.23 \text{ nm}$. The film height was relatively constant as observed by AFM measurements.

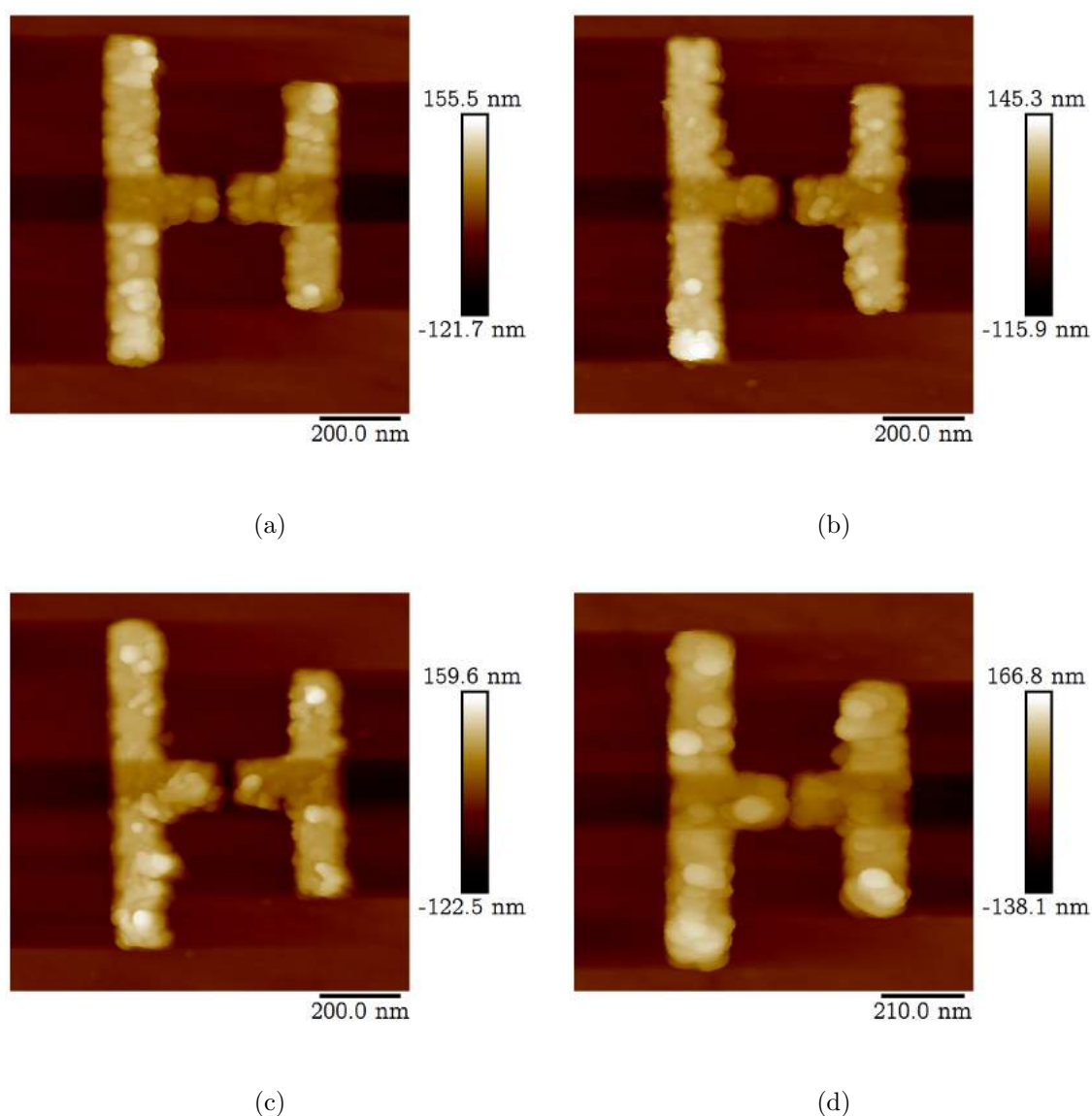


Figure 6.13: AFM image of (a) the bare ASH (b) after the surface functionalization by attaching the APT (c) the uncovered surface was covered by MCH and (d) after the E2 binding.

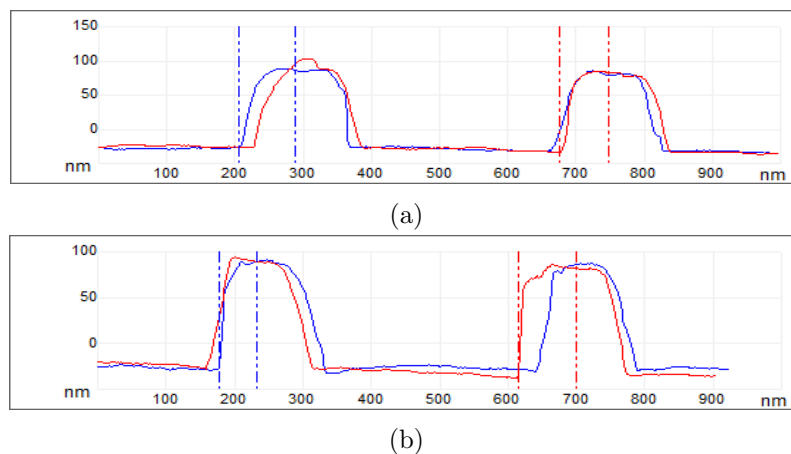


Figure 6.14: Height profile of the AFM images in Figure 6.13 (a) ASH alone with (b) APT on the ASH. The blue the red line indicates the height profile at a different area and measured from the baseline to the top peak.

6.5 Conclusion

In conclusion, this chapter has demonstrated aptamers as a bio-recognition element that binds to E2 which has been functionalized on the ASH nanostructures and with MCH used as a blocking agent to prevent non-specific binding on the gold surface. Thus, this can be applied as a label-free optical sensor to detect the E2 in the environment. mMCH was attached on ASH with the sensitivity were 105 nm/RIU (ASH₁) and 208 nm/RIU (ASH₂). The molecular vibration of C-H bonds of the MCH were matched with the transmittance peak of ASH₁ and the molecular bond resonances were 500 times larger. After the immobilization of the aptamers, the resonances were blue-shifted and the total resonance shift are depending on the concentration of APT. However, in this experiment, the ASH worked more efficiently as a refractometric sensor than as a quantitative SEIRA sensor. The experimental results showed that the E2 could be detected at concentration as low as 1 nM equivalent to 0.27 ng/ml.

Acknowledgement

The author wishes to express her gratitude to Associate Prof Nathalie Lidgi-Guigui from Université Paris 13 for the surface functionalization techniques, Dr Rungroch Sungthong (University of Glasgow) for the aptamers dilution in the environmental laboratory, Dr Samadhan Patil (University of Glasgow) for discussions regarding the analysis of the results and Scottish Research Partnership in Engineering (SRPe) for funding the visit in France.

References

- [1] S. Roh, T. Chung, and B. Lee, *Overview of the characteristics of micro- and nano-structured surface plasmon resonance sensors*, Jan. 2011. [Online]. Available: <http://www.mdpi.com/1424-8220/11/2/1565/> (cit. on p. 102).
- [2] O. A. Alsager, S. Kumar, B. Zhu, J. Travas-Sejdic, K. P. McNatty, and J. M. Hodgkiss, “Ultrasensitive Colorimetric Detection of 17β -Estradiol: The Effect of Shortening DNA Aptamer Sequences,” *Analytical Chemistry*, vol. 87, no. 8, pp. 4201–4209, Apr. 2015 (cit. on pp. 102, 104).
- [3] N. Yildirim, F. Long, C. Gao, M. He, H.-C. C. Shi, and A. Z. Gu, “Aptamer-based optical biosensor for rapid and sensitive detection of 17β -estradiol in water samples,” *Environmental science & technology*, vol. 46 VN - r, no. 6, pp. 3288–3294, Mar. 2012 (cit. on pp. 102, 103).
- [4] H. Hou, X. Bai, C. Xing, N. Gu, B. Zhang, and J. Tang, “Aptamer-based cantilever array sensors for oxytetracycline detection,” *Analytical Chemistry*, vol. 85, no. 4, pp. 2010–2014, Feb. 2013 (cit. on p. 103).
- [5] S. U. Akki and C. J. Werth, “Critical Review: DNA Aptasensors, Are They Ready for Monitoring Organic Pollutants in Natural and Treated Water Sources?” *Environmental Science and Technology*, vol. 52, no. 16, pp. 8989–9007, Aug. 2018 (cit. on p. 103).
- [6] Y. S. Kim, H. S. Jung, T. Matsuura, H. Y. Lee, T. Kawai, and M. B. Gu, “Electrochemical detection of 17β -estradiol using DNA aptamer immobilized gold electrode chip,” *Biosensors and Bioelectronics*, vol. 22, no. 11, pp. 2525–2531, May 2007. arXiv: [NIHMS150003](https://arxiv.org/abs/NIHMS150003) (cit. on pp. 103, 105).
- [7] K. J. Huang, Y. J. Liu, G. W. Shi, X. R. Yang, and Y. M. Liu, “Label-free aptamer sensor for 17β -estradiol based on vanadium disulfide nanoflowers and Au nanoparticles,” *Sensors and Actuators, B: Chemical*, vol. 201, pp. 579–585, Oct. 2014 (cit. on p. 103).
- [8] L. Fan, G. Zhao, H. Shi, M. Liu, Y. Wang, and H. Ke, “A Femtomolar Level and Highly Selective 17β -estradiol Photoelectrochemical Aptasensor Applied in Environmental Water Samples Analysis,” *Environmental Science & Technology*, vol. 48, no. 10, pp. 5754–5761, May 2014 (cit. on p. 104).
- [9] S. U. Akki, C. J. Werth, and S. K. Silverman, “Selective Aptamers for Detection of Estradiol and Ethynylestradiol in Natural Waters,” *Environmental Science and Technology*, vol. 49, no. 16, pp. 9905–9913, Aug. 2015 (cit. on p. 104).

- [10] S. Liu, R. Cheng, Y. Chen, H. Shi, and G. Zhao, “A simple one-step pretreatment, highly sensitive and selective sensing of 17β -estradiol in environmental water samples using surface-enhanced Raman spectroscopy,” *Sensors and Actuators B: Chemical*, vol. 254, pp. 1157–1164, Jan. 2018 (cit. on p. 104).
- [11] M. Liu, H. Ke, C. Sun, G. Wang, Y. Wang, and G. Zhao, “A simple and highly selective electrochemical label-free aptasensor of 17β -estradiol based on signal amplification of bi-functional graphene,” *Talanta*, vol. 194, pp. 266–272, Mar. 2019 (cit. on p. 104).
- [12] M. Cottat, C. D’Andrea, R. Yasukuni, N. Malashikhina, R. Grinyte, N. Lidgi-Guigui, B. Fazio, A. Sutton, O. Oudar, N. Charnaux, V. Pavlov, A. Toma, E. Di Fabrizio, P. G. Gucciardi, and M. Lamy de la Chapelle, “High Sensitivity, High Selectivity SERS Detection of MnSOD Using Optical Nanoantennas Functionalized with Aptamers,” *The Journal of Physical Chemistry C*, vol. 119, no. 27, pp. 15 532–15 540, Jul. 2015 (cit. on pp. 106, 107).
- [13] H. Tan, T. Zhan, and W. Y. Fan, “Direct functionalization of the hydroxyl group of the 6-mercapto-1-hexanol (MCH) ligand attached to gold nanoclusters,” *Journal of Physical Chemistry B*, vol. 110, no. 43, pp. 21 690–21 693, 2006 (cit. on p. 108).
- [14] *6-Mercapto-1-hexanol* — $C_6H_{14}OS$ - PubChem. [Online]. Available: <https://pubchem.ncbi.nlm.nih.gov/compound/560126> (visited on 07/06/2019) (cit. on p. 108).
- [15] J. Zhou and J. Rossi, “Aptamers as targeted therapeutics: current potential and challenges,” *Nature Reviews Drug Discovery*, vol. 16, no. 3, pp. 181–202, Mar. 2017 (cit. on p. 110).
- [16] C. Y. Chen, C. M. Wang, P. S. Chen, and W. S. Liao, “Self-standing aptamers by an artificial defect-rich matrix,” *Nanoscale*, vol. 10, no. 7, pp. 3191–3197, Feb. 2018 (cit. on p. 112).
- [17] W. Ren, K. Zheng, C. Liao, J. Yang, and J. Zhao, “Charge evolution during the unfolding of a single DNA i-motif,” *Physical Chemistry Chemical Physics*, vol. 20, no. 2, pp. 916–924, Jan. 2018 (cit. on p. 112).
- [18] K. Ashley and S. Pons, “Infrared Spectroelectrochemistry,” *Chemical Reviews*, vol. 88, no. 4, pp. 673–695, 1988 (cit. on p. 112).
- [19] B. Han, Z. Li, and T. Wandlowski, “Adsorption and self-assembly of aromatic carboxylic acids on Au/electrolyte interfaces,” *Analytical and Bioanalytical Chemistry*, vol. 388, no. 1, pp. 121–129, Mar. 2007 (cit. on p. 112).

- [20] D. K. Lambert, “Vibrational stark effect of adsorbates at electrochemical interfaces,” *Electrochimica Acta*, vol. 41, no. 5 SPEC. ISS. Pp. 623–630, Apr. 1996 (cit. on p. 112).

Chapter 7

Conclusions and future work

7.1 Aim and Objectives

The aim of this study was to develop a novel plasmonic biosensor that will specifically detect in water estrogenic hormones (analytes) that are detrimental to humans and animals. The specific objectives were to:

1. Perform simulation, fabrication and characterisation asymmetric split-H (ASH) gold nanostructures on a dielectric substrate to produce double resonance peaks to be matched with the infrared vibrational energies of the bonds in the targeted molecules.
2. Tune the plasmonic resonances of ASH nanostructures to match with the molecular vibration resonances of estrogenic hormones, namely Estrone (E1), 17β -Estradiol (E2), Estriol (E3) and 17α -Ethinyl Estradiol (EE2), simultaneously detect the hormones in mixtures and quantify their molar fraction.
3. Functionalize ASH nanostructure surface with a specific bio-recognition element which will be used to bind with the 17β -Estradiol (E2) and test the sensing performance after functionalization.

The final findings are recalled below to demonstrate how the work meets the aim and objectives of the project. This chapter will also look at how the work could be further advanced.

7.2 Summary findings and conclusion

The devices were fabricated on silica and zinc selenide (ZnSe) substrates. The effects of changing the geometry of the nanostructures and the array period on the substrate was investigated using simulation and experimental results. Double plasmonic resonance was obtained in the mid-infrared wavelength between 2 and 8 μm by tuning

the geometry of ASH. Q-factor of 26 was achieved from the double ASH (D-ASH) in EX polarizations on a silica substrate, which is twice that of previously reported values. The sensitivity of D-ASH was characterised using PMMA layer and showed a redshift when increasing the environmental refractive index. The sensitivity of the design in the simulation was 1297 nm/RIU. Then, the influence of the substrate was investigated by comparing the ASH on both substrates. ZnSe substrate was chosen to ensure low-loss transmission operation up to 21 μm . However, due to the high refractive index of ZnSe, the medium Q-factor value of only 12 was achieved compared to the 26 obtained for ASH on the silica substrate. The resonances were controllably tuned to align with the targeted wavelengths of the molecular bonds of analytes and the locations of each resonance depended on the arm-length of ASH. A thin layer various of refractive index values was also simulated to measure the RI sensitivity of the ASH on ZnSe substrates is 586 nm/RIU with the refractive index of $n=1.46$. This work demonstrated that the ASHs could be used for LSPR sensing.

After characterising the estrogen mid-IR vibrational fingerprints, the ASH nanostructures geometry was tuned to enhance the five relevant molecular bonds resonances of four estrogenic hormones (for O-H, C-H, C=O, C=C and C \equiv C-H bonds). Two different sizes of ASH labelled as ASH₁ and ASH₂, with ASH₁'s arm length (L_1 and L_2) varying between 450 nm and 800 nm and ASH₂'s arm lengths between 1.2 μm and 1.6 μm were chosen for the mid-IR region. The ASH₁ structures were optimized to resonate at the wavelengths of the two C-H vibrations of interest and good matches were found for a length of 800 nm (L_1) and 600 nm (L_2). For the C=C bonds, good matches were found with ASH₂, 1.5 μm (L_1) and 1.2 μm (L_2). The plasmonic resonance was red-shifted towards longer wavelengths through the deposition of organic materials on the nanostructure. The ASH nanostructures showed a refractive index sensitivity of 363 nm/RIU (ASH₁) and 636 nm/RIU (ASH₂). The molecular bond resonances were typically 500 times larger, therefore more easily visible and identifiable than those for estrogens deposited on bare substrates. Additionally, the contribution of each different estrogen in mixtures could be quantitatively separated out. This approach, however, did not show specificity towards the estrogens.

Finally, specificity of the devices was introduced using specific thiol-terminated aptamers for 17 β -Estradiol (E2). The surface of the ASH nanostructures was modified to have selective binding and specific detection for E2. Mercaptohexanol was used as a blocking agent to prevent non-specific binding on the gold. The resonances were red-shifted when MCH self-assembled monolayer were formed on the nanostructure and the sensitivity was calculated at $s_1 = 125$ nm/RIU and s_2

= 208 nm/RIU. With additional immobilization of the aptamer between 1 μM and 18 μM , the ASHs were found to be sensitive to refractive index change; for ASH₁ and ASH₂, the maximum resonance shift occurred for a concentration of aptamer of 5 μM and was -70 nm and - 90 nm. The resonances systematically blue-shifted with the addition of DNA because of electronic phenomena due to the high negative charges of the aptamers. Different concentrations of E2 ranging from 1 nM to 100 μM were deposited on the nanostructures. There was good correlation for ASH₁ between the concentrations of E2 and the resonance shift for concentrations between 1 nM and 10 μM . While E2 specific CH₂ and CH₃ vibrational bonds bands were enhanced but their intensities did not change in function of the concentration of E2. ASH nanostructures show better results in the detection of the refractive index changes compared to molecular sensing. These various efforts have demonstrated novel efficient approaches for SEIRA and RI sensing for estrogenic hormones.

7.3 Recommendation for future work

Further works should look into improving the sensors based on knowledge that was established throughout the project and then move towards a usable portable sensor.

7.3.1 Improving the nanofabrication

Nanofabrication could be further improved to improve sensitivity and enhancement factor. Chen *et al.* [1] demonstrated improved sensitivity for similar nanostructures by etching down the substrate around the metallic structures. Because of the high RI of ZnSe, lifting the nanostructure away from the substrate using an additional layer of metal (such as Ag) or a dielectric with a lower RI could narrow the resonance peaks and increase their amplitude. Another strategy developed by Chen *et al.* [1] that could be adopted here to improve the enhancement factor is to add AuNPs near the hot spots of the structures. The substrate could also be replaced to CaF₂ because its transmission is up to 10 μm and its reflection loss is only 10%. CaF₂, however, is slightly soluble in water which is not ideal for the intended application.

For ASH₁, the C-H bond was captured on one of the resonance peaks, but while the second resonance matched the vibrational OH bond wavelength, no peak could be observed. This could be due to the broad linewidth of the resonance. Therefore improving the linewidth of the resonance using the approach described above could help solve this issue too.

7.3.2 Improving surface functionalization

The optimal concentration of aptamer was not fully investigated. Better understanding of the relationship between resonance's blue shift and aptamer concentration could be essential in determining optimal functionalization for maximal molar sensitivity of the device. Similarly, the suspected changes in aptamer conformations when attaching E2 and their effect they have on the surrounding dielectric should be further investigated. SEIRA sensing will only be optimised when these factors are known.

Surface functionalization parameters also need to be improved for maximum sensitivity for the analytes. Notably the nature of the aptamers and the deposition methods could be changed. Indeed, conformational changes have been reported to be more robust when the aptamer is kept away of the gold using a linker between the thiol and the aptamer [2]. Similarly, the use of smaller aptamers (20 to 30 mers) has shown to improve affinity between the gold and the targeted analytes [3]. Additionally, deposition orders between aptamers and MCH on the substrate has also been shown to play a crucial role on the molar sensitivity of sensors.

7.3.3 Towards an environmental sensor

The estrogenic environmental sensor I aim to develop is multiplex, portable and real-time. For multiplexing, a different aptamer should be used that can bind all four molecules. There is, however, no such aptamer currently available and one would have to be isolated. Alternatively, a mixture of aptamers with different estrogenic affinities could be employed. In all cases the K_D of the device would have to be determined for each estrogenic molecule. The work will also continue by investigating and determining the specificity of the aptamers used. The other three types of the estrogen; estrone (E1), estriol (E3) and 17 α - ethinyl estradiol (EE2) and other types of molecules e.g paracetamol will be tested on the sensor surface to demonstrate the specific and non specific binding.

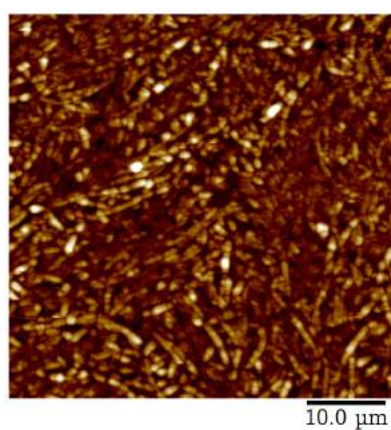
Real-time detection cannot happen if samples need to be dried before measurements. Therefore, the integration of the device into a continuous-flow microfluidic platform should be investigated by merging the biological and chemical components. Literature reports [4], [5] show that microfluidic chips lead to lower limit of detections and faster analytical detection. An in-between analysis flushing method also needs to be developed to capitalise on one of the main advantages of aptamers, which is that they are durable and reusable.

References

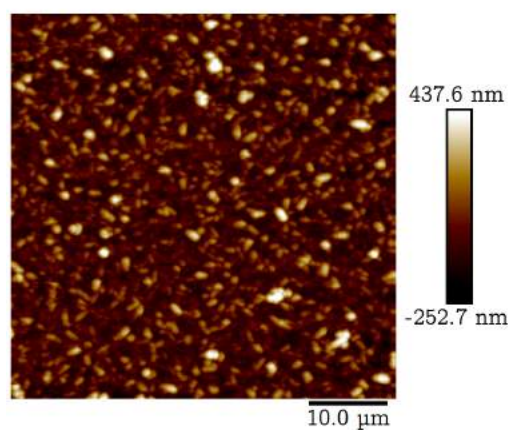
- [1] X. Chen, C. Wang, Y. Yao, and C. Wang, “Plasmonic Vertically Coupled Complementary Antennas for Dual-Mode Infrared Molecule Sensing,” *ACS Nano*, vol. 11, no. 8, pp. 8034–8046, Aug. 2017 (cit. on p. 126).
- [2] T. C. Chiu and C. C. Huang, *Aptamer-functionalized nano-biosensors*, Dec. 2009 (cit. on p. 127).
- [3] O. A. Alsager, S. Kumar, B. Zhu, J. Travas-Sejdic, K. P. McNatty, and J. M. Hodgkiss, “Ultrasensitive Colorimetric Detection of 17β -Estradiol: The Effect of Shortening DNA Aptamer Sequences,” *Analytical Chemistry*, vol. 87, no. 8, pp. 4201–4209, Apr. 2015 (cit. on p. 127).
- [4] T. H. H. Le and T. Tanaka, “Plasmonics–Nanofluidics Hybrid Metamaterial: An Ultrasensitive Platform for Infrared Absorption Spectroscopy and Quantitative Measurement of Molecules,” *ACS Nano*, acsnano.7b02743, Sep. 2017 (cit. on p. 127).
- [5] O. Limaj, D. Etezadi, N. J. Wittenberg, D. Rodrigo, D. Yoo, S.-H. Oh, and H. Altug, “Infrared Plasmonic Biosensor for Real-Time and Label-Free Monitoring of Lipid Membranes,” *Nano Letters*, vol. 16, no. 2, pp. 1502–1508, Feb. 2016 (cit. on p. 127).

Appendix A

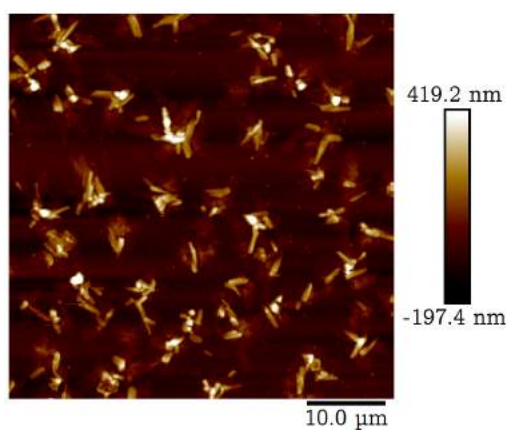
Graphs



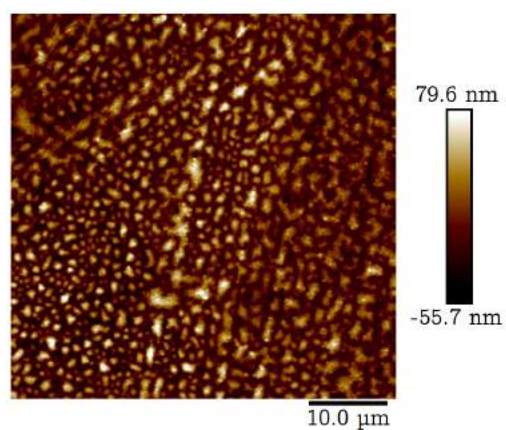
(a) E1



(b) E2



(c) E3



(d) EE2

Figure A.1: AFM images of (a) Estrone (E1) (b) 17β -Estradiol (E2) (c) Estriol (E3) (d) 17α -Ethinyl Estradiol with 1mg/ml solution concentration deposited on the ZnSe substrate. The images were obtained using ScanAsyst mode with the scale bar 10 μm

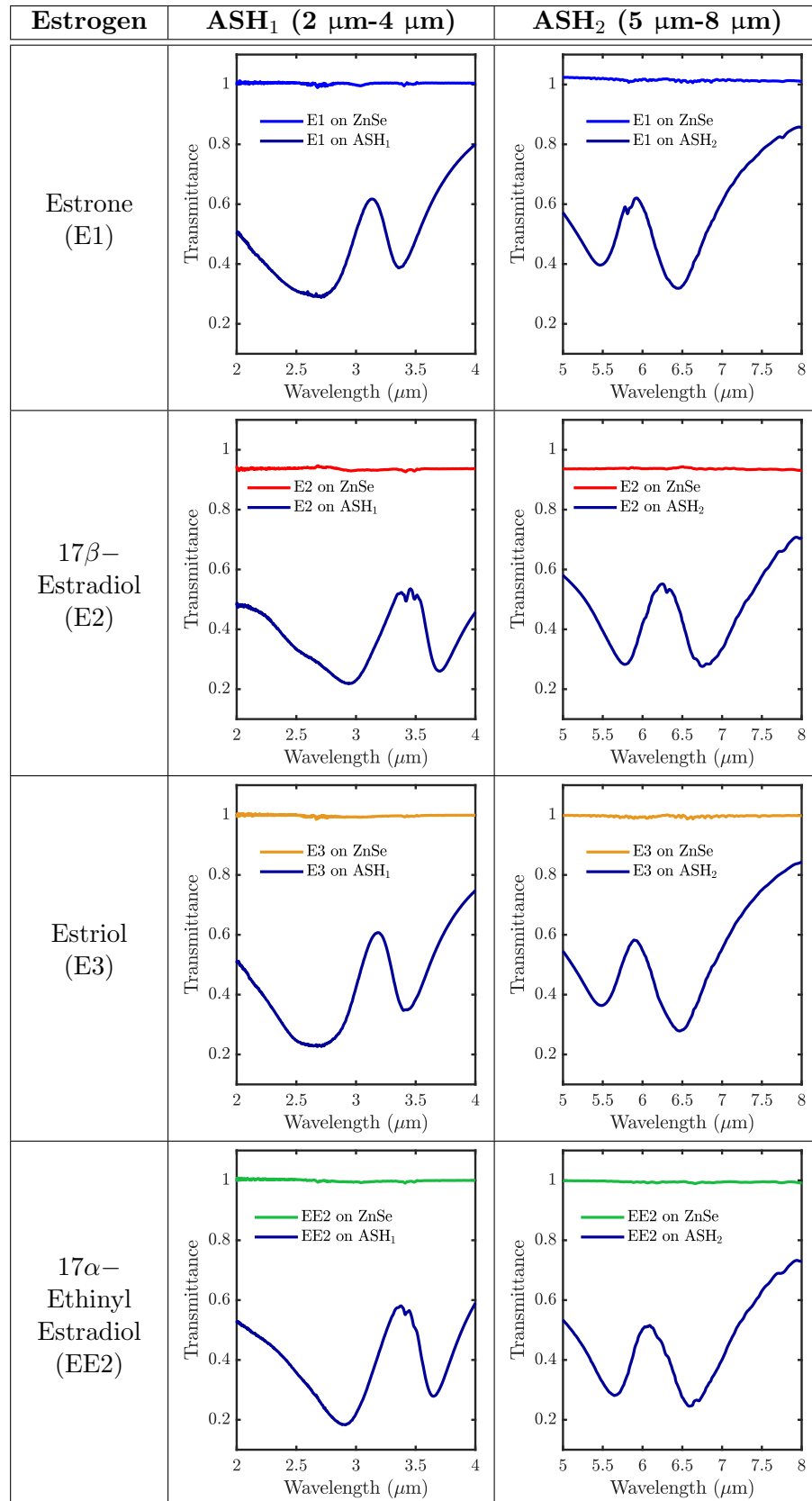


Figure A.2: Matching the molecular bonds of (a) Estrone (b) 17 β -Estradiol (c) Estriol and (d) 17 α -Ethinyl with the plasmonic resonance.

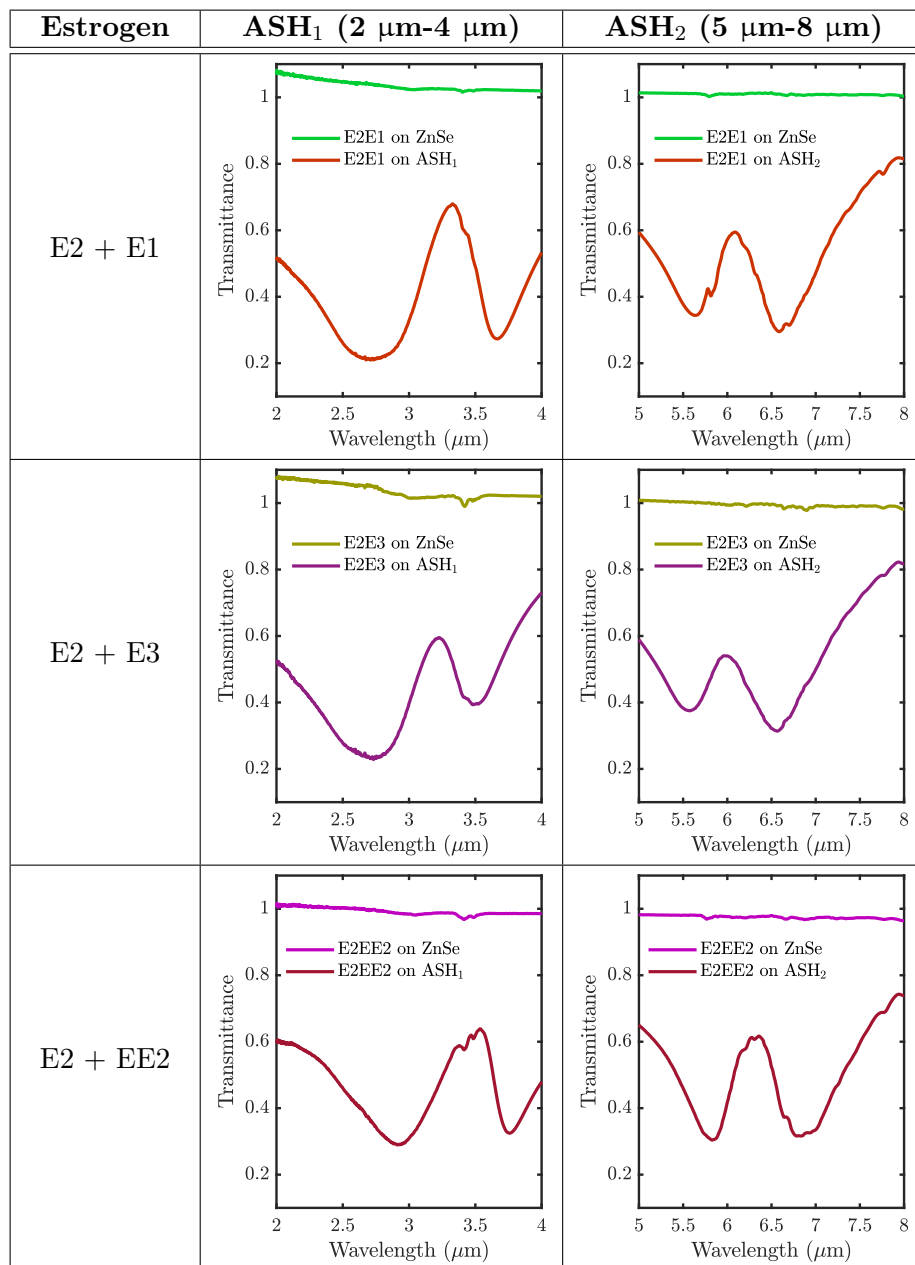


Figure A.3: Plots transmittance resonances from the ASH with the mixture of E2 with E1, E3, and EE2 vibrational resonances for the C-H, C=O and C=C bonds with the inset showing the zoomed plots

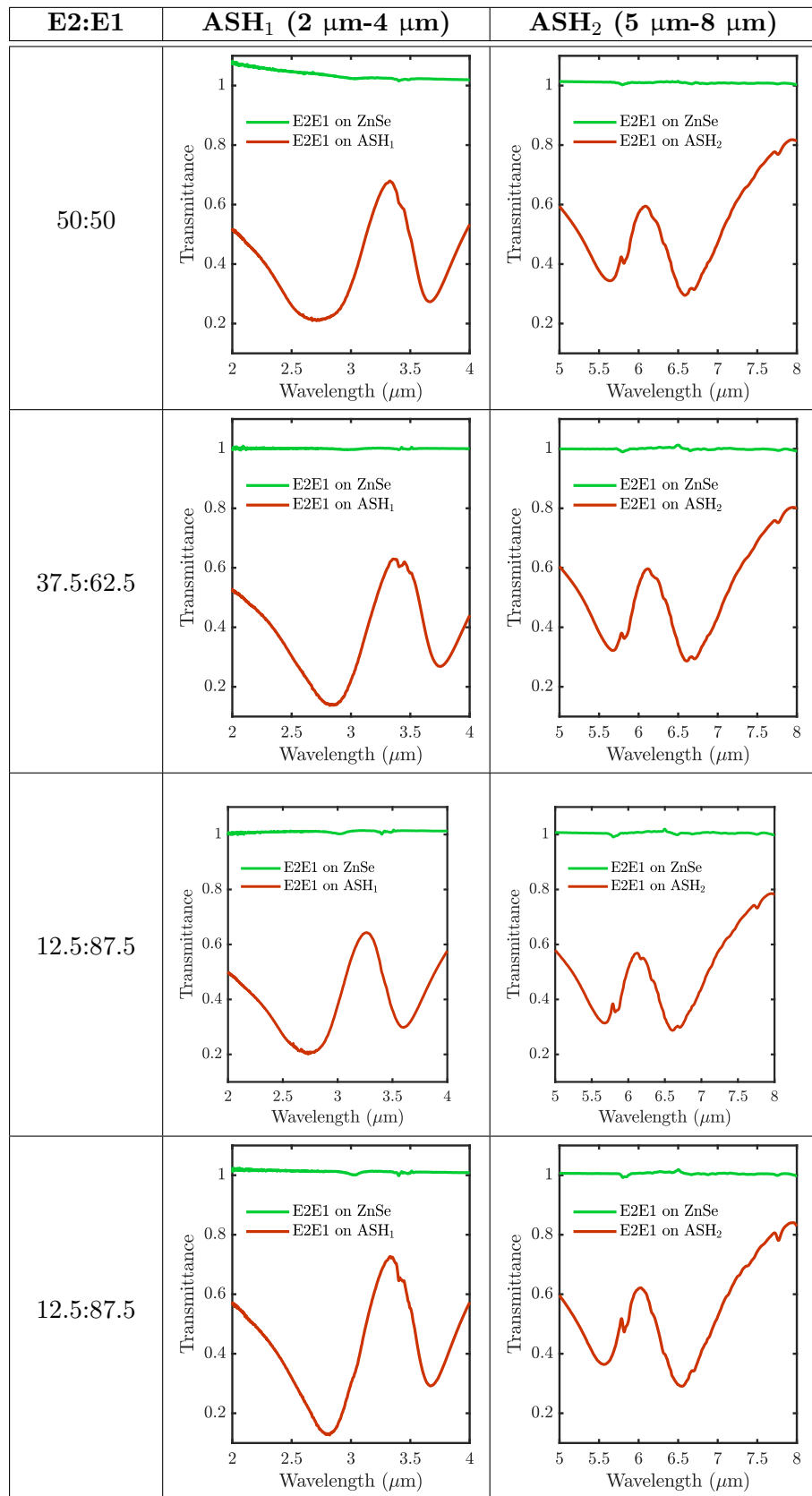


Figure A.4: Plots transmittance resonances from the ASH with the mixture of E2 with E1 with different ratio.

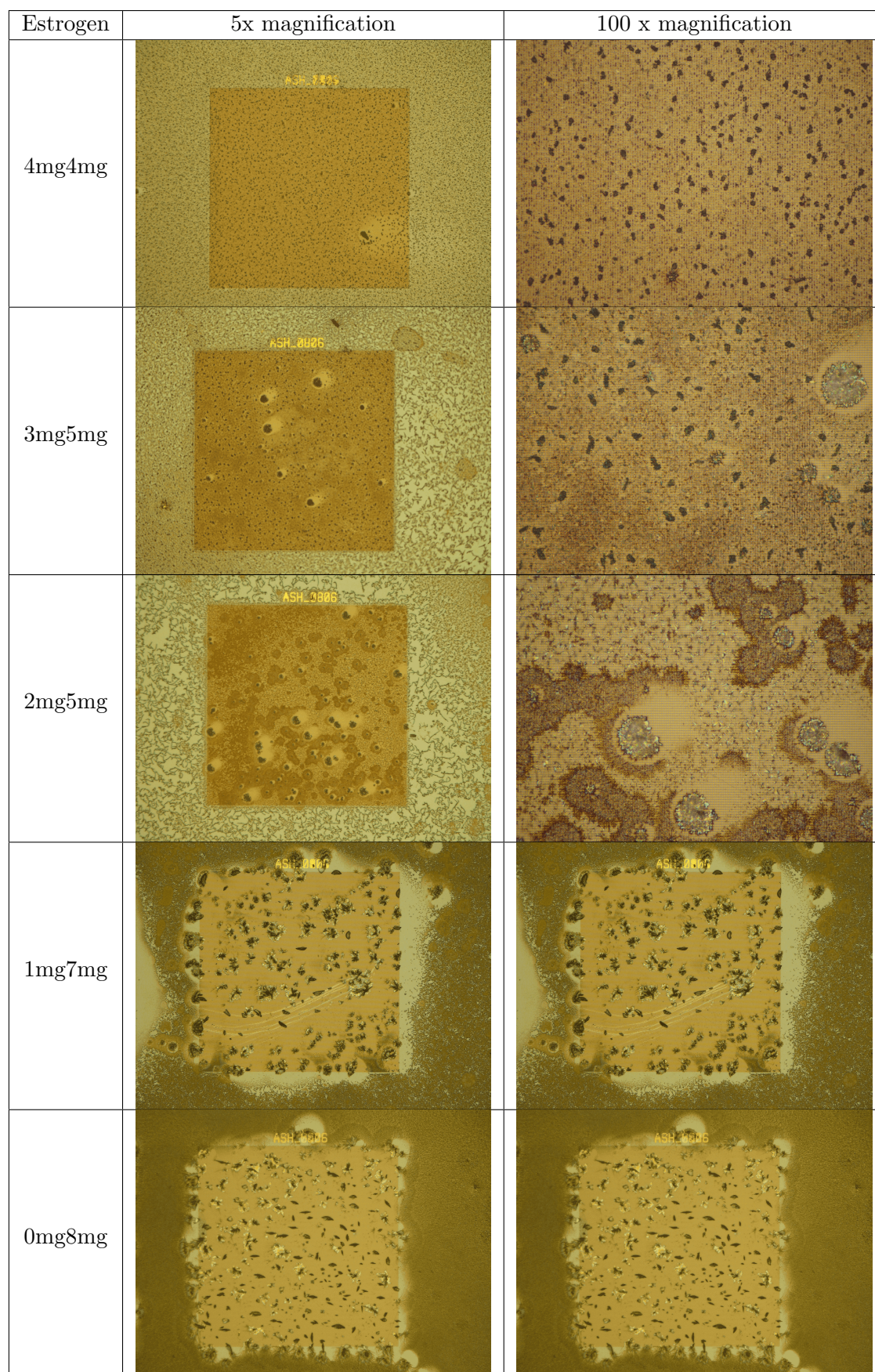


Figure A.5: Microscope images of the mixture of E2 with E1 with a different ratio on the ASH arrays

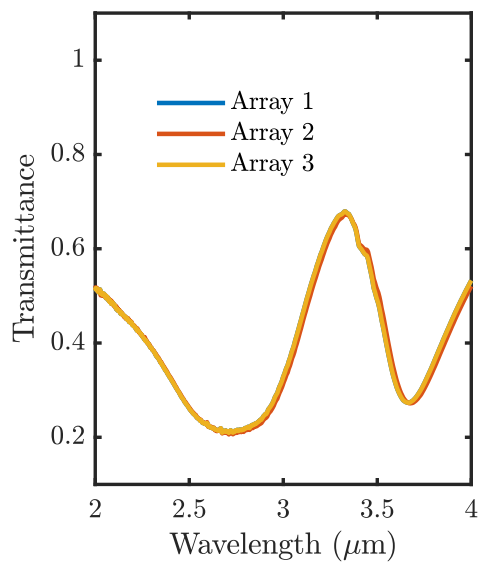
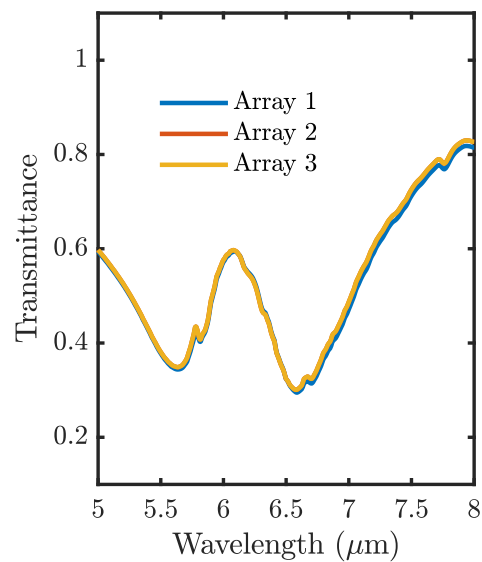
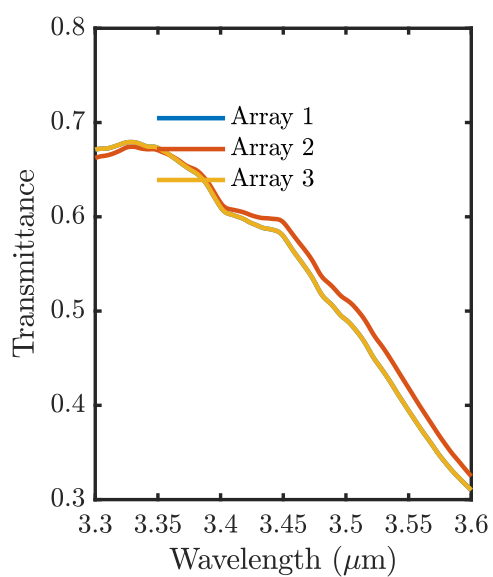
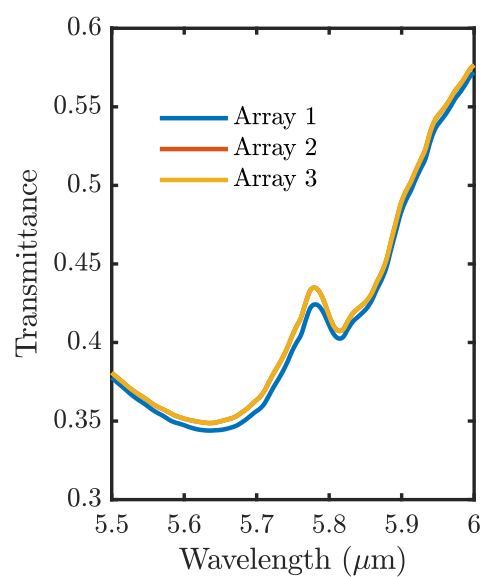
(a) ASH₁(b) ASH₂(c) ASH₁(d) ASH₂

Figure A.6: FTIR transmittance spectra of three arrays in a different area from samples mixtures of E2: E1 (4:4)